Nonlinear dissipative dynamics of optomechanical and laser arrays

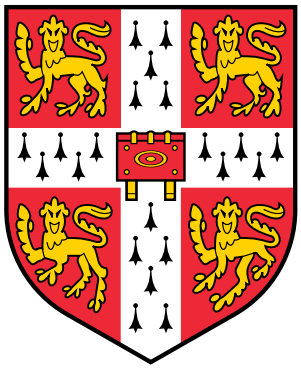

Petr Zapletal

Fitzwilliam College
University of Cambridge

Supervisor: Dr Andreas Nunnenkamp

July 2020

This dissertation is submitted for the degree of Doctor of Philosophy

To my father.

Declaration

I hereby declare that except where specific reference is made to the work of others, the contents of this dissertation are original and have not been submitted in whole or in part for consideration for any other degree or qualification in this or any other institution. This dissertation is my own work and includes nothing which is the outcome of work done in collaboration with others, except as detailed in the text and specified below. This dissertation contains fewer than 60,000 words including appendices, bibliography, footnotes, tables, and equations, and has fewer than 150 figures.

Chapters 2 and 3 contain work published in

- Ref. [1]: P. Zapletal, S. Walter, and F. Marquardt, *Dynamically Generated Synthetic Electric Fields for Photons*, Phys. Rev. A **100**, 023804 (2019).
- Ref. [2]: P. Zapletal and A. Nunnenkamp, *Dynamical generation of synthetic electric fields for photons in the quantum regime*, Quantum Sci. Technol. **4**, 044001 (2019).
- Ref. [3]: P. Zapletal, B. Galilo, and A. Nunnenkamp, *Long-lived elementary excitations and light coherence in topological lasers*, arXiv:2002.12337 (2020) – accepted for publication in *Optica*.

Petr Zapletal
July 2020

Acknowledgments

First and foremost, I would thank Andreas for being my supervisor and mentor during the past three years. I very much appreciate the stimulating questions that you asked and your patience while I was trying to answer them. I was able to understand what it means to be an independent researcher in theoretical physics thanks to not only your support and guidance but also the freedom in making my own choices that you left me. I admire your unique style of doing theoretical research. It was a pleasure working with you and learning from you.

Special thanks go to Stefan Walter, Bogdan Galilo and Florian Marquardt for fruitful collaboration on research projects, which I enjoyed very much. I greatly appreciate that Florian provided me with a lot of guidance and support, through which I managed to learn so much about theoretical research and how to present it in a simple yet very accurate manner. Working with you was an enjoyable experience that is invaluable for my future career.

I feel very lucky to share the time of my PhD studies with Andreas' team. Andrea, Bogdan, Clara, Daniel, Eze, Matteo, Simon thank you very much for countless inspiring discussions during coffee and lunch breaks as well as for being such wonderful friends. I am very grateful to my colleagues and friends Adam, Alex, Angela, Beñat, Elis, Iria, Ivona, James, Jan, Max, Nick, Philippe, and Tycho as well as the senior group members Austen, Claudio, Johannes, Nigel for creating an inspiring and welcoming environment in the Theory of Condensed Matter group at the Cavendish Laboratory. Thank you for many insightful discussions, which broadened my horizons both scientifically and personally. I very much enjoyed the time with you including Friday drinks, pub nights and unforgettable Christmas parties. I am very happy that I shared our office with Attila and Ollie. Thank you for making a stimulating and friendly atmosphere as well as for endless conversations about vague ideas and tedious technical problems. I am very grateful to Eze, Matteo, Max, and Ollie for proofreading of this thesis.

I cannot express enough how thankful I am to all my teachers and supervisors for teaching me the basics of physics and sharing their excitement for the subject. Special mention goes to Radim Filip, who first introduced me to theoretical research and who has been my mentor throughout my entire University education. Your continuous

support has been inspiring and ensuring. Your advice and guidance helped me to make the right decisions throughout my studies, which unfolded in a way that I could never have envisioned 10 years ago when I first met you.

Going through my PhD would not be possible without loved ones outside the department. First, I would like to thank Friederike for her support in times when I really needed it, a very enjoyable companionship and a lot of love. I am very grateful to the Fitz family for creating home for me in Cambridge. I especially thank Lorenzo for endless discussions about physics, politics and life in general, Costanza for being wonderful and understanding flatmate and for passionate exchanges of opinions, Carlos and Oliver for always being ready to hang out and talk about silly stuff and for their companionship during the lockdown, as well as Pavao for being an excellent opponent during squash games and a good friend otherwise. I would like to also thank Maria-Christina for being an amazing friend and a splendid dancing partner. We pulled off some *great* dancing.

Last but not least, big thanks go to my family for their amazing support and endless love. I am very thankful to Helča for her siblings rivalry and love. I cannot thank my parents enough for their love and for always believing in me in any situation. I am very grateful to my mum for continuously advising me and supporting me in my life.

Abstract

In this thesis, we study nonlinear dissipative dynamics of two different systems: (i) synthetic dynamical gauge fields for photons in optomechanical arrays and (ii) laser arrays with a topologically nontrivial structure. The chosen models are relevant to state-of-the-art optomechanical experiments as well as to recent implementations of topological lasers based on semiconductor ring-resonator arrays. We present our results with a focus on applications.

First, we investigate nonlinear dynamics of synthetic gauge fields in optomechanical arrays in the classical regime. We demonstrate that synthetic electric fields for photons are generated in open one-dimensional arrays, leading to the suppression of light transport. Importantly, the generation of synthetic electric fields depends on the direction of light propagation, giving rise to unidirectional light transport. In a second step, we investigate the quantum dynamics of synthetic gauge fields in the minimal setup composed of two optical modes with photon tunneling assisted by a mechanical self-oscillator. Employing the quantum van-der-Pol oscillator as the simplest dynamical model for a mechanical self-oscillator enables us to take quantum fluctuations into account using the quantum master equation formalism. We show that the generation of synthetic electric fields is robust against fluctuations and unidirectional light transport can be achieved also in the quantum regime.

In the second part of the thesis, we study topological lasing, which arises from the combination of topologically-protected chiral light transport and laser amplification, leading to laser operation that is robust against local disorder in system parameters and defects. We study a topological laser arrays based on the photonic Haldane model with selective pumping of chiral edge modes described by saturable gain. We investigate elementary excitations around the mean-field steady state and their consequences for the coherence properties. In particular, we show that the hybridization of chiral edge modes gives rise to long-lived elementary excitations, leading to large phase fluctuations in the emitted light field and a decrease of light coherence. In contrast to topologically trivial lasers, the lifetime of elementary excitations is robust against disorder in topological lasers. The lifetime depends strongly on the edge-mode dispersion around the lasing

frequency. As a result, the lifetime can be reduced by orders of magnitude for lasing of different edge modes, leading to a suppression of phase fluctuations and, consequently, larger coherence of the emitted light. On the other hand, amplitude fluctuations and the second-order autocorrelation function are moderately increased at the same time.

Contents

1 Introduction

All physical systems must be regarded as open systems since they can never be perfectly isolated from their environment. The interaction of a system with its environment leads to the irreversible process of *dissipation*, during which the system exchanges energy with its environment. This thesis is concerned with the interplay between coherent dynamics described by a Hamiltonian and dissipation in systems coupled to their environment.

We are interested in *nonlinear dissipative systems* whose dynamical behavior can be very rich. A key role in the theoretical work presented in this thesis is played by *limit-cycle oscillations*, which are a prominent nonlinear effect [4] . Limit-cycle oscillations generically arise from the competition of nonlinear damping and pumping. An isolated limit-cycle oscillator maintains oscillations at its intrinsic frequency and its phase is determined by initial conditions. The dynamics of limit cycle oscillators coupled in an array is very naturally tied together with the physics of *synchronization*, which is a ubiquitous phenomenon appearing in a wide range of nonlinear dissipative systems [5].

We focus on *cavity optomechanics*, which deals with the interaction of light and mechanical oscillators [6]. Recent developments have led to quantum control of mechanical oscillators [7, 8, 9] and the engineering of their dissipative environment [10, 11, 12, 13]. This enables testing fundamental laws of quantum physics in novel regimes involving massive objects in controlled environments. Cavity optomechanics offers the possibility of implementing new devices with usuful applications for *quantum technology* [14], which harnesses quantum mechanical effects for technological advances. In the first project presented in this thesis, we study an optomechanical array with photon tunneling assisted by a coherent emission/absorption of a phonon from mechanical oscillators. We assume that the mechanical oscillators perform limit-cycle oscillations giving rise to a nonlinear dynamics, which we connect to the mathematical formalism of *dynamical gauge fields*. *Static* synthetic gauge fields have been first envisaged and implemented

for cold atoms [15, 16] and then for photons [17, 18, 19, 20, 21, 22, 23, 24, 25], phonons [26, 27, 28, 29], and other platforms [30, 31]. While in these systems, synthetic gauge fields are fixed to external parameters, we explore their natural extension allowing for the dynamics of synthetic gauge fields. In particular, we investigate how the rich dynamics of gauge fields is affected by quantum noise [32]. We uncover a novel mechanism of unidirectional light transport via synthetic dynamical gauge fields, which can lead to new nonlinear photonic devices.

Other interesting avenues in exploring dissipative dynamics are offered by *topological photonics* [33]. This field extends the concept of energy-band topology, originally used to understand the physics of topological insulators [34, 35], to photonic structures such as photonic crystals [36], arrays of semiconductor ring resonators [23] and optical waveguides [37]. As gain and loss are inherently present in photonic structures, it is necessary to develop a theoretical framework for topology in non-Hermitian regimes involving dissipative dynamics to uncover whether topological photonic structures can be employed for the implementation of new devices such as delay lines immune to backscattering [19] and optical isolators [38]. The interplay between dissipation and topology plays a crucial role also in other systems including exciton polaritons [39], cold atoms [40], mechanical metamaterials [41] and electrical circuits [42]. In the second project presented in this thesis, we study lasers – an archetypical example of limit-cycle oscillators – arranged in an array with an underlying topologically-nontrivial structure. The combination of topologically-protected chiral light transport and laser amplification offers a novel design of laser devices. In particular, single-mode lasing, leading to a large-intensity monochromatic light emission, is robust against fabrication imperfections and defects in topological lasers in contrast to their trivial counterparts [43, 44]. We investigate elementary excitations around the mean-field steady state and their consequences for coherence properties of topological lasers, which are essential characteristics of laser devices important for practical applications [45].

Our work opens interesting avenues for studying the classical and quantum dynamics of synthetic gauge fields based on optomechanical arrays as well as for uncovering the role of topology in a novel nonlinear non-Hermitian regime employing topological light emitters. Future directions include strong nonlinearities leading to genuine quantum features of dynamical gauge fields in optomechanical arrays and to topologically protected generation of nonclassical light in topological photonic arrays.

1.1 Thesis outline

In this thesis, we investigate the nonlinear dissipative dynamics of synthetic gauge fields for photons in optomechanical arrays and of laser arrays with a topologically nontrivial structure. In this chapter, we introduce theoretical methods and basic physical concepts important for the original work presented in chapters 2 and 3.

We start with a brief description of nonlinear dissipative systems. The dynamics of expectation values for system variables is discussed in sections 1.2 and 1.3. It is followed by the description of quantum fluctuations in section 1.4 employing Langevin equations of motion and Lindblad master equations. We pay special attention to *limit-cycle oscillations*, which play an important role in the research presented in this thesis. We then discuss in section 1.5 the basic concepts of lasers, which are a prominent example of a nonlinear dissipative system driven far from equilibrium. We focus on the dynamics of the light field in a laser employing a Langevin equation of motion taking fluctuations into account. We discuss the properties of fluctuations in a laser driven above threshold performing limit-cycle oscillations and the coherence properties of the light field. In the intermezzo 1.6, we introduce the quantum van-der-Pol oscillator to investigate the effects of quantum fluctuations on limit-cycle oscillations using a Lindblad master equation. Section 1.7 is concerned with the interaction between light and mechanical oscillators. We particularly focus on the situation in which an effective optomechanical damping is negative, giving rise to self-sustained mechanical oscillations, which are an example of a limit-cycle.

In chapter 2, we present original research published in Refs. [1, 2], which is concerned with the dynamics of synthetic gauge fields for photons in optomechanical arrays with phonon-assisted photon tunneling. Importantly, we consider that mechanical modes in the optomechanical arrays perform self-sustained oscillations. As a result, mechanical phases can represent *synthetic dynamical gauge fields* for photons as they are not fixed to any external parameter and they can evolve according to their own dynamics. First, we investigate the dynamics of synthetic gauge fields in the classical regime, where quantum fluctuations around large optical and mechanical amplitudes can be neglected. Our results, published in Ref. [1], show that synthetic electric fields for photons can be dynamically generated in open one-dimensional arrays leading to unidirectional light transport. Second, we employ the quantum van-der-Pol oscillator as

a simple model of a mechanical self-oscillator allowing us to investigate the effects of quantum fluctuations on the dynamics of synthetic gauge fields using master-equation simulations. We demonstrate that the dynamical generation of synthetic electric fields is robust against fluctuations and that unidirectional light transport can be achieved also in the quantum regime. This is published in Ref. [2].

In chapter 3, we start by providing an overview of the theory for the topology of energy bands which has recently been extended for a wide range of systems including photonic arrays. We then present an original work, published in Ref. [3], investigating the interplay of a topologically-protected unidirectional light transport and laser amplification in photonic arrays, leading to so-called *topological lasing*. In particular, we study elementary excitations around the mean-field steady state and their consequences for the coherence properties of the light field emitted by a topological laser.

In this thesis, we assume that $\hbar = 1$.

1.2 Equations of motion

In many situations, dissipative systems can be well characterized by mean values of certain variables. The dynamical behavior of nonlinear dissipative systems can be accurately described by the equations of motion for these mean values if fluctuations are negligibly small compared to the mean values. We can study the time evolution of these mean values using the theory of dynamical systems [4]. In this section, we discuss general properties of equations of motion and their stationary solutions.

We assume that the time-evolution of mean values for certain variables can be described by equations of motion

$$\dot{\mathbf{x}} = v(\mathbf{x}, t), \tag{1.2.1}$$

where the vector $\mathbf{x}$ contains the mean values and v is an arbitrary function. If the function v has a special form $v(\mathbf{x}, t) = \mathbf{A}(t)\,\mathbf{x} + \mathbf{b}(t)$, the equations of motion describe a linear system, where $\mathbf{A}(t)$ is a matrix and $\mathbf{b}(t)$ is a vector of constants. Linear equations of motion have a general solution

$$\mathbf{x}(t) = e^{\int_0^t \mathrm{d}\tau\, \mathbf{A}(\tau)} \left[\mathbf{x}(0) + \int_0^t \mathrm{d}\tau e^{-\int_0^\tau \mathrm{d}s\, \mathbf{A}(s)} \mathbf{b}(\tau) \right], \tag{1.2.2}$$

where $\mathbf{x}(0)$ is a vector containing initial values.

In this thesis, we are interested in nonlinear systems, which cannot be described by equations of motion in the linear form $v(\mathbf{x}, t) = \mathbf{A}(t)\,\mathbf{x} + \mathbf{b}(t)$. In particular, we are interested in *autonomous* systems, whose equations of motion are not explicitly dependent on time, i.e. $v(\mathbf{x}, t) = v(\mathbf{x})$ [4].

Stationary solutions of equation (1.2.1) are important for the description of dynamical systems. A stationary solution $\mathbf{x}^*$ satisfies $v(\mathbf{x}^*) = 0$. Stationary solutions represent *steady states* of a dynamical system. If the system reaches a steady state, it remains in the steady state indefinitely. The dynamics of the system in the vicinity of a stationary solution can be described by linear equations of motion

$$\dot{\mathbf{x}} = \mathbf{J}\,\mathbf{x}, \tag{1.2.3}$$

where $\mathbf{J}$ is the Jacobian matrix and $J_{jk} = \left.\frac{\partial v_j}{\partial x_k}\right|_{\mathbf{x}=\mathbf{x}^*}$ [4].

Equation (1.2.3) has a general solution $\mathbf{x}(t) = e^{\mathbf{J}t}\,\mathbf{x}(0)$ for $\mathbf{x}(0)$ lying in the vicinity of $\mathbf{x}^*$. If all eigenvalues of the Jacobian matrix $\mathbf{J}$ have negative real parts, the stationary solution $\mathbf{x}^*$ represents a *stable* steady state. The system is attracted to the stable steady state if it is initially in the vicinity of the steady state. All initial conditions $\mathbf{x}(0)$, for which the system asymptotically approaches the stable steady state, form the basin of attraction of the steady state. The largest (smallest in magnitude) real part of Jacobian-matrix eigenvalues determines the rate with which the system asymptotically approaches the steady state. If any eigenvalue of the Jacobian matrix has a positive real part, the system diverges from the steady state and the steady state is *unstable*.

1.3 Limit cycle

In the previous section, we discussed steady states of equations of motion. If a system reaches a steady state it remains in the steady state indefinitely. This represents one kind of the asymptotic solution for the equations of motion at long times. In this section, we will focus on a different kind of asymptotic solution for equations of motion, namely limit cycles.

A limit cycle is a closed *isolated* trajectory [4]. A closed trajectory is a solution $\mathbf{x}(t)$ of equations of motion, which is periodic in time, i.e. $\mathbf{x}(t) = \mathbf{x}(t + T)$, where T is the

period. A closed trajectory is isolated if all trajectories in its vicinity are not closed, i.e. they either converge to or diverge from the closed trajectory. A limit cycle is *stable* if all trajectories in its vicinity converge to it. A limit cycle is *unstable* if any trajectory in its vicinity diverges from it.

Limit cycles are intrinsically nonlinear phenomena, which do not occur in linear systems [4]. Linear systems $\dot{\mathbf{x}} = \mathbf{A}\,\mathbf{x}$ can have closed trajectories but they cannot be isolated. If $\mathbf{x}(t) = \mathbf{x}(t+T)$ is a closed trajectory then also $c\,\mathbf{x}(t)$ is a closed trajectory for any constant $c \neq 0$.

To illustrate generic features, we now consider a so-called van-der-Pol oscillator, which is an archetypical example of a nonlinear system featuring a limit cycle [5]. The complex amplitude b of the van-der-Pol oscillator is described by the equation of motion

$$\dot{b} = -i\Omega\, b + \frac{\gamma_1}{2}\, b - \gamma_2\, |b|^2 b, \tag{1.3.1}$$

where Ω is the oscillation frequency, γ_1 is the rate of linear damping (or linear gain for $\gamma_1 > 0$) and γ_2 is the rate of nonlinear damping. To avoid unphysical solutions with an indefinitely growing amplitude $|b|$, we assume $\gamma_2 > 0$.

We can write the equations of motion for the amplitude B and the phase ϕ of the van-der-Pol oscillator

$$\dot{B} = \left(\frac{\gamma_1}{2} - \gamma_2\, B^2\right) B, \tag{1.3.2}$$

$$\dot{\phi} = -\Omega, \tag{1.3.3}$$

where $b = Be^{i\phi}$. We can see that the equations of motion for the amplitude and the phase are decoupled and we can study them separately. The phase of the van-der-Pol oscillator evolves with a constant angular velocity Ω. Inspecting equation (1.3.2), we can see that the van-der-Pol oscillator has two stationary amplitudes $B = 0$ and $B = \sqrt{\frac{\gamma_1}{2\gamma_2}}$, for which the amplitude remains constant indefinitely. The stationary solution $B = \sqrt{\frac{\gamma_1}{2\gamma_2}}$ exists for $\gamma_1 > 0$ and the stationary solution $B = 0$ exists for any value of γ_1.

For $\gamma_1 < 0$, $\dot{B} < 0$ for any $B > 0$, which means that B always decays to zero. Coming back to the complex amplitude b, we conclude that all trajectories $b(t)$ spiral towards $b = 0$, making it a stable steady state.

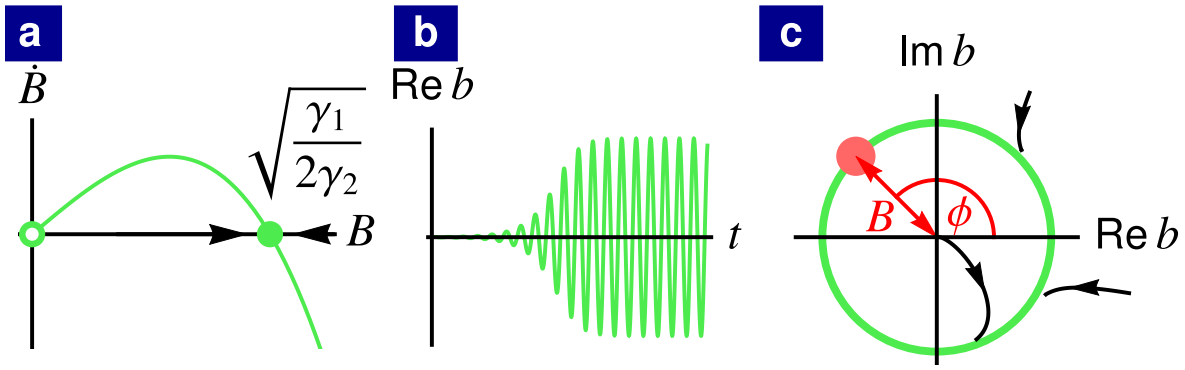

Figure 1.3.1: Emergence of limit-cycle oscillations in the van-der-Pol oscillator for $\gamma_1 > 0$. (a) Time derivative $\dot{B}$ of the amplitude as a function of the amplitude B with an unstable steady state for $B = 0$ and a stable steady state for $B = \sqrt{\frac{\gamma_1}{2\gamma_2}}$. (b) Build-up of limit-cycle oscillations for a small initial complex amplitude $|b| \ll \sqrt{\frac{\gamma_1}{2\gamma_2}}$. (c) Asymptotic solution $b = Be^{i\phi}$ in phase space (green line) with the amplitude B and the phase $\phi = -\Omega t + \phi_0$. Black arrows show trajectories approaching the limit cycle.

For $\gamma_1 > 0$, we plot the time derivative $\dot{B}$ of the amplitude as a function of the amplitude B in Fig. 1.3.1a. $\dot{B} > 0$ for $0 < B < \sqrt{\frac{\gamma_1}{2\gamma_2}}$ and $\dot{B} < 0$ for $\sqrt{\frac{\gamma_1}{2\gamma_2}} < B$, which means that B converges to the stationary value $\sqrt{\frac{\gamma_1}{2\gamma_2}}$ for any $B(0) > 0$. Coming back to the complex amplitude b, we conclude that all trajectories $b(t)$ with $b(0) \neq 0$ approach the asymptotic solution $b(t) = \sqrt{\frac{\gamma_1}{2\gamma_2}} e^{-i(\Omega t - \phi_0)}$ depicted in Fig. 1.3.1c. This asymptotic solution represents a stable limit cycle, since it is periodic (with period $2\pi/\Omega$) and all trajectories in its vicinity converge to it (black arrows in Fig. 1.3.1c). The phase ϕ_0 of the asymptotic oscillations is determined by initial conditions $b(0)$ but the amplitude $\sqrt{\frac{\gamma_1}{2\gamma_2}}$ of the asymptotic oscillations is independent of the initial conditions. The steady state $b = 0$ is unstable as all trajectories $b(t)$ with $b(0) \neq 0$ diverge from this steady state.

To shed more light on the dynamics in the vicinity of the limit cycle, we linearize the equations of motion (1.3.2) and (1.3.3) around a given point on the limit cycle $b = \sqrt{\frac{\gamma_1}{2\gamma_2}} e^{i\phi}$. The linearized equations of motion are

$$\begin{pmatrix} \dot{B} \\ \dot{\phi} \end{pmatrix} = \mathbf{J} \begin{pmatrix} B \\ \phi \end{pmatrix}, \tag{1.3.4}$$

where

$$\mathbf{J} = \begin{pmatrix} \frac{\partial \dot{B}}{\partial B} & \frac{\partial \dot{B}}{\partial \phi} \\ \frac{\partial \dot{\phi}}{\partial B} & \frac{\partial \dot{\phi}}{\partial \phi} \end{pmatrix}\Bigg|_{B=\sqrt{\frac{\gamma_1}{2\gamma_2}}} = \begin{pmatrix} -\gamma_1 & 0 \\ 0 & 0 \end{pmatrix} \tag{1.3.5}$$

is the Jacobian matrix. We directly see that the eigenvalues of the Jacobian matrix are $\lambda_1 = -\gamma_1$ and $\lambda_2 = 0$. The eigenvalue $\lambda_1 = -\gamma_1$ determines the rate at which the amplitude B relaxes towards the stationary value $\sqrt{\frac{\gamma_1}{2\gamma_2}}$. The eigenvalue $\lambda_2 = 0$ corresponds to an undamped degree of freedom in a form of the phase ϕ. The presence of a zero-valued eigenvalue and a corresponding undamped degree of freedom are generic features of limit cycles.

In this section, we introduced limit cycles, which are inherently nonlinear phenomena. Limit cycles play a key role in the research presented in this thesis. In Chapter. 2, we will consider an optomechanical system performing self-sustained oscillations, which correspond to a stable limit cycle. Chapter. 3 is concerned with lasers, which are another example of systems performing limit-cycle oscillations.

1.4 Quantum fluctuations

In the previous sections, we discussed the time evolution of mean values for certain variables describing a dissipative system. In this section, we will focus on fluctuations of these variables and their time evolution. In dissipative quantum systems, fluctuations can have two different origins [32]. First, the intrinsic uncertainty in a quantum system leads to vacuum fluctuations, which are present even if the system has a vanishing energy on average. Quantum vacuum fluctuations are always present in the system even if the system is perfectly isolated from its environment. Second, the coupling of the system to its environment leads to stochastic forces due to quantum and thermal fluctuations in the environment. These stochastic forces give rise to additional fluctuations in the system. In this section, we focus on the description of fluctuations in dissipative quantum systems. We describe their environment as a bath. We consider a quantum system weakly coupled to a Markovian bath, which is memoryless.

1.4.1 Quantum Langevin equations

Quantum Langevin equations describe the time evolution of operators for a dissipative system, taking into account quantum fluctuations and stochastic forces due to the coupling of the system to the bath [32]. In this section, we introduce the concept of quantum Langevin equations and the assumptions for the bath and the system-bath coupling, for which quantum Langevin equations are valid.

We consider that the unitary evolution of a system is described by the Hamiltonian $\hat{H}_{\text{sys}}$. First, we assume that a bath consists of an infinite number of harmonic oscillators, whose frequency spectrum is smooth and dense. Second, we assume that the system-bath coupling has a linear form $\hat{H}_{\text{int}} = \sum_n k_n \hat{q}_n \hat{X}$, where $\hat{X}$ is some system operator, $\hat{q}_n$ is the position operator of a harmonic oscillator in the bath, and the system-bath coupling constants k_n are a smooth function of the frequency of the harmonic oscillators. These assumptions are properties of a quantum field [32]. This makes them very practical, since we usually consider the bath to be a quantum field, for example an electromagnetic field. Next, we also consider the *Markov approximation*, which assumes that (i) the system-bath coupling constants k_n are frequency independent and (ii) the frequency spectrum of the bath has a linear dispersion. Due to the assumptions of the Markov approximation, the memory time of the bath is zero.

We now consider a particular example of an optical mode coupled to a semi-infinite waveguide, which can be used as a model for many systems considered in this thesis. We discuss quantum Langevin equations for operators of the optical mode treating the semi-infinite waveguide as a bath. The free evolution of this particular bath is described by the Hamiltonian

$$\hat{H}_B = \int \frac{\mathrm{d}k}{2\pi}\, \omega_k\, \hat{b}_k^\dagger \hat{b}_k, \tag{1.4.1}$$

where $\hat{b}_k$ is an annihilation operator of a plane-wave mode with wave vector k. The system-bath coupling has the following form

$$\hat{H}_{\text{int}} = -\alpha \int \frac{\mathrm{d}k}{2\pi} \left(\hat{b}_k^\dagger + \hat{b}_k\right)\left(\hat{a}^\dagger + \hat{a}\right), \tag{1.4.2}$$

where $\hat{a}$ is the annihilation operator of the optical mode. The coupling constant α is frequency independent, which is the first assumption of the Markov approximation. Writing explicitly the time-dependence of the bath operators $\hat{b}(t) = e^{-i\omega_k t}\hat{b}(0)$ and ex-

pressing the operators of the optical mode in a rotating frame with its natural frequency ω_c, we can rewrite the interaction Hamiltonian as

$$\hat{H}_{\text{int}} = -\alpha \int \frac{\mathrm{d}k}{2\pi} \left[e^{i\omega_k t} \hat{b}_k^\dagger(0) + e^{-i\omega_k t} \hat{b}_k(0) \right] \left(e^{i\omega_c t} \hat{a}^\dagger + e^{-i\omega_c t} \hat{a} \right). \tag{1.4.3}$$

For a weak coupling $\alpha \ll \omega_c, \omega_k$, terms $\hat{b}_k^\dagger \hat{a}^\dagger$ and $\hat{b}_k \hat{a}$ oscillate with a large frequency $\omega_c + \omega_k$. Due to their rapid oscillations, these terms average to zero and they can be neglected within the *rotating-wave approximation*. Switching also bath operators into a frame rotating with the frequency ω_c, we obtain

$$\hat{H}_B = \int \frac{\mathrm{d}k}{2\pi} \, \bar{\omega}_k \, \hat{b}_k^\dagger \hat{b}_k, \tag{1.4.4}$$

$$\hat{H}_{\text{int}} = -\alpha \int \frac{\mathrm{d}k}{2\pi} \left(\hat{b}_k^\dagger \hat{a} + \hat{b}_k \hat{a}^\dagger \right), \tag{1.4.5}$$

where $\bar{\omega}_k = \omega_k - \omega_c$. We can now write the Heisenberg equation of motion for the bath operators

$$\dot{\hat{b}}_k = -i\bar{\omega}_k \hat{b}_k + i\alpha \hat{a}, \tag{1.4.6}$$

which has the solution

$$\hat{b}_k(t) = e^{-i\bar{\omega}_k t} \hat{b}_k(0) + i\alpha \int_0^t \mathrm{d}\tau \, e^{-i\bar{\omega}_k (t-\tau)} \hat{a}(\tau). \tag{1.4.7}$$

The Heisenberg equation of motion for the optical mode operator reads

$$\dot{\hat{a}} = i \left[\hat{H}_{\text{sys}}, \hat{a} \right] + i\alpha \int \frac{\mathrm{d}k}{2\pi} \, \hat{b}_k(t) \tag{1.4.8}$$

$$= i \left[\hat{H}_{\text{sys}}, \hat{a} \right] + i\alpha \int \frac{\mathrm{d}k}{2\pi} e^{-i\bar{\omega}_k t} \hat{b}_k(0) - \alpha^2 \int \frac{\mathrm{d}k}{2\pi} \int_0^t \mathrm{d}\tau \, e^{-i\bar{\omega}_k (t-\tau)} \hat{a}(\tau), \tag{1.4.9}$$

where $\left[\hat{A}, \hat{B} \right] = \hat{A}\hat{B} - \hat{B}\hat{A}$ is a commutator. The term $i \int \frac{\mathrm{d}k}{2\pi} e^{-i\bar{\omega}_k t} \hat{b}_k(0) \equiv \sqrt{v} \hat{a}_{\text{in}}(t)$ involves bath operators at time zero. It describes the input signal coming from the bath to the optical mode at time t. We now consider that the frequency spectrum of the bath has a linear dispersion $\bar{\omega} = vk + \text{const}$, which is the second assumption of the

Markov approximation. We can then evaluate the term

$$-\alpha^2 \int \frac{\mathrm{d}k}{2\pi} \int_0^t \mathrm{d}\tau\, e^{-i\bar{\omega}_k(t-\tau)}\hat{a}(\tau) = -\alpha^2 \int_0^t \mathrm{d}\tau \int \frac{\mathrm{d}k}{2\pi}\, e^{-ivk(t-\tau)}\hat{a}(\tau) \tag{1.4.10}$$

$$= -v\alpha^2 \int_0^t \mathrm{d}\tau\, \delta(t-\tau)\hat{a}(\tau) \tag{1.4.11}$$

$$= -\frac{\kappa}{2}\hat{a}(t), \tag{1.4.12}$$

where $\kappa = v\alpha^2$, and $\delta(t)$ is the Dirac delta function. Coming back to the Heisenberg equation of motion for the optical mode, we can write

$$\dot{\hat{a}} = i\left[\hat{H}_{\mathrm{sys}}, \hat{a}\right] - \frac{\kappa}{2}\hat{a} + \sqrt{\kappa}\hat{a}_{\mathrm{in}}. \tag{1.4.13}$$

The second term on the right-hand side provides decay of the optical mode. The third term on the right-hand side describes the input signal coming to the optical mode from the bath. It can be interpreted as a stochastic force driving the optical mode. Depending on a particular initial state of the bath, this stochastic force can provide both thermal and quantum fluctuations. For a thermal occupation of the bath with the mean photon number n_{th}, the input signal has correlations

$$\langle \hat{a}_{\mathrm{in}}(t)\hat{a}^\dagger_{\mathrm{in}}(t')\rangle = (n_{\mathrm{th}}+1)\delta(t-t'), \tag{1.4.14}$$

$$\langle \hat{a}^\dagger_{\mathrm{in}}(t)\hat{a}_{\mathrm{in}}(t')\rangle = n_{\mathrm{th}}\delta(t-t'), \tag{1.4.15}$$

$$\langle \hat{a}_{\mathrm{in}}(t)\rangle = 0. \tag{1.4.16}$$

Even for a vanishing mean photon number n_{th}, the driving force does not completely vanish, but instead $\langle \hat{a}_{\mathrm{in}}(t)\hat{a}^\dagger_{\mathrm{in}}(t')\rangle = 1$ due to vacuum fluctuations.

Quantum Langevin equations have the same form as classical Langevin equations for brownian motion. However, quantum Langevin equations describe the time-evolution of operators, which, in principle, do not have to commute, in contrast to commuting variables in classical Langevin equations. In some situations, we can derive equivalent classical Langevin equations, which correctly reproduce expectation values of operators described by quantum Langevin equations.

Returning to the equations of motion (1.4.6) for bath operators, we can also describe the signal traveling in the semi-infinite waveguide from the optical mode to infinity. To

this end, we set the origin of time at a large time T yielding the solution

$$\hat{b}_k(t) = e^{-i\bar{\omega}_k(t-T)}\hat{b}_k(T) + i\alpha \int_t^T \mathrm{d}\tau\, e^{-i\bar{\omega}_k(t-\tau)}\hat{a}(\tau). \tag{1.4.17}$$

Repeating the same steps as above, we derive the Langevin equation

$$\dot{\hat{a}} = i\left[\hat{H}_{\mathrm{sys}}, \hat{a}\right] + \frac{\kappa}{2}\hat{a} + \sqrt{\kappa}\hat{a}_{\mathrm{out}}, \tag{1.4.18}$$

where we introduced the output field $\sqrt{v}\hat{a}_{\mathrm{out}}(t) \equiv \int \frac{\mathrm{d}k}{2\pi} e^{-i\bar{\omega}_k(t-T)}\hat{b}_k(T)$. Subtracting equation (1.4.13) from equation (1.4.18), we obtain the *input-output relation* [32]

$$\hat{a}_{\mathrm{out}}(t) = \hat{a}_{\mathrm{in}}(t) - \sqrt{\kappa}\hat{a}(t). \tag{1.4.19}$$

The outgoing signal consists of the input signal reflected from the end of the semi-infinite waveguide and the signal $\sqrt{\kappa}\hat{a}(t)$ leaking out of the optical mode.

In this section, we derived the quantum Langevin equation for an optical mode coupled to a semi-infinite waveguide and the input-output relation allowing us to study the signal leaking out of the optical mode into the waveguide. The particular form of the quantum Langevin equation and the input-output relation derived here describe a more general situation of an optical mode coupled to an electromagnetic field satisfying the assumptions of the Markov approximation. In general, an optical mode can be coupled to a non-Markovian bath, which has a finite memory time [46]. In such a situation, the description of the system-bath coupling is more complicated. However, in this thesis, we consider baths that are well described by the Markov approximation.

1.4.2 Lindblad master equation

A different approach to studying fluctuations in quantum dissipative systems employs Lindblad master equations [32]. In contrast to quantum Langevin equations, which describe the time evolution of system operators, Lindblad master equations describe the time evolution of quantum states which characterize the dissipative system. They can be derived by assuming a weak interaction of the system with a bath and employing the Markov approximation. Depending on a particular problem that we are trying to solve, Lindblad master equations or quantum Langevin equations can be more suitable

to describe fluctuations. For example, Lindblad master equations are very useful for finding a steady state of a dissipative system as we will discuss in this section.

Due to the interaction of the system with a bath, the system cannot always be described by a pure state $|\psi\rangle$. In general, the system can be characterized by a statistical mixture of states $|\psi_a\rangle$, where the system is in the state $|\psi_a\rangle$ with the probability P_a. The statistical mixture is described by the density matrix $\hat{\rho} = \sum_a P_a |\psi_a\rangle\langle\psi_a|$, where $|\psi_a\rangle\langle\psi_a|$ is the outer product [32]. The density matrix $\hat{\rho}$ evolves in time according to the Lindblad master equation

$$\dot{\hat{\rho}} = -i\left[\hat{H}_{\text{sys}}, \hat{\rho}\right] + \sum_{j=1}^{N} \kappa_j \mathcal{D}[\hat{F}_j]\hat{\rho}, \tag{1.4.20}$$

assuming that the dissipative system is weakly coupled to the bath and the bath satisfies the assumptions of the Markov approximation [32]. In the absence of dissipation, i.e. $\kappa_j = 0$ for all j, the system would undergo unitary dynamics governed by the Hamiltonian $\hat{H}_{\text{sys}}$. The coupling of the system to the bath is described by dissipators in Lindblad form

$$\mathcal{D}[\hat{F}_j]\hat{\rho} = \hat{F}_j^\dagger \hat{\rho} \hat{F}_j - \frac{1}{2}\left(\hat{F}_j^\dagger \hat{F}_j \hat{\rho} + \hat{\rho}\hat{F}_j^\dagger \hat{F}_j\right), \tag{1.4.21}$$

where the system operators $\hat{F}_j$ are linearly coupled to the bath. Constants κ_j are rates of dissipation for the particular dissipation channel described by the dissipator $\mathcal{D}[\hat{F}_j]$.

We can rewrite the master equation (1.4.20) in the following form

$$\dot{\hat{\rho}} = -i\hat{H}_{\text{eff}}\hat{\rho} + i\hat{\rho}\hat{H}_{\text{eff}}^\dagger + \sum_{j=1}^{N} \kappa_j \hat{F}_j^\dagger \hat{\rho} \hat{F}_j, \tag{1.4.22}$$

where $\hat{H}_{\text{eff}} = \hat{H}_{\text{sys}} - i\sum_{j=1}^{N} \kappa_j \hat{F}_j^\dagger \hat{F}_j$ is an effective non-Hermitian Hamiltonian. The effective non-Hermitian Hamiltonian has complex eigenvalues, whose imaginary parts describe rates of dissipation due to the coupling to the bath. The coupling to the bath leads also to quantum jumps, which are described by the last term on the right-hand side of equation (1.4.22). The nature of quantum jumps depends on particular jump operators $\hat{F}_j$. An example of a quantum jump is the emission of a photon to the bath or the absorption of a photon from the bath.

Lindblad master equations can be derived for a more general kind of baths than

quantum Langevin equations. In particular, for the derivation of quantum Langevin equations, we need to assume that the bath consists of harmonic oscillators. This assumption is not necessary for the derivation of the Lindblad master equation, provided that all jump operators $\hat{F}_j$ are eigenoperators of the Hamiltonian $\hat{H}_{\text{sys}}$, i.e. $\left[\hat{H}_{\text{sys}}, \hat{F}_j\right] = \omega_j \hat{F}_j$. This condition is quite general since any system operator can be decomposed into eigenoperators of the Hamiltonian $\hat{H}_{\text{sys}}$. To derive Lindblad master equations, we only need to assume that the bath is in a stationary state, it satisfies the assumptions of the Markov approximation and the system-bath coupling is weak [32].

Importantly, the Lindblad master equation (1.4.20) is linear in terms of the density matrix $\hat{\rho}$. As a result, it can be written in the following form

$$\dot{\hat{\rho}} = \mathcal{L}\hat{\rho}, \tag{1.4.23}$$

where $\mathcal{L}$ is a Lindbladian superoperator, which represents a linear completely positive trace-preserving map. This implies that the density matrix remains completely positive during the time evolution and its trace remains equal to unity. Even though, the Lindbladian can, in principle, explicitly depend on time, we will focus only on time-independent Lindbladians, which are relevant for the problems studied in this thesis. The master equation then has a general solution

$$\hat{\rho}(t) = e^{\mathcal{L}t}\hat{\rho}(0). \tag{1.4.24}$$

The density matrix $\hat{\rho}$ can be decomposed into right eigenoperators $\hat{\sigma}_i$ of the Lindbladian, which satisfy

$$\mathcal{L}\hat{\sigma}_i = \lambda_i \hat{\sigma}_i, \tag{1.4.25}$$

where λ_i are their respective eigenvalues. The eigenoperators $\hat{\sigma}_i$ evolve in time according to

$$\hat{\sigma}_i(t) = e^{\lambda_i t}\hat{\sigma}_i(0). \tag{1.4.26}$$

For a physical Lindbladian, $\operatorname{Re}\lambda_i \leq 0$ for all eigenvalues λ_i to avoid exponentially growing solutions of the master equation. Real parts of the eigenvalues λ_i determine rates of decay and the imaginary parts determine oscillation frequencies. Eigenvalues of the Lindbladian are either real-valued or they come in complex conjugate pairs. Eigenoperators $\hat{\sigma}_i$, in general, do not have to be density matrices, i.e. they do not have

to be completely positive and their trace does not have to be equal to unity.

The density matrix $\hat{\rho}(t)$ can be decomposed at any time t during the time evolution into eigenoperators $\hat{\sigma}_i$. The decomposition of the density matrix $\hat{\rho}$ in terms of eigenoperators $\hat{\sigma}_i$ is very useful if we are looking for a long-time solution $\lim_{t\to\infty}\hat{\rho}(t)$ of the master equation. All eigenoperators $\hat{\sigma}_i$ decay to zero except from eigenoperators with $\mathrm{Re}\,\lambda_i = 0$. As a result, we can only look for eigenoperators with $\mathrm{Re}\,\lambda_i = 0$ to find the long-time solution. Depending on a particular Lindbladian, a single eigenvalue $\lambda_0 = 0$ can have a vanishing real part with all other eigenvalues having negative real parts or a multiple eigenvalues have vanishing real parts. In the case of a single eigenvalue $\lambda_0 = 0$ with a vanishing real part, the Lindbladian has a unique steady state $\hat{\rho}_S \propto \hat{\sigma}_0$, towards which the system converges in the long-time limit for any initial state $\hat{\rho}(0)$. In the case of multiple eigenvalues λ_i with vanishing real parts, the Lindbladian has a decoherence-free subspace, i.e. a subspace of the Hilbert space which is not damped, and the steady state is not unique [47]. Some information from the initial state $\hat{\rho}(0)$ is preserved during the time evolution. In this case, the Lindbladian can also have purely imaginary eigenvalues corresponding to persistently oscillating coherences.

If the Lindbladian has a single eigenvalue $\lambda_0 = 0$ with a vanishing real part, the steady state of the master equation can be efficiently found. In particular, we can efficiently solve for the kernel of the Lindbladian on a computer if we express the Lindbladian in the form of a matrix. For a Hilbert space with the dimension N, the Lindbladian can be represented by an $N^2 \times N^2$ matrix. In the case of an infinitely-dimensional Hilbert space, the steady state is usually (at least approximately) confined in a finite-dimensional subspace of the Hilbert space and we can focus only on the finite-dimensional subspace. The main computational limitation of solving for the kernel of the Lindbladian is the rapidly increasing size of the Lindbladian ($N^2 \times N^2$ matrix) with the dimension N of the Hilbert space. As a result, solving for a steady state of a master equation on a computer is limited only to systems with a relatively low dimension of the Hilbert space.

In this section, we discussed Lindblad master equations, which can be employed to study dissipative systems taking fluctuations into account. In some situations, Lindblad master equations can be more suitable for the description of dissipative systems than quantum Langevin equations. For example, Lindblad master equations are well suited for finding a steady state, characterizing the dissipative system in the long-time limit.

Together with the equations of motion for mean values of system variables, which were discussed in previous sections, we have now covered the essential methods employed in this thesis. In the remaining sections of this chapter, we will introduce the particular dissipative systems which are investigated in the following chapters.

1.5 Laser

In this section, we discuss lasers, which are a prominent example of a nonlinear dissipative system. In a laser, incoherently pumped two-level atoms are used to amplify a light field via the process of stimulated emission, leading to a large coherent population of a single mode of the light field. Here, we will focus on the dynamics of the light field in lasers and the nature of light emitted by lasers.

Laser is an acronym for *Light Amplification by Stimulated Emission of Radiation*. The concept of laser is based on the interaction of a light field with a nonlinear optical medium. The nonlinear medium consists of two-level atoms and the transition between the two atomic levels is incoherently pumped. The light field in a laser is amplified by the stimulated emission of photons into a single mode of the light field, which is in resonance with the transition between the atomic levels. The amplification of the light field leads to a large coherent population of the single mode. There is a large variety of optical media which can be used for laser amplification. This includes atoms doped in a solid state material as well as atomic gasses. However, laser amplification can be achieved employing also two-level transitions that are not direct atomic transitions. For example, an electronic transition in semi-conductors can be used as well. In this case, electronic levels of the whole crystalline structure are involved instead of energy levels of individual atoms. A review of possible optical media can be found in Ref. [45].

1.5.1 Effective dynamics of a light field

A detailed description of the interaction between a light field and atoms in a laser can be found in Refs. [32, 48]. In this section, we will focus only on the effective dynamics of the light field and its generic properties independent of the particular choice of an optical medium. The optical medium is placed in an optical cavity. Photons emitted into a mode of the cavity circulate many times inside before they leak out of the cavity.

This enhances the process of stimulated emission since each photon interacts many times with the optical medium. If the relaxation time of atoms in the optical medium is much shorter than the ringdown time of photons in the cavity, the atoms can be adiabatically eliminated leaving us with an effective description for the dynamics of the light field [32, 48].

The light field can be described by the classical Langevin equation

$$\dot{\alpha} = \left(-i\omega - \gamma + \frac{g}{1 + |\alpha|^2/I_{\text{sat}}}\right)\alpha + \sqrt{q}\alpha_{\text{in}}, \tag{1.5.1}$$

for the complex amplitude α, where ω is the resonant frequency, γ are optical losses, g is the optical gain, I_{sat} is the saturation intensity, q is the strength of fluctuations and α_{in} describes Gaussian white noise $\langle \alpha_{in}(t)\alpha^*_{in}(t')\rangle = \delta(t-t')$ [48]. This Langevin equation correctly reproduces first- and second-order normally-order correlations of the light field $\hat{a}$. The intensity $I = \langle |\alpha|^2 \rangle$ corresponds to the mean photon number $\langle \hat{a}^\dagger \hat{a} \rangle$. For large intensities, the factorization of higher statistical moments $\langle \hat{a}^{\dagger r} \hat{a}^r \rangle \approx I^r$ is a good approximation, which allows us to efficiently compute higher-order photon-number correlations [48].

The effective description of a light field captures two fundamental effects due to the interaction of the light field with an optical medium. The first effect is stimulated emission into the optical mode $\hat{a}$, which leads to the optical gain g. The second effect is spontaneous emission into the optical mode $\hat{a}$, which leads to a stochastic force α_{in}, since photons emitted via the process of spontaneous emission have a random phase. Spontaneous emission is usually the dominant source of fluctuations in a laser even though other sources of noise can contribute to the total noise of strength q. Such additional sources of noise can be due to the coupling of the optical mode to its environment. The coupling to the environment leads also to optical losses γ. It is desirable that the optical mode $\hat{a}$ is dominantly coupled to a waveguide which is used to outcouple light from the laser. In this way, the leaking of light from the mode $\hat{a}$ into the waveguide dominates over intrinsic optical losses.

The effective description of a light field is very general. It does not assume any physical details of the optical medium except from the fact that the optical medium adiabatically follows the dynamics of the light field. Despite its simplicity, the effective description captures the effects of stimulated and spontaneous emissions, which are the

fundamental effects on the light field due the interaction with the optical medium. We use this effective description of the laser light field in chapter 3 to study the dynamics of several lasers coupled in an array.

1.5.2 Mean light field

We start by discussing the dynamics of the mean light field, which captures the time evolution of the expectation value $\langle \hat{a} \rangle$.

The mean light field α is described by the equation of motion

$$\dot{\alpha} = \left(-i\omega - \gamma + \frac{g}{1 + |\alpha|^2 / I_{\mathrm{sat}}} \right) \alpha, \tag{1.5.2}$$

obtained by omitting the stochastic term α_{in} in the Langevin equation (1.5.1). We first note that the equation of motion exhibits a $U(1)$ symmetry, i.e. it is invariant under the transformation $\alpha \to \alpha e^{i\phi}$, where ϕ is an arbitrary phase. Due to the $U(1)$ symmetry, it is convenient to split the complex optical amplitude α to an amplitude A and a phase φ, where $\alpha = A e^{i\varphi}$. We can write equations of motion for the amplitude A and the phase φ

$$\dot{A} = \left(-\gamma + \frac{g}{1 + A^2 / I_{\mathrm{sat}}} \right) A, \tag{1.5.3}$$

$$\dot{\varphi} = -\omega. \tag{1.5.4}$$

We can see that the equations of motion for the amplitude A and the phase φ are decoupled. The phase φ evolves with the constant angular velocity ω.

Inspecting the equation of motion (1.5.3), we can see that the amplitude A has a stationary value $A = 0$. If the gain g is smaller than losses γ, the amplitude decays to zero as $\dot{A} < 0$ for any A. As a result, $A = 0$ is a unique steady state as A has no other stationary values for $g < \gamma$. We conclude that if the gain g is smaller than the decay rate γ, the complex optical amplitude spirals towards $\alpha = 0$. It represents a unique stable steady state with a vanishing coherent occupation of the light field in the cavity.

If the gain exceeds the threshold value $g = \gamma$, a second stationary amplitude $A = \sqrt{I_{\mathrm{sat}} \left(\frac{g}{\gamma} - 1 \right)}$ emerges. Now the stationary amplitude $A = 0$ is unstable as $\dot{A} > 0$ for

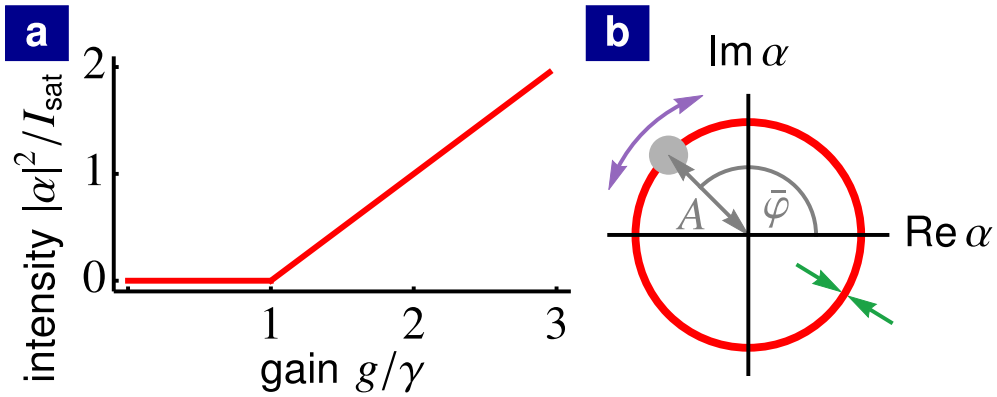

Figure 1.5.1: Asymptotic behavior of the mean light field α. (a) Intensity of the light field $|\alpha|^2$ as a function of the optical gain g taking finite values above the threshold value of the gain $g = \gamma$. (b) Stationary complex amplitudes α (red circle) in phase space in a rotating frame with the frequency ω. The stationary complex amplitude α acquires a certain phase $\bar{\varphi}$ determined by initial conditions. The amplitude A relaxes towards its stationary value (green arrows). The phase φ is an undamped degree of freedom (purple arrows).

$0 < A < \sqrt{I_{\rm sat}\left(\frac{g}{\gamma}-1\right)}$. The amplitude converges towards the stationary value $A = \sqrt{I_{\rm sat}\left(\frac{g}{\gamma}-1\right)}$ for any $A \neq 0$ as also $\dot{A} < 0$ for $A > \sqrt{I_{\rm sat}\left(\frac{g}{\gamma}-1\right)}$. We conclude that $\alpha(t) = \sqrt{I_{\rm sat}\left(\frac{g}{\gamma}-1\right)}\, e^{-i\omega t + i\bar{\varphi}}$ is a stable limit cycle, where the phase $\bar{\varphi}$ is determined by initial conditions. The intensity of the light field $|\alpha|^2 = I_{\rm sat}\left(\frac{g}{\gamma}-1\right)$ is depicted in Fig. 1.5.1a as a function of the optical gain g. For $g > \gamma$, the laser amplification via stimulated emission leads to a coherent population of the light field. In Fig. 1.5.1b, we plot the stationary amplitude $\alpha(t)$ in phase space in a rotating frame with the frequency ω. The $U(1)$ symmetry of the equation of motion (1.5.2) is spontaneously broken and the complex amplitude acquires a specific phase $\bar{\varphi}$, determined by initial conditions.

Investigating the Jacobian matrix

$$\mathbf{J} = \begin{pmatrix} \frac{\partial \dot{A}}{\partial A} & \frac{\partial \dot{A}}{\partial \varphi} \\ \frac{\partial \dot{\varphi}}{\partial A} & \frac{\partial \dot{\varphi}}{\partial \varphi} \end{pmatrix}\Bigg|_{A=\sqrt{I_{\rm sat}\left(\frac{g}{\gamma}-1\right)}} = \begin{pmatrix} -\bar{\gamma} & 0 \\ 0 & 0 \end{pmatrix}, \tag{1.5.5}$$

we can determine the rate $\bar{\gamma} = 2\gamma\left(1-\frac{\gamma}{g}\right)$ with which the complex optical amplitude

α converges towards the limit cycle. The Jacobian matrix also describes the dynamics in the vicinity of the limit cycle (red line in Fig. 1.5.1b). The amplitude A is damped towards its stationary value (green arrows) at the rate $\bar{\gamma}$. The oscillation phase φ is an undamped degree of freedom (purple arrows) corresponding to the vanishing eigenvalue of the Jacobian matrix.

Studying the mean light field, we discussed the fundamental behavior of a laser light field. Below threshold $g < \gamma$, the complex optical amplitude relaxes at a vanishing value since optical losses are larger than the optical gain. As a result, the light field has a vanishing coherent population. Above threshold $g > \gamma$, the gain overcomes losses and a coherent population of the light field builds up. The optical amplitude starts performing limit-cycle oscillations with a constant amplitude. The oscillation phase is an undamped degree of freedom, which is a characteristic feature of limit-cycle oscillations that we have seen already for the van-der-Pol oscillator in section 1.3.

1.5.3 Fluctuations of a light field

We now study fluctuations of a light field in a laser. We discuss two cases: (i) fluctuations for a vanishing mean light field below threshold and (ii) fluctuations around a coherent mean field above threshold.

Well below threshold, $g \ll \gamma$, the optical amplitude $|\alpha(t)|$ is small compared to the saturation amplitude $\sqrt{I_{\mathrm{sat}}}$ and the dynamics of the complex amplitude α is well described by the linearized Langevin equation of motion

$$\dot{\alpha} = (-i\omega - \gamma + g)\,\alpha + \sqrt{q}\alpha_{\mathrm{in}}. \tag{1.5.6}$$

The linearized Langevin equation of motion is obtained from the full Langevin equation (1.5.1) by omitting second- and higher-order terms in α. The solution of the linearized Langevin equations is

$$\alpha(t) = \sqrt{q}e^{-i\omega t-(\gamma-g)t}\int_0^t \mathrm{d}\tau\, e^{i\omega\tau+(\gamma-g)\tau}\alpha_{\mathrm{in}}(\tau), \tag{1.5.7}$$

assuming that any initial excitations present at time $t = -\infty$ were already damped away at time $t = 0$. The intra-cavity field α is driven by the input noise α_{in} and the optical gain leads only to a decrease in the effective decay rate $\gamma - g$. The coherent

population of the cavity vanishes, $\langle\alpha(t)\rangle = 0$, and the mean number of photons in the cavity is $\langle|\alpha(t)|^2\rangle = \frac{q}{2(\gamma-g)}$.

To study fluctuations well above threshold, we can decompose the complex optical amplitude $\alpha = (\bar{\alpha} + \delta\alpha)\, e^{-i\omega t}$ into the mean amplitude $\bar{\alpha} = \sqrt{I_{\mathrm{sat}}\left(\frac{g}{\gamma} - 1\right)} e^{i\bar{\varphi}}$ and a modulation $\delta\alpha$. Due to the $U(1)$ symmetry of the mean optical field, it is convenient to express the modulation $\delta\alpha$ in terms of amplitude fluctuations δA and phase fluctuations $\delta\varphi$, where $\alpha = \left(\bar{A} + \delta A\right) e^{i(-\omega t + \bar{\varphi} + \delta\varphi)}$ and $\bar{\alpha} = \bar{A} e^{i\bar{\varphi}}$. Well above threshold $g \gg \gamma$, amplitude fluctuations δA and phase fluctuations $\bar{A}\delta\varphi$ are small compared to the mean optical amplitude $\bar{A}$ and they can be described by linearized Langevin equations

$$\delta\dot{A} = -\bar{\gamma}\delta A + \sqrt{\frac{q}{2}} A_{\mathrm{in}}, \tag{1.5.8}$$

$$\delta\dot{\varphi} = \sqrt{\frac{q}{2\bar{A}^2}} \varphi_{\mathrm{in}}, \tag{1.5.9}$$

where $\bar{\gamma} = 2\gamma\left(1 - \frac{\gamma}{g}\right)$, $A_{\mathrm{in}} = \sqrt{2}\mathrm{Re}\,\alpha_{\mathrm{in}}$ and $\varphi_{\mathrm{in}} = \sqrt{2}\mathrm{Im}\,\alpha_{\mathrm{in}}$ [32]. The input noise obeys the following correlations $\langle A_{in}(t) A_{in}(t')\rangle = \delta(t - t')$ and $\langle \varphi_{in}(t)\varphi_{in}(t')\rangle = \delta(t - t')$.

Amplitude fluctuations are damped with the rate $\bar{\gamma}$, which is approximately $\bar{\gamma} \approx 2\gamma$ well above threshold $g \gg \gamma$. Assuming that any initial deviation $\delta A(-\infty)$ from the stationary amplitude $\bar{A}$ has decayed, amplitude fluctuations have the following solution

$$\delta A(t) = \sqrt{\frac{q}{2}} e^{-\bar{\gamma}t} \int_0^t \mathrm{d}\tau\, e^{\bar{\gamma}\tau} A_{\mathrm{in}}(\tau). \tag{1.5.10}$$

The relative strength of amplitude fluctuations $\langle\delta A^2\rangle = \frac{q}{4\bar{\gamma}} \approx \frac{q}{8\gamma}$ compared to the coherent mean-field occupation $\bar{A}^2 = I_{\mathrm{sat}}\left(\frac{g}{\gamma} - 1\right) \approx I_{\mathrm{sat}}\frac{g}{\gamma}$ decreases with the optical gain g.

Above threshold, the phase φ is an undamped degree of freedom as we discussed in the previous subsection. As a consequence, also fluctuations of the phase are undamped, see equation (1.5.9). Undamped phase fluctuation $\delta\varphi(t) = \delta\varphi(0) + \sqrt{\frac{q}{2\bar{A}^2}} \int_0^t \mathrm{d}\tau\, \varphi_{\mathrm{in}}(\tau)$ lead to a diffusion of the phase φ

$$\langle[\varphi(t) - \varphi(t')]^2\rangle = \langle[\delta\varphi(t) - \delta\varphi(t')]^2\rangle = D|t - t'|, \tag{1.5.11}$$

with the diffusion constant $D = \frac{q}{2A^2}$.

In this subsection, we studied fluctuations of the light field in a laser. Below threshold, fluctuations are damped with an effective damping rate, which is smaller than the rate of intrinsic optical losses due to the optical gain. Above threshold, amplitude fluctuations and phase fluctuations have a qualitatively different behavior as a coherent mean field builds up in the cavity. On the one hand, amplitude fluctuations are damped and their relative strength compared to the coherent mean-field occupation decreases with the optical gain g. On the other hand, phase fluctuations are undamped and they lead to a diffusion of the optical phase. The diffusion of an oscillation phase due to undamped phase fluctuations is a generic feature of limit-cycle oscillations. The presence of an undamped degree of freedom, which is represented by the phase, is a consequence of the fact that the $U(1)$ symmetry of the light field is spontaneously broken above threshold. The undamped degree of freedom is analogous to a Goldstone mode, which is associated with undamped long-range fluctuations in spatially extended systems with a spontaneously broken continuous symmetry [49].

1.5.4 Nature of laser light

In this subsection, we focus on the coherence properties of the light field in a laser, which are important for laser applications [45]. In particular, we study non-equal-time autocorrelations of the optical amplitude and the optical intensity.

Below threshold, the light field is only driven by the Gaussian input noise, see equation (1.5.7). As a result, the light field inherits the Gaussian statistics of the input noise. The non-equal-time autocorrelation of the optical amplitude α is

$$\begin{aligned}\langle \alpha(t)\alpha^*(t+\Delta t)\rangle &= q e^{i\omega\Delta t-(\gamma-g)(2t+\Delta t)} \int_0^t \mathrm{d}\tau \int_0^{t+\Delta t} \mathrm{d}\tau'\, e^{i\omega(\tau-\tau')+(\gamma-g)(\tau+\tau')} \langle \alpha_{\mathrm{in}}(\tau)\alpha_{\mathrm{in}}^*(\tau')\rangle \\ &= \frac{q}{2(\gamma-g)}\, e^{i\omega\Delta t-(\gamma-g)|\Delta t|}. \end{aligned} \tag{1.5.12}$$

The second-order autocorrelation function

$$g^{(2)}(\Delta t) = \frac{\langle \alpha(t)\alpha(t+\Delta t)\alpha^*(t+\Delta t)\alpha^*(t)\rangle}{\langle \alpha(t)\alpha^*(t)\rangle \langle \alpha(t+\Delta t)\alpha^*(t+\Delta t)\rangle} \tag{1.5.13}$$

determines the relative strength of correlations between the optical intensity $|\alpha(t)|^2$ at

time t and the optical intensity $|\alpha(t+\Delta t)|^2$ at time $t+\Delta t$ [32]. Due to the Gaussian nature of the light field α, we can express the second-order autocorrelation function as

$$g^{(2)}(\Delta t) = 1 + \frac{|\langle \alpha(t)\alpha^*(t+\Delta t)|^2}{|\langle \alpha(t)\alpha^*(t)\rangle|^2} = 1 + e^{-2(\gamma - g)|\Delta t|}, \tag{1.5.14}$$

where we used Wick's theorem and equation (1.5.12) in the first equality and in the second equality, respectively [32]. We can see that $g^2(0) = 2$ and the second-order autocorrelation function decays to unity for a large time difference Δt. Below threshold, the light field has a characteristic Gaussian nature with equal-time intensity correlations $g^2(0) = 2$ and vanishing intensity correlations for a large time difference Δt.

We saw in the previous subsection that the nature of fluctuations in the laser light field qualitatively changes above threshold. This also leads to a qualitative change in the coherence properties. The non-equal-time autocorrelation of the optical amplitude can be written as

$$\langle \alpha(t)\alpha^*(t+\Delta t)\rangle = \langle \left[\bar{A} + \delta A(t)\right]\left[\bar{A} + \delta A(t+\Delta t)\right] e^{i[\omega\Delta t + \delta\varphi(t) - \delta\varphi(t+\Delta t)]}\rangle, \tag{1.5.15}$$

using the decomposition of the complex optical amplitude $\alpha = \left(\bar{A} + \delta A\right) e^{i(-\omega t + \bar{\varphi} + \delta\varphi)}$ into amplitude fluctuations δA and phase fluctuations $\delta\varphi$ around the coherent mean field $\bar{\alpha}(t) = \bar{A}e^{-i\omega t + \bar{\varphi}}$. Well above threshold, amplitude fluctuations $\delta A(t)$ are small compared to the coherent mean light field $\bar{A}$ and they can be neglected

$$\langle \alpha(t)\alpha^*(t+\Delta t)\rangle \approx \bar{A}^2 e^{i\omega\Delta t}\langle e^{i[\delta\varphi(t) - \delta\varphi(t+\Delta t)]}\rangle = \bar{A}^2 e^{i\omega\Delta t} e^{-\frac{1}{2}\langle[\delta\varphi(t) - \delta\varphi(t+\Delta t)]^2\rangle} \tag{1.5.16}$$

$$= \bar{A}^2 e^{i\omega\Delta t - |\Delta t|/\tau_c}, \tag{1.5.17}$$

where $\tau_c = \frac{2}{D} = \frac{4\bar{A}^2}{q}$ is the coherence time. In the second equality on the line (1.5.16), we used the property of Gaussian fluctuations $\langle e^x\rangle = e^{\langle x^2\rangle/2}$ as the phase fluctuations $\delta\varphi$ are Gaussian [32]. In the equality (1.5.17), we used equation (1.5.11). The time delay Δt, for which the light field $\alpha(t+\Delta t)$ still coherently interferes with itself $\alpha(t)$, is limited due to the diffusion of the optical phase at rate $D = \frac{q}{2\bar{A}^2}$. The autocorrelation $|\langle \alpha(t)\alpha^*(t+\Delta t)\rangle|$ exponentially decays due to the phase diffusion. For time delays Δt that are much shorter than the coherence time τ_c, the light field $\alpha(t+\Delta t)$ still coherently interferes with itself $\alpha(t)$ and the autocorrelation $|\langle \alpha(t)\alpha^*(t+\Delta t)\rangle| \approx \langle|\alpha(t)|\rangle^2 = \bar{A}^2$

is almost unchanged. For time delays that are much longer than the coherence time, the coherence of the light field is lost as the autocorrelation $\langle \alpha(t)\alpha^*(t+\Delta t)\rangle$ vanishes. Since the rate $D = \frac{q}{2\bar{A}^2}$ of the phase diffusion is inversely proportional to the intensity $\bar{A}$ of the light field, the phase diffusion can be very slow for large intensities. In that case, the light field has a very long coherence time. The relation $\tau_c = \frac{4\bar{A}^2}{q}$ between the coherence time τ_c and the intensity $\bar{A}^2$ of the laser light field was first described by Schawlow and Townes [50].

The second-order autocorrelation function is determined by amplitude fluctuations

$$g^{(2)}(\Delta t) = \frac{\langle \left[\bar{A} + \delta A(t)\right]^2 \left[\bar{A} + \delta A(t+\Delta t)\right]^2 \rangle}{\langle \left[\bar{A} + \delta A(t)\right]^2 \rangle \langle \left[\bar{A} + \delta A(t+\Delta t)\right]^2 \rangle}. \tag{1.5.18}$$

Well above threshold, the amplitude fluctuations δA are small compared to the coherent mean field occupation $\bar{A}$ and the leading order in the second-order autocorrelation function is

$$g^{(2)}(\Delta t) = 1 + \frac{4}{\bar{A}^2}\langle \delta A(t)\delta A(t+\Delta t)\rangle + \mathcal{O}\left(\frac{1}{\bar{A}^4}\right) = 1 + \frac{q}{\bar{\gamma}\bar{A}^2} e^{-\bar{\gamma}|\Delta t|} + \mathcal{O}\left(\frac{1}{\bar{A}^4}\right), \tag{1.5.19}$$

where we used equation (1.5.10) in the second equality. We can see that intensity correlations decay to unity at time $t \sim \frac{1}{\bar{\gamma}} \approx \frac{1}{2\gamma}$, which is much shorter than the coherence time τ_c. Intensity correlations are suppressed as the amplitude fluctuations are small compared to the coherent mean field $\bar{A}$. Well above threshold, we can reach vanishingly small intensity correlations with $g^{(2)}(0) \approx 1$.

Lasers are widely used sources of coherent light as the laser light field has a long coherence time and vanishing intensity correlations well above threshold [45]. We can use a semi-infinite waveguide to outcouple the light field from a laser. It is desirable that the coupling γ_{out} to the waveguide is strong compared to intrinsic optical losses such that $\gamma \approx \gamma_{\text{out}}$. The light field emitted into the waveguide $\alpha_{\text{out}} = \alpha_{\text{in}} - \sqrt{2\gamma}\alpha$ is directly related to the light field α inside the laser by the input-output relation (1.4.18). For a laser driven well above threshold, the large coherent field α represents the dominant contribution to the emitted light field $\alpha_{\text{out}} \approx -\sqrt{2\gamma}\alpha$.

The light field in a laser has very different coherence properties below and above the lasing threshold. Below threshold, the light field is only driven by the input noise and, as

a consequence, it inherits Gaussian statistics of the input noise. Amplitude correlations vanish for a time delay comparable to the ringdown time of the laser cavity, which is the inverse of the cavity decay rate. Intensity correlations are large for small time delays and they decay to unity for time delays comparable to the cavity ringdown time. On the other hand, well above threshold, the coherence time of the light field is only limited by the diffusion of the optical phase. Since the diffusion constant is inversely proportional to the intensity of the light field for large intensities, we can reach coherence times that are much longer than the ringdown time of the laser cavity. Intensity fluctuations are suppressed for large intensities of the laser light field. As a result, lasers pumped well above threshold are excellent sources of coherent light [45].

1.6 *Intermezzo*: Quantum van-der-Pol oscillator

In this intermezzo, we consider again the van-der-Pol oscillator, which is an archetypical model employed to investigate nonlinear limit-cycle oscillations. In section 1.3, we studied the mean oscillation amplitude of the van-der-Pol oscillator, focusing on its time evolution and the emergence of limit-cycle oscillations. Now we employ a quantum model of the van-der-Pol oscillator to investigate effects of quantum fluctuations on limit-cycle oscillations.

In particular, we consider the quantum van-der-Pol oscillator [51, 52] described by the master equation in Lindblad form

$$\dot{\hat{\rho}} = -i\left[\Omega\,\hat{b}^\dagger\hat{b},\hat{\rho}\right] + \gamma_1\mathcal{D}[\hat{b}^\dagger]\hat{\rho} + \gamma_2\mathcal{D}[\hat{b}^2]\hat{\rho} = \mathcal{L}\hat{\rho}, \tag{1.6.1}$$

where $\hat{b}$ is the annihilation operator, $\hat{\rho}$ is a density matrix describing the state of the van-der-Pol oscillator and $\mathcal{L}$ is the Lindbladian superoperator. The oscillator has a natural frequency Ω and it experiences negative damping, $\mathcal{D}[\hat{b}^\dagger]$, and nonlinear damping, $\mathcal{D}[\hat{b}^2]$, with rates γ_1 and γ_2, respectively.

Even though implementations of the quantum van-der-Pol oscillator have been proposed using trapped ions [51] and optomechanical systems [52], these proposals remain experimentally very challenging and they are still awaiting an experimental realization. Despite the fact that it has not been experimentally realized yet, the quantum van-der-Pol oscillator is a very useful theoretical model for studying the effects of quantum

fluctuations on limit-cycle oscillations. It has been employed to investigate how quantum fluctuations affect the nonlinear phenomenon of synchronization [51, 52, 53, 54] as well as a critical response close to the onset of limit-cycle oscillations [55]. We use the quantum van-der-Pol oscillator in chapter 2 to study the effects of quantum fluctuations on the nonlinear dynamics of synthetic gauge fields.

The relative strength of quantum fluctuations compared to the mean amplitude $b = \mathrm{Tr}\left[\hat{\rho}\hat{b}\right]$ is controlled by a single parameter $\frac{\gamma_1}{\gamma_2}$ [52]. For $\gamma_1 \gg \gamma_2$, the strength of fluctuations is small compared to the mean amplitude b. As a consequence, the higher-order moment $\mathrm{Tr}\left[\hat{\rho}\hat{b}^\dagger\hat{b}^2\right] \approx |b|^2 b$ factorizes and we can derive the equation of motion (1.3.1) for the mean amplitude b. We showed in section 1.3 that any solution of the equation of motion (1.3.1) converges to a limit cycle with the amplitude $b(t) = \sqrt{\frac{\gamma_1}{2\gamma_2}}\, e^{i(\Omega t+\phi_0)}$.

We can find steady states of the van-der-Pol oscillator by solving for the kernel of the Lindbladian superoperator $\mathcal{L}$. To this end, we truncate the infinite dimensional Hilbert space of the oscillator by considering only the N lowest Fock states. We find that the Lindbladian has a single zero-valued eigenvalue and thus the van-der-Pol oscillator has a unique steady state. We plot the Wigner function [56]

$$W(x,p) = \frac{1}{\pi}\int_{-\infty}^{\infty} \mathrm{d}y\, \exp(-2\,i\,y\,p)\langle x+y|\hat{\rho}|x-y\rangle. \tag{1.6.2}$$

of the steady state in figure 1.6.1 for different values of the ratio $\frac{\gamma_1}{\gamma_2}$. The Wigner function represents a quasi-probability distribution of the position $\hat{x} = \hat{b}^\dagger + \hat{b}$ and the momentum $\hat{p} = i\left(\hat{b}^\dagger - \hat{b}\right)$ of the van-der-Pol oscillator in phase space. We can see that the steady-state Wigner function is rotationally symmetric and the phase ϕ of the van-der-Pol oscillator is completely diffused, where $b = Be^{i\phi}$. This is a consequence of the fact that, during limit-cycle oscillations, the phase ϕ is undamped as we have discussed in section 1.3. We showed in the previous section on the example of a light field in a laser that undamped fluctuations in the oscillation phase of a limit-cycle oscillator lead to a diffusion of the phase. In the same way, the phase ϕ of the van-der-Pol oscillator is diffused.

For large values of the ratio $\frac{\gamma_1}{\gamma_2} \gg 1$, the relative strength of quantum fluctuations is small. We refer to this regime as classical. In this regime, the maximum of the steady state Wigner function coincides with the trajectory (black line in figure 1.6.1a) of the

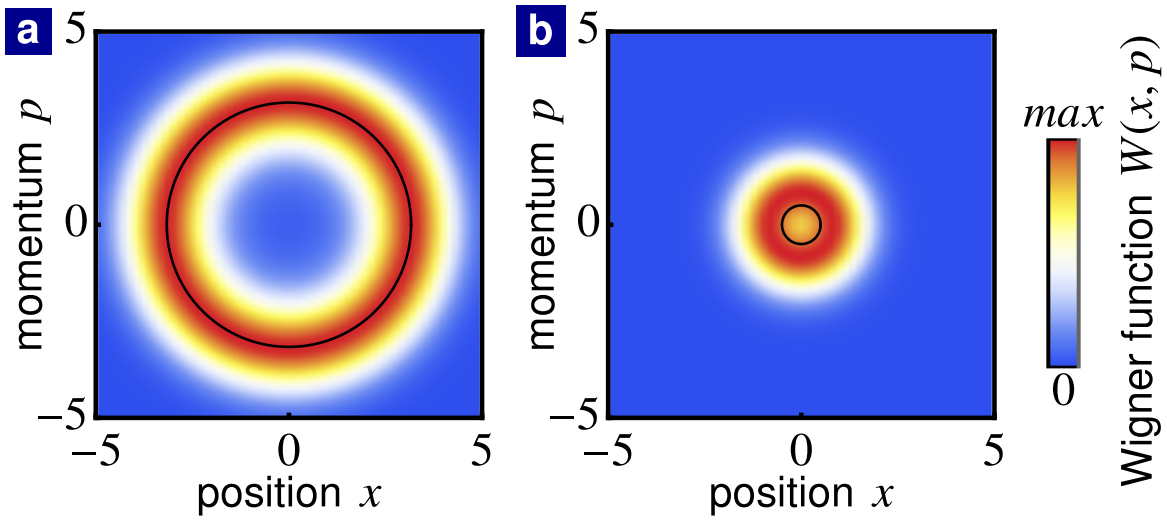

Figure 1.6.1: Steady-state Wigner function of the quantum van-der-Pol oscillator for different values of the ratio $\frac{\gamma_1}{\gamma_2}$. Black lines show the mean amplitude b according to the classical equation of motion (1.3.1). (Parameters: (a) $\gamma_1/\gamma_2 = 10$; (b) $\gamma_1/\gamma_2 = 0.25$; Truncation: $N = 20$)

mean amplitude b according to the equation of motion (1.3.1). The steady state of the van-der-Pol oscillator can be described by Gaussian fluctuations distributed along the trajectory of the mean amplitude b [57].

For small values of the ratio $\frac{\gamma_1}{\gamma_2} \ll 1$, quantum fluctuations are strong compared to the mean amplitude b and we refer to this regime as quantum. We can see in figure 1.6.1b that the trajectory of the mean amplitude b according to the equation of motion (1.3.1) deviates from the maximum of the Wigner function. For $\frac{\gamma_1}{\gamma_2} \ll 1$, the quantization of van-der-Pol-oscillator energy levels is important. The nonlinear dissipation leads to two-particle decay. As a result, the first excited state $|1\rangle$ cannot directly decay to the vacuum state $|0\rangle$. This leads to a finite amplitude $b = \sqrt{\frac{1}{3}}$ even in the limit of a very large nonlinear decay, $\frac{\gamma_1}{\gamma_2} \to 0$. The equation of motion (1.3.1) predicts a vanishing mean amplitude b for $\frac{\gamma_1}{\gamma_2} \to 0$, since it does not take the quantization of energy levels into account. As a result in the quantum regime for $\frac{\gamma_1}{\gamma_2} \ll 1$, the dynamics of the mean amplitude b and fluctuations around it cannot be separated as in the classical regime. In the quantum regime, the quantum van-der-Pol oscillator has to be described by the master equation (1.6.1) to correctly take quantum fluctuations into account.

In this intermezzo, we introduced the quantum van-der-Pol oscillator and we dis-

cussed its steady state. The relative strength of quantum fluctuations in the van-der-Pol oscillator is controlled by a single parameter. In the classical regime, the van-der-Pol oscillator can be well described by an equation of motion for the mean value of the oscillation amplitude. In the quantum regime, this classical description breaks down and quantum fluctuations have to be taken into account using the master-equation formalism. For these reasons, the quantum van-der-Pol oscillator is a suitable model to study effects of quantum fluctuations on limit-cycle oscillations in the quantum regime and on the crossover between the classical and the quantum regime.

1.7 Cavity optomechanics

In this section, we discuss the optomechanical interaction between light and mechanical oscillators. The optomechanical interaction has been implemented in a wide variety of mechanical oscillators, ranging from trapped atoms to kilogram-scale mirrors in Laser Interferometer Gravitational-Wave Observatory (LIGO). Here we discuss optomechanical concepts, which are important for research presented in chapter 2. Since we do not provide an exhaustive introduction to the field of optomechanics, we refer the reader to an extensive review [6] for more details. The coupling of a mechanical oscillator to an optical mode allows for employing well-established experimental techniques for optical systems to control the motion of the mechanical oscillator. We are particularly interested in the situation when a mechanical oscillator is driven via the optomechanical interaction with an optical mode into self-sustained oscillations, which are another example of limit-cycle oscillations.

A standard optomechanical setup is depicted in figure 1.7.1. It consists of a Fabry-Perot cavity with a movable mirror (green rectangle), which represents a mechanical oscillator. For a Fabry-Perot cavity with a large free spectral range, we can focus only on a single resonance. The resonant frequency of the cavity depends on the position x of the movable mirror $\omega_c(x) = \omega_c(0) + \frac{\partial \omega_c}{\partial x} x + \mathcal{O}(x^2)$, where $x = 0$ is the rest position of the movable mirror. At the same time, photons induce the radiation pressure force on the movable mirror, while reflecting from it. This results in the coupling between an optical field inside the cavity and the position of the mechanical oscillator, which is represented by the movable mirror. This optomechanical coupling is described by the

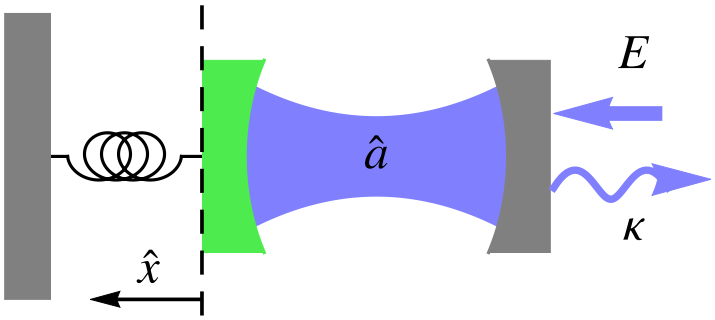

Figure 1.7.1: Standard optomechanical setup consisting of a Fabry-Perot cavity with a movable mirror (green rectangle). The position of the movable mirror $\hat{x}$ couples to the intra-cavity field $\hat{a}$, which is driven by a laser with the amplitude E. The intra-cavity field experiences optical losses κ.

Hamiltonian

$$\hat{H} = \omega_c \hat{a}^\dagger \hat{a} + \Omega \hat{b}^\dagger \hat{b} - g_0 \hat{a}^\dagger \hat{a} \left(\hat{b} + \hat{b}^\dagger\right), \tag{1.7.1}$$

where $\hat{a}$ is the annihilation operator of the optical field, $\omega_c = \omega_c(0)$ and Ω is the frequency of the mechanical oscillator [6]. The position operator $\hat{x} = x_{\mathrm{zpf}} \left(\hat{b} + \hat{b}^\dagger\right)$ of the mechanical oscillator can be expressed in terms of the annihilation operator $\hat{b}$ and the creation operator $\hat{b}^\dagger$, where $x_{\mathrm{zpf}} = \sqrt{\hbar/2\Omega m}$ characterizes the strength of mechanical zero-point fluctuations and m is the mass of the mechanical oscillator. The single-photon optomechanical coupling g_0 quantifies the strength of the interaction between a single phonon and a single photon.

Despite a considerable effort to increase the single-photon optomechanical coupling g_0, it is still small compared to intrinsic photon losses κ in most current experiments. As a result, the optomechanical interaction on the level of single photons remains experimentally challenging, even though some experiments finally entered the single-photon coupling regime for the first time [58, 59]. On the other hand, the optomechanical interaction can be enhanced by coherently driving the cavity with a laser, which results in a large number of photons in the cavity. This leads to a considerable radiation pressure and the enhancement of the optomechanical coupling. The laser drive is described by an additional term in the Hamiltonian

$$\hat{H} = \omega_c \hat{a}^\dagger \hat{a} + \Omega \hat{b}^\dagger \hat{b} - g_0 \hat{a}^\dagger \hat{a} \left(\hat{b} + \hat{b}^\dagger\right) + E \left(\hat{a}\, e^{i\omega_d t} + \hat{a}^\dagger e^{-i\omega_d t}\right), \tag{1.7.2}$$

where E is the amplitude of the driving field and ω_d is the driving frequency. The explicit time-dependence of the Hamiltonian can be removed by switching to a rotating frame, $\hat{H} \to \hat{U}\hat{H}\hat{U}^\dagger - i\hat{U}\partial\hat{U}^\dagger/\partial t$ where $\hat{U} = e^{i\omega_d \hat{a}^\dagger \hat{a} t}$. This yields the time-independent Hamiltonian

$$\hat{H} = -\Delta\hat{a}^\dagger\hat{a} + \Omega\hat{b}^\dagger\hat{b} - g_0\hat{a}^\dagger\hat{a}\left(\hat{b} + \hat{b}^\dagger\right) + E\left(\hat{a} + \hat{a}^\dagger\right), \tag{1.7.3}$$

where $\Delta = \omega_d - \omega_c$ is the detuning of the driving frequency from the resonant frequency. The optical field inside the cavity $\hat{a} = \alpha + \delta\hat{a}$ can be split into the mean optical amplitude $\alpha = \langle\hat{a}\rangle$ and fluctuations $\delta\hat{a}$. In the presence of a strong laser drive $E \gg \kappa$, the interaction between fluctuations $\delta\hat{a}$ and the mechanical oscillator can be well described within a linearized regime by the quadratic Hamiltonian

$$\hat{H} = -\Delta\delta\hat{a}^\dagger\delta\hat{a} + \Omega\hat{b}^\dagger\hat{b} - g\left(\delta\hat{a} + \delta\hat{a}^\dagger\right)\left(\hat{b} + \hat{b}^\dagger\right), \tag{1.7.4}$$

and by the corresponding linear Heisenberg equations of motion. The optomechanical interaction $g = \alpha g_0$ between fluctuations $\delta\hat{a}$ and the mechanical oscillator is enhanced by the mean optical field α.

In the linearized regime, radiation pressure due to the mean optical field leads only to a static shift in the rest position of the mechanical oscillator. This in turn results in an effective shift of the optical frequency, $\Delta_{\text{eff}} \approx \Delta + 2g_0^2|\alpha|^2/\Omega$. The coherently-enhanced optomechanical interaction described by the linearized Hamiltonian (1.7.4) leads to dynamical effects on the mechanical oscillator. The first dynamical effect is an effective shift in the mechanical frequency Ω called *optical spring effect* [6]. The second dynamical effect is *optomechanical damping* with rate

$$\Gamma_{\text{opt}} = g^2\left(\frac{\kappa}{\frac{\kappa^2}{4} + (\Delta_{\text{eff}} + \Omega)^2} - \frac{\kappa}{\frac{\kappa^2}{4} + (\Delta_{\text{eff}} - \Omega)^2}\right), \tag{1.7.5}$$

which together with intrinsic mechanical losses Γ contributes to the effective mechanical damping $\Gamma_{\text{tot}} = \Gamma + \Gamma_{\text{opt}}$ [6]. For a red-detuned laser drive $\Delta_{\text{eff}} \approx -\Omega$, the optomechanical damping leads to an increased damping of the mechanical oscillator. This can be understood in the scattering picture: photons from the laser drive have a smaller frequency than the cavity resonant frequency and they can be scattered into the cavity mode by absorbing a phonon from the mechanical oscillator. This results in an effective

damping of the mechanical oscillator. In the so-called resolved-sideband regime $\Omega \gg \kappa$, this effective optomechanical damping is so strong that it can be used to cool the motion of the mechanical oscillator into its ground state [60]. The optomechanical cooling was a very important experimental achievement [7, 8], which has brought optomechanics into the quantum regime. Since then, optomechanical cooling has become routinely used in experiments.

However, in this thesis we are interested in the opposite regime where the laser drive is blue detuned $\Delta_{\text{eff}} > 0$. In the scattering picture, photons from the laser drive have now a larger frequency than the cavity resonant frequency and they are scattered into the cavity mode by emitting a phonon into the mechanical oscillator. Thus the optomechanical damping is negative $\Gamma_{\text{opt}} < 0$ and it can lead to an *optomechanical instability* if it overcomes intrinsic mechanical losses Γ [61]. The linearized description can be still used to determine the onset of the optomechanical instability, for which the effective mechanical damping vanishes $\Gamma_{\text{tot}} = \Gamma + \Gamma_{\text{opt}} = 0$. However, when the mechanical oscillator becomes unstable, any initial fluctuations in the mechanical amplitude are exponentially amplified and the optomechanical interaction can no longer be described in the linearized picture. Due to the nonlinear nature of the optomechanical interaction, the amplification of the mechanical oscillator saturates at a certain mechanical amplitude and the mechanical oscillator ends up performing self-sustained oscillations [61]. These mechanical self-oscillations are another example of limit-cycle oscillations, which play a key role in the research presented in this thesis.

Optomechanically induced self-oscillations share generic features with the quantum van-der-Pol oscillator, which was discussed in the intermezzo, even though optomechanical self-oscillations are, in general, more complicated. Optomechanical self-oscillations are multi-stable as the mechanical amplitude can settle at multiple stationary values [61, 62]. For a strong single-photon optomechanical coupling, the Wigner function of the mechanical oscillator can have negative values [63, 64]. The negativity of the Wigner function is a genuine signature of quantum states, which the quantum van-der-Pol oscillator lacks. However, basic features of optomechanical self-oscillations, when stabilized around a certain stationary amplitude, are well captured by the model of the quantum van-der-Pol oscillator. Quantum fluctuations lead to the diffusion of the oscillation phase and the strength of the quantum fluctuations is controlled by a single parameter [62]. We will use the quantum van-der-Pol oscillator in chapter 2 as a simple model of

mechanical self-oscillations allowing us to study effects of quantum fluctuations on the nonlinear dynamics of synthetic gauge fields.

We focused in this section on the optomechanical interaction between a single optical mode and a single mechanical mode. However, the optomechanical interaction can be used to mutually couple several optical and mechanical modes. In this way, optomechanical arrays of optical and mechanical modes can be implemented. Optomechanical arrays are relevant for the research presented in this thesis. In particular, we are interested in the coupling of multiple optical modes to a mechanical self-oscillator, which can provide a nonlinear interaction between the optical modes. In chapter 2, we study an array of optical modes whose interaction is assisted by a mechanical self-oscillator. In that situation, the phase of the mechanical self-oscillator represents a synthetic dynamical gauge field for photons.

2 Dynamical gauge fields in optomechanical arrays

2.1 Introduction

The field of cavity optomechanics, addressing the interaction between light and sound, has made rapid strides in recent years [6]. Experiments have shown ground state cooling [7, 8], measurements of motion with record sensitivity [9], efficient conversion between microwave and optical photons [65], dynamics of vibrations near exceptional points [66], squeezing of a mechanical oscillator [10, 11, 12], the control of single phonons [67] and entanglement of mechanical oscillators [13, 68] to name but a few achievements.

Due to the optomechanical interaction, mechanical vibrations can change light frequency. During this process, the mechanical oscillation phase is imparted onto the light field. This provides a natural means to generate synthetic magnetic fields for photons, as was first suggested in Refs. [21, 25]. Together with reservoir engineering [69], these ideas form the theoretical basis underlying a recent series of pioneering experiments on optomechanical nonreciprocity [70, 71, 72, 73, 74, 75]. While those still operate in few-mode setups, future extensions to optomechanical arrays [76, 77, 78, 79] will enable studying photon transport on a lattice in presence of an arbitrary tunable synthetic magnetic field [25]. A similar optomechanical design underlies the first proposal for engineered topological phonon transport [26]. These developments tie into the wide field of synthetic magnetic fields and topologically-protected nonreciprocal transport, first envisaged and implemented for cold atoms [15, 16, 80, 81] and then for photons [17, 18, 19, 20, 22, 23, 24], phonons [26, 27, 28, 29, 82, 83, 84], and other platforms [30, 31].

In these works, gauge fields are fixed by external parameters, e.g., the phases of external driving beams. It was understood only recently that optomechanics provides a very natural platform for creating dynamical classical gauge fields [85]: if the mechanical

resonator is not periodically modulated by external driving but rather undergoes limit-cycle oscillations, the phase of those oscillations becomes a dynamical gauge field. This field is a new degree of freedom that can be influenced by photons.

The theory of *classical* dynamical gauge fields is not only important as a starting point for high-energy *quantum* field theory (e.g. Yang-Mills and Higgs theories [86, 87, 88]), but is also an active area of research in modern condensed matter physics (e.g. in the gauge theory of dislocations [89], spin ice [90] and nematic liquid crystals [91, 92]). We emphasize that our main goal is different from the attempts to build quantum simulators for existing high-energy gauge theories (suggested theoretically for ultra-cold atoms in optical lattices [93, 94], superconducting circuits [95, 96], cavity quantum electrodynamics [97], and trapped ions [98]), where the experimental implementation remains very challenging (see Ref. [99] for the first steps). Rather, our work provides new insight into all physical systems where limit-cycle oscillators assist transitions between linear modes, by connecting these systems to the general mathematical framework of dynamical gauge fields. This includes different kinds of limit-cycles (electrical, mechanical, optical, and spin oscillators, pumped using electrical feedback, optomechanical backaction, etc.), different kinds of linear modes (microwave, mechanical, optical, magnon resonances, etc.), and almost arbitrary nonlinear coupling, using optical or mechanical nonlinearities, Josephson junctions, etc. For concreteness, we describe it here for the case of optomechanics, but the mathematics and the predictions are general and of wide experimental applicability.

In this chapter, we first investigate the classical dynamics of synthetic gauge fields assuming large optical and mechanical amplitudes such that quantum noise can be neglected. This is an excellent approximation for existing optomechanical experiments studying nonlinear dynamics.

If the gauge field dynamics results in a time-dependent vector potential, conventional electromagnetism dictates that this describes an electric field. In this work, we predict that synthetic electric fields can arise in elementary optomechanical systems, in a dynamical way. The scenarios in which these electric fields arise, and their physical consequences, are qualitatively different from the more conventional self-consistently generated magnetic fields discussed in our previous work [85]. They can arise even in a linear arrangement of coupled photon modes, where static vector potentials do not have any effect, since they can be gauged away. This makes them a very relevant

phenomenon for present-day experimental implementations, in setups as simple as two coupled optical modes. Moreover, the appearance of electric fields turns out to depend on the direction of photon propagation. In this way, we uncover a novel mechanism for nonlinear unidirectional transport of photons (a photon diode). This works especially well in arrays, where transport is significantly suppressed in the blockaded direction. This work was published in Ref. [1].

Synthetic electric fields for photons have been previously analyzed only in the context of prescribed external driving [100, 101], i.e. not dynamically generated. In these cases, the nonlinear dynamics and unidirectional transport explored in our work are absent.

In a second step, we consider the quantum dynamics of synthetic gauge fields in optomechanical arrays taking into account quantum fluctuations. We study the minimal setup exhibiting synthetic dynamical gauge fields: two optical modes that are coupled by phonon-assisted tunneling where the phonon mode is undergoing self-oscillations. Cavity optomechanics is approaching the nonlinear quantum regime where a single photon displaces the mechanical oscillator by more than its zero-point uncertainty [102, 103]. This has motivated the theoretical investigation of optomechanically induced self-oscillations in the quantum regime, showing that self-oscillations persist even if only a few energy levels are occupied [62, 63, 64, 104, 105, 106]. In particular, we use the so-called quantum van-der-Pol oscillator [51, 52] as a model of mechanical self-oscillations. We show that in our model the strength of quantum fluctuations is controlled by a single parameter. By tuning the strength of quantum fluctuations, we explore the classical-to-quantum crossover, an analysis which has been carried out for the standard optomechanical setup [53, 62]. We show that the phase of the mechanical oscillator is very sensitive to noise and as a consequence its value is washed out deep in the quantum regime by quantum fluctuations. However, the mechanical phase still represents a synthetic gauge field for photons, despite being very noisy, since quantum fluctuations do not break the gauge symmetry of the system. We show that even though the value of the mechanical phase is washed out in the quantum regime, its nonlinear dynamics still results in the generation of synthetic electric fields. This demonstrates the robustness of synthetic electric fields against noise, which emerge via a dynamical instability. In contrast to the classical regime, the transition from a vanishing to a finite synthetic electric field is blurred by quantum fluctuations [107]. Sufficiently above threshold,

the synthetic electric field is not affected by fluctuations and thus also the resulting unidirectional light transport is robust against noise. However, the quantization of the van-der-Pol oscillator's energy levels leads to an increased mechanical amplitude with respect to the classical regime, and an increased transmission in the blockaded direction. This results in reduced isolation ratios, which, however, do not preclude unidirectional light transport in arrays. These results are published in Ref. [2].

Our work shows that cavity optomechanics provides a suitable platform for studying both the classical and the quantum dynamics of synthetic gauge fields. In the future, it will allow for the investigation of genuine quantum features in synthetic gauge fields and the interplay of their dynamics with quantum synchronization [51, 52, 53, 54].

2.2 Dynamical gauge fields for photons

The optomechanical interaction can be used to realize phonon-assisted photon tunneling, which, as we have shown previously, offers a natural route towards classical dynamical gauge fields for photons [85]. Photons hopping between optical modes $\hat{a}_1$ and $\hat{a}_2$ absorb or emit a phonon from a mechanical mode $\hat{b}$. A pictorial representation of this process is shown in figure 2.2.1b. Many implementations are conceivable (photonic crystal devices, coupled toroids, and microwave circuits [6]), but a suitable realization might simply consist of the well-known membrane-in-the-middle setup [108, 109]. The Hamiltonian is

$$\hat{H} = \sum_{j=1}^{2} \nu_j \hat{a}_j^\dagger \hat{a}_j + \Omega\, \hat{b}^\dagger \hat{b} + J\left(\hat{b}\hat{a}_2^\dagger \hat{a}_1 + \text{h.c.}\right), \tag{2.2.1}$$

where ν_j are the optical frequencies of modes $\hat{a}_j$, Ω is the frequency of the mechanical oscillator and J is the tunneling amplitude [85]. In the following, we set $\hbar = 1$. The phonon-assisted photon tunneling is selected by tuning the mechanical frequency, $\Omega \approx |\nu_2 - \nu_1|$, see appendix 2.A for a detailed derivation of the Hamiltonian (2.2.1). The Hamiltonian (2.2.1) is valid within the rotating-wave approximation for $\nu_2 > \nu_1$ and $\Omega \gg \kappa, J, JB$, where κ is the photon decay rate and B is the amplitude of the mechanical oscillations: $\langle \hat{b} \rangle = Be^{i\phi}e^{-i\Omega t}$.

During the photon tunneling process $\hat{b}\hat{a}_2^\dagger\hat{a}_1$, the mechanical phase ϕ is imprinted on the photons, similar to an Aharonov-Bohm (Peierls) phase. This can be used for optomechanical generation of static gauge fields, as proposed in Ref. [25], and the scheme

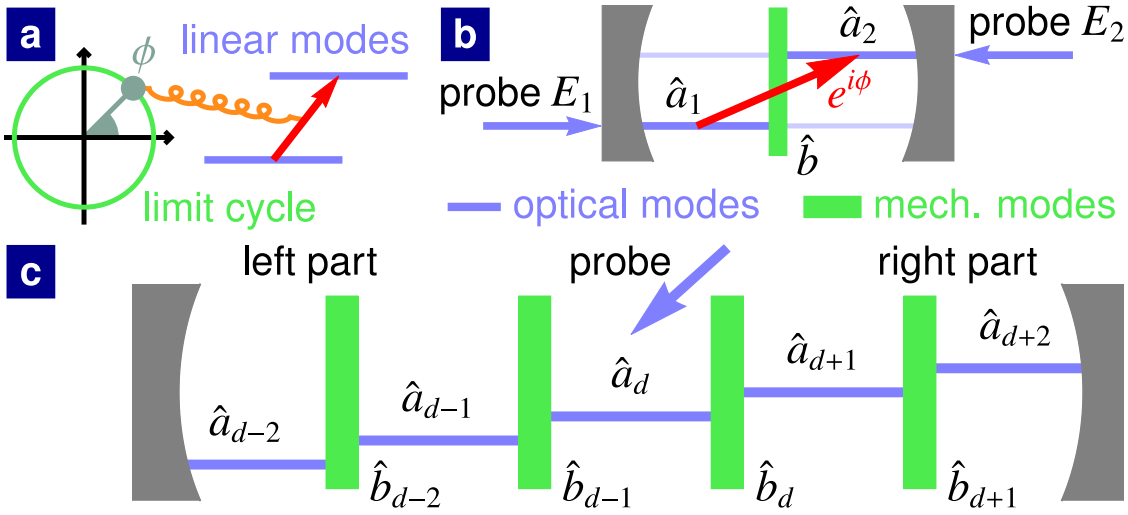

Figure 2.2.1: Setup exhibiting dynamically generated synthetic electric fields. (a) In general terms: limit-cycle oscillator assisting the transition between linear modes. (b) Optomechanical realization: a cavity with a movable membrane (green rectangle) in the middle supporting optical supermodes $\hat{a}_1$ and $\hat{a}_2$ (mostly localized left and right, respectively). The mechanical mode $\hat{b}$ undergoes limit-cycle oscillations. Photons tunneling (red arrow) from optical mode $\hat{a}_1$ to $\hat{a}_2$ absorb a phonon from the mechanical oscillation, thereby acquiring a phase shift set by the oscillation phase ϕ. Photon transport through the setup can be probed by driving mode $\hat{a}_1$ or $\hat{a}_2$. Optical frequencies are represented by the blue lines. (c) A one-dimensional array, with optical modes $\hat{a}_j$ of increasing frequency. Mechanical modes $\hat{b}_j$ assist tunneling between modes $\hat{a}_j$ and $\hat{a}_{j+1}$. Some mode, $\hat{a}_d$, is driven by a laser (blue arrow), probing photon transport both towards the left and right.

can be readily implemented in optomechanical crystals [110, 111] or the membrane-cavity setup [108, 109, 112]. It was experimentally realized in Ref. [73].

To implement dynamical gauge fields for photons, i.e., fields that are themselves dynamical degrees of freedom, the oscillation phase ϕ (the "gauge field") has to evolve freely, which is the case if the mechanical mode performs limit-cycle oscillations [85]. The limit-cycle oscillations can be generated by pumping an ancillary optical mode, situated at a different frequency, on the blue sideband [61]. This pumping does not impose any particular phase on the mechanical oscillator and thus the phase is able to evolve according to its own dynamics. In this way, the phase ϕ turns into a dynamical gauge field, being influenced by photon transport and acting back on photons. The Hamiltonian (2.2.1) can be used as a building block for optomechanical arrays with

dynamical gauge fields for photons, as we first proposed in Ref. [85]. We use the equations of Ref. [85] as our starting point, to predict the new phenomenon of synthetic electric fields generated by nonlinear dynamics, giving rise to unidirectional photon transport.

2.3 The basic physics behind our results

We start with a preview of our results, emphasizing the physical intuition. Any oscillator driven by a resonant force $F_0 \cos(\Omega t - \theta)$ experiences a drift, $\dot{\phi} \propto F_0 \cos(\phi - \theta)$, of its phase ϕ. In our case, the force is the radiation pressure oscillating at the beat note between the two optical modes, and we obtain $\dot{\phi} = -(J/B)\,|a_1|\,|a_2| \cos(\phi - \theta)$, where θ is the phase difference between the optical modes. If the forcing phase θ is kept constant, this results in a stable fixed point $\phi = \theta - \pi/2$. For a limit-cycle oscillator, that behavior is known as phase locking (injection locking) to an external drive (see appendix 2.D for more details).

However, in our case an interesting self-consistency problem arises: the phase difference $\theta = \theta_2 - \theta_1$ of the two optical modes depends on ϕ itself, as the phase ϕ is imprinted onto the photons during the phonon-assisted photon tunneling. The phase of the force thus follows the oscillation phase. We now discuss qualitatively the resulting physics, which will be bolstered by detailed analysis later. Two cases need to be distinguished, depending on which optical mode is driven by the laser (see figure 2.3.1a and figure 2.3.1b). If the higher-frequency optical mode (labeled '2') is driven, then we find $\theta = \phi + \pi/2$. The crucial term $\pi/2$ comes about due to the resonant excitation of the lower-frequency mode via the phonon-assisted transition $2 \to 1$. Comparing with the stable fixed point for ϕ deduced above, we conclude that any value of ϕ is now stable.

The situation drastically changes if the lower-frequency optical mode is driven by the laser. Then, we find $\theta = \phi - \pi/2$, where the sign has flipped because the roles of optical modes have been interchanged (now the higher-frequency mode is excited by the phonon sideband of the driven lower-frequency mode). This corresponds to an unstable fixed point. Once ϕ tries to move away, θ will follow, such that ϕ is forever repelled. This results in a finite phase drift $\dot{\phi} \neq 0$, corresponding to an effective shift of the mechanical frequency. Thus, the phonon-assisted tunneling process towards the higher-

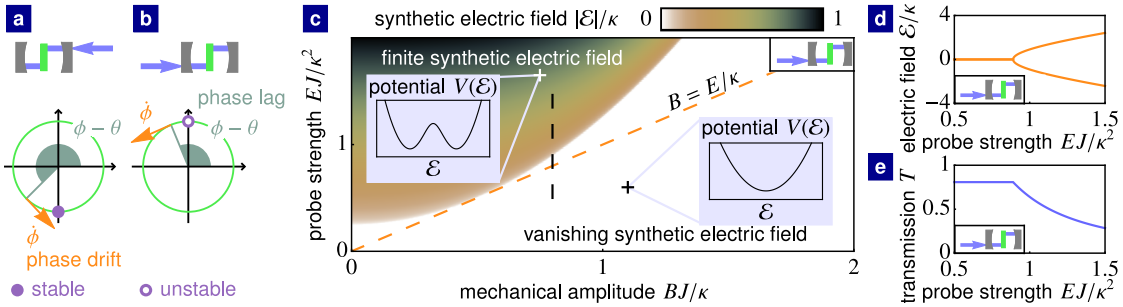

Figure 2.3.1: Dynamically generated synthetic electric fields in the two-site system. (a,b) Phase evolution on the mechanical limit cycle (green orbit). (a) When the higher-frequency optical mode is laser-driven, the system settles into a stable fixed point, with a phase lag $\phi - \theta = -\pi/2$. (b) When the lower-frequency optical mode is driven, the phase is continuously repelled from an unstable fixed point $\phi - \theta = +\pi/2$, generating a finite synthetic electric field $\mathcal{E} = \dot{\phi} \neq 0$ acting on the photons. (c) The phase diagram. In the white region, $\mathcal{E}$ vanishes in the steady state. If the lower-frequency mode, a_1, is driven, $\mathcal{E}$ bifurcates in the colored region to finite steady-state values. Their absolute values are indicated by the color scale. The blue insets show the effective potential $V(\mathcal{E})$ determining the steady-state value of $\mathcal{E}$. The dashed black line denotes the cut along which $\mathcal{E}$ and the optical transmission T are plotted in (d) and (e), respectively. For the higher-frequency mode, a_2, being driven, $\mathcal{E}$ always vanishes for any values of the system parameters. Consequently, the transmission is never suppressed.

frequency optical mode is no longer in resonance but detuned by $\dot{\phi}$. This off-resonant excitation shifts the optical phase difference according to $\theta \approx \phi - \pi/2 - \dot{\phi}/(\kappa/2)$. The equation $\dot{\phi} \propto -\cos(\phi - \theta)$ can then be fulfilled at a certain value of $\dot{\phi}$, which has to be obtained self-consistently. This is the qualitative origin of the nonlinear dynamics that gives rise to what we will identify below as a synthetic electric field $\mathcal{E} = \dot{\phi}$ acting on photons.

2.4 Classical dynamics and synthetic electric fields

Let us analyze the dynamics of the two-site system (2.2.1) with the mechanical oscillator performing limit-cycle oscillations. The optical mode $\hat{a}_j$ is driven by a laser of amplitude E_j at frequency $\nu_{D,j}$, probing photon transport through the system. The optical and mechanical amplitudes are assumed large such that quantum noise can be neglected, which is an excellent approximation for existing optomechanical experiments studying nonlinear dynamics.

Following Ref. [85], the classical equations of motion for the optical amplitudes $a_j = \langle \hat{a}_j \rangle$ and the mechanical phase ϕ read

$$\dot{\phi} = \Delta_{\mathrm{M}} - \frac{J}{B} \mathrm{Re}\left[a_1^* a_2 e^{-i\phi}\right], \tag{2.4.1}$$

$$\dot{a}_1 = i\Delta_1 a_1 - iE_1 - iJBe^{-i\phi} a_2 - \frac{\kappa}{2} a_1, \tag{2.4.2}$$

$$\dot{a}_2 = i\Delta_2 a_2 - iE_2 - iJBe^{i\phi} a_1 - \frac{\kappa}{2} a_2, \tag{2.4.3}$$

where $\Delta_j = \nu_{D,j} - \nu_j$ and $\Delta_{\mathrm{M}} = \nu_{D,2} - \nu_{D,1} - \Omega$ are optical and mechanical detunings, respectively (switching to suitable rotating frames). The mechanical amplitude B is considered fixed. These equations form the starting point of our analysis.

If only one optical mode is driven, no external phase is imprinted. The mechanical oscillator is free to pick any phase despite the interaction with the optical modes. The phase forms a classical gauge field with $U(1)$ symmetry. The gauge transformation

$$\phi \mapsto \phi + \chi_2 - \chi_1, \tag{2.4.4}$$

$$a_j \mapsto a_j e^{i\chi_j}, \text{ for } j = 1, 2, \tag{2.4.5}$$

generates a new valid solution of the dynamical equations, for any real functions $\chi_j(t)$. The transformation also preserves optical and mechanical frequencies whenever it is time-independent, i.e., $\chi_j = \text{const}$. However, if χ_j are time-dependent, equations (2.4.4) and (2.4.5) have to be supplemented by a shift in frequencies: $\Omega \mapsto \Omega + \dot{\chi}_1 - \dot{\chi}_2$ and $\nu_j \mapsto \nu_j - \dot{\chi}_j$. Any time-evolving phase ϕ can be viewed as generating a synthetic electric field

$$\mathcal{E} = \dot{\phi} \tag{2.4.6}$$

for photons. For example, if mode 1 is driven, we can re-gauge using $\chi_1 = 0$, $\chi_2 = -\phi$, which results in a description where the mechanical phase is static but $\nu_2 \mapsto \nu_2 + \mathcal{E}$. This describes an effective optical frequency shift, which can be interpreted as a synthetic electric field for photons in the same way that an energy difference between electronic levels indicates a voltage drop, i.e., a real electric field. In conventional electromagnetism, an electric field can be represented either by a time-dependent vector potential or by a spatially varying potential. Analogically, the synthetic electric field $\mathcal{E}$ is described either by the time-evolution of the mechanical phase or by an effective

frequency shift. As we will show, $\mathcal{E}$ has important consequences for photon transport.

2.5 Dynamical phase diagram

Here, $\mathcal{E}$ is not prescribed externally but it arises due to the dynamics of coupled optical and mechanical modes. The optical modes induce the force F acting on the mechanical phase. The resulting phase evolution may generate a field $\mathcal{E}$ which effectively modifies the optical frequency difference and, consequently, the population of the optical modes.

The results of the dynamical analysis are shown in figure 2.3.1. The results were obtained by linear stability analysis and numerical simulations, see appendix 2.B for more details.

We consider the fully resonant situation where physical effects are most pronounced, as both optical driving and phonon-assisted photon tunneling are resonant ($\Delta_{\mathrm{M}} = \Delta_1 = \Delta_2 = 0$). The system always converges to a steady state. The steady-state value of $\mathcal{E}$ depends on two dimensionless parameters: the rescaled limit-cycle amplitude BJ/κ and the rescaled laser amplitude EJ/κ^2.

The dynamical analysis becomes more intuitive by "integrating out" the optical modes. This leaves us with an effective potential $V(\mathcal{E})$, whose minima determine steady-state values of $\mathcal{E}$ (see appendix 2.B for the full analytical expression):

$$\dot{\mathcal{E}} = -\frac{dV(\mathcal{E})}{d\mathcal{E}} = 0. \tag{2.5.1}$$

In the white region of the phase diagram, figure 2.3.1c, the potential $V(\mathcal{E})$ has a single minimum at $\mathcal{E} = 0$ (see the blue inset). For the lower-frequency mode, a_1, being driven, this steady state becomes unstable in the colored region of the phase diagram, where the potential $V(\mathcal{E})$ has two minima at finite values of $\mathcal{E}$. The field $\mathcal{E}$ can develop such a nonzero value for $B < E/\kappa$ (above the dashed orange line). In terms of physical parameters, the occupation of the driven optical mode has to exceed the phonon number in the limit-cycle oscillation.

In contrast, if the higher-frequency mode, a_2, is driven, $V(\mathcal{E})$ always has a single minimum at $\mathcal{E} = 0$ for any values of system parameters.

The steady states are not qualitatively changed for finite mechanical and laser detunings (see appendix 2.B) as well as for a finite coupling of the laser drive from the left (right) to the optical supermode $\hat{a}_2$ ($\hat{a}_1$), see appendix 2.C.

We now study the effects of the dynamically generated synthetic electric field on light transport. The transmission T is the ratio of the output power leaking from the nondriven mode, $\kappa|a_2|^2$ (if mode 1 is driven) or $\kappa|a_1|^2$ (if mode 2 is driven), and the driving power E^2/κ. We find that

$$T = \frac{\frac{B^2J^2}{\kappa^2}}{\left(\frac{B^2J^2}{\kappa^2} + \frac{1}{4}\right)^2 + \frac{1}{4\kappa^2}\mathcal{E}^2} \tag{2.5.2}$$

is suppressed when a finite field $\mathcal{E}$ detunes the tunneling process from resonance. In figures 2.3.1d and 2.3.1e, $\mathcal{E}$ and T, respectively, are depicted along the cut in figure 2.3.1c denoted by the dashed black line.

When light propagates to higher optical frequencies, the phonon-assisted photon tunneling is suppressed due to the synthetic electric field. In contrast, the field always vanishes when light propagates towards lower optical frequencies. In this way, dynamical gauge fields give rise to a new mechanism for unidirectional light transport.

2.6 Nonlinear unidirectional light transport in a one-dimensional array

The physics of synthetic electric fields also affects photon transport in arrays (figure 2.2.1c). For more details see appendix 2.E.

Figure 2.6.1a shows the result for a 1D array: for a sufficiently large laser drive, the system switches into a state where finite $\mathcal{E}$ develops to the right of the laser drive. This is the direction where photons need to gain energy when tunneling, and where we already saw in the two-site system that (i) a finite field can develop, and (ii) it suppresses photon transport. In the array, this results in a rapid exponential suppression of light intensity. In contrast, light easily propagates towards the left, where $\mathcal{E}$ remains zero. In figure 2.6.1b, we plot the ratio $R = |a_{d-1}/a_{d+1}|^2$ of transmission to the sites adjacent to the driven site $j = d$ as a function of EJ/κ^2. The suppression of light propagation to the right, i.e., $R > 1$, is achieved above the threshold of the laser amplitude. At m sites distance from the driven site, the ratio is exponentially increased to R^m.

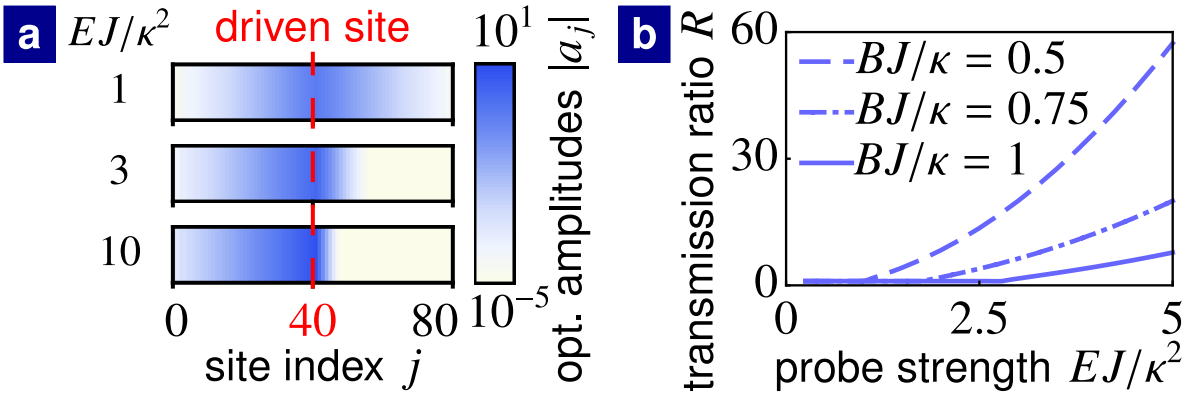

Figure 2.6.1: Light transport in a 1D array with dynamical gauge fields – generation of a barrier for photon transport induced by synthetic electric fields. (a) The optical amplitudes $|a_j|$ as a function of position for different values of the laser amplitude E and $BJ/\kappa = 1$ (shown on a logarithmic scale). The dashed red line denotes the driven site. Transport to the right is strongly suppressed. (b) The ratio $R = |a_{d-1}/a_{d+1}|^2$ of the optical amplitudes adjacent to the driven site $j = d$. (Plotted for $n = 81$ sites, site $d = 40$ being driven.)

2.7 Experimental parameters

In this section, we estimate experimental parameters required for generating the synthetic electric field. We show that unidirectional light transport can be observed for experimentally realistic parameters. For the membrane-in-the-middle setup, feasible parameters are $\kappa \approx 300\,\mathrm{kHz}$, $J \approx 1\,\mathrm{Hz}$, a zero-point fluctuation amplitude of $x_{\mathrm{ZPF}} \approx 10^{-15}\,\mathrm{m}$ and a number of photons in the cavity $(E/\kappa)^2 \sim 10^{10}$ [109]. A typical phonon number in limit-cycle oscillations driven well above threshold is $B^2 \sim (\kappa/J)^2 \sim 10^{10}$ with a corresponding real oscillation amplitude $2x_{\mathrm{ZPF}}B \sim 100\,\mathrm{pm}$ [61]. Optical modes can be represented by hybridized modes of a cavity with avoided crossing [109]. The splitting of their frequencies $\approx 200\,\mathrm{kHz}$ can match the mechanical frequency. For these experimental parameters, $EJ/\kappa^2 \sim 1$ and $BJ/\kappa \sim 1$ are promising for observing unidirectional light transport (see figure 2.3.1). The phonon number can be decreased below the photon number in the driven mode by driving mechanical self-oscillations closer to threshold [61], fulfilling the necessary condition for a finite synthetic electric field (figure 2.3.1).

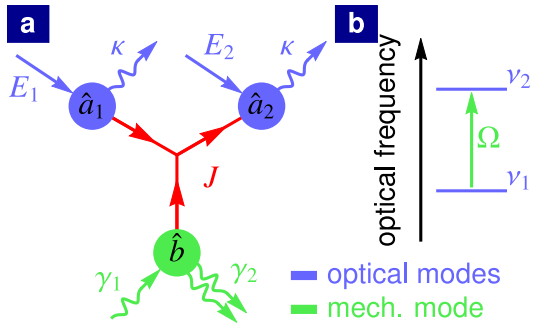

Figure 2.8.1: Quantum model of an optomechanical setup exhibiting a synthetic dynamical gauge field for photons. (a) Red arrows depict tunneling of photons (with tunneling amplitude J) from the optical mode, $\hat{a}_1$, to the optical mode, $\hat{a}_2$, assisted by the coherent absorption of a phonon from the mechanical mode $\hat{b}$. The inverse process happens with the same tunneling amplitude J. The mechanical oscillator performs self-oscillations arising from the competition of linear (one-phonon) anti-damping and nonlinear (two-phonon) damping with rates γ_1 and γ_2, respectively. Photons decay at a rate κ. Optical modes are driven with lasers of amplitudes E_1 and E_2 to study the transmission through the device. (b) Optical frequencies ν_1 and ν_2 satisfy the resonance condition $\Omega \approx \nu_2 - \nu_1$, where Ω is the mechanical frequency.

2.8 Quantum model

We now consider a quantum model of synthetic dynamical gauge fields to take quantum fluctuations into account. The minimal optomechanical setup featuring dynamical gauge fields for photons consists of two optical modes and one mechanical mode, as shown in figure 2.8.1. The tunneling between optical modes $\hat{a}_1$ and $\hat{a}_2$ is assisted by a coherent absorption or emission of a phonon from the mechanical mode $\hat{b}$. This phonon-assisted photon tunneling is described by the Hamiltonian (2.2.1). We now explicitly consider coherent drives of optical modes $\hat{a}_j$ at frequencies $\nu_{D,j}$ and with strengths E_j in the Hamiltonian

$$\hat{H} = -\sum_{j=1}^{2} \Delta_{O,j} \hat{a}_j^\dagger \hat{a}_j - \Delta_M \, \hat{b}^\dagger \hat{b} + J \left(\hat{b} \hat{a}_2^\dagger \hat{a}_1 + \text{h.c.} \right) + \sum_{j=1}^{2} E_j (\hat{a}_j + \hat{a}_j^\dagger), \tag{2.8.1}$$

where $\Delta_{O,j} = \nu_j - \nu_{D,j}$ and $\Delta_M = \Omega - \nu_{D,2} + \nu_{D,1}$ are optical and mechanical detunings. The optical and mechanical modes are expressed in suitable rotating frames.

To implement dynamical gauge fields, the mechanical oscillator is assumed, as in

previous sections, to perform self-sustained oscillations. In this case, the phase ϕ of the mechanical oscillator is able to evolve according to its own dynamics which provides a dynamical gauge field for photons with a $U(1)$ symmetry. Here we employ the quantum van-der-Pol oscillator as a model of the mechanical self-oscillations enabling us to study synthetic dynamical gauge fields in the quantum regime. Two optical modes with tunneling assisted by such a mechanical self-oscillator are described by the following quantum master equation in Lindblad form

$$\dot{\hat{\rho}} = -i\left[\hat{H}, \hat{\rho}\right] + \kappa \sum_{j=1}^{2} \mathcal{D}\left[\hat{a}_j\right]\hat{\rho} + \gamma_1 \mathcal{D}[\hat{b}^\dagger]\hat{\rho} + \gamma_2 \mathcal{D}[\hat{b}^2]\hat{\rho}, \tag{2.8.2}$$

for the composite density matrix ρ, where $\mathcal{D}[\hat{O}]\hat{\rho} = \hat{O}\hat{\rho}\hat{O}^\dagger - \frac{1}{2}\left\{\hat{O}^\dagger\hat{O}, \hat{\rho}\right\}$ and $\{\cdot,\cdot\}$ is the anti-commutator. The Hamiltonian (2.8.1) governs the coherent dynamics of the system. Photon decay at a rate κ is described by the dissipator $\mathcal{D}[\hat{a}_j]$. Self-oscillations of the mechanical mode arise from the competition of two dissipative processes, namely negative damping, $\mathcal{D}[\hat{b}^\dagger]$, and nonlinear damping, $\mathcal{D}[\hat{b}^2]$, with rates γ_1 and γ_2, respectively. Mechanical self-oscillations persist even in the extreme quantum limit, $\gamma_2/\gamma_1 \to \infty$, where only two lowest energy levels are occupied [51, 52]. As a result, the model described by the master equation (2.8.2) allows us to study the dynamics of synthetic gauge fields deep in the quantum regime for low occupations of the mechanical self-oscillator. The master equation (2.8.2) is a starting point for our analysis of dynamical gauge fields in the quantum regime.

2.9 Classical limit and quantum parameter

We start our analysis of the minimal setup with the van-der-Pol oscillator by considering the classical regime of large mechanical and optical occupations when quantum fluctuations are negligible.

In the classical regime, quantum fluctuations and the quantization of energy levels can be neglected for the van-der-Pol oscillator [52] as well as for the optical modes. The system can then be described by equations of motion for the expectation values $\langle\hat{b}\rangle = \mathrm{Tr}\left[\hat{\rho}\hat{b}\right] \equiv b$, $\langle\hat{a}_1\rangle = \mathrm{Tr}\left[\hat{\rho}\hat{a}_1\right] \equiv a_1$, $\langle\hat{a}_2\rangle = \mathrm{Tr}\left[\hat{\rho}\hat{a}_2\right] \equiv a_2$, derived from the quantum master equation (2.8.2). In the classical regime, it is a good approximation to factorize

the higher order moments, $\mathrm{Tr}\left[\hat{\rho}\hat{b}^\dagger\hat{b}^2\right] \approx |b|^2 b$ and $\mathrm{Tr}\left[\hat{\rho}\hat{a}_1^\dagger\hat{a}_2\right] \approx a_1^* a_2$. In this way we obtain a set of classical equations of motion

$$\dot{b} = i\Delta_M b - iJa_1^* a_2 + \frac{\gamma_1}{2}b - \gamma_2|b|^2 b, \tag{2.9.1}$$

$$\dot{a}_k = i\Delta_O a_k - iE - iJ\left(\delta_{1,k}b^* + \delta_{2,k}b\right)a_l - \frac{\kappa}{2}a_k, \tag{2.9.2}$$

$$\dot{a}_l = -iJ\left(\delta_{1,k}b + \delta_{2,k}b^*\right)a_k - \frac{\kappa}{2}a_l, \tag{2.9.3}$$

where we assume that only one optical mode, a_k, is driven, $\Delta_O = \Delta_{O,k}$ and $\delta_{j,k}$ is the Kronecker delta. The detuning, $\Delta_{O,l}$, of the nondriven optical mode, a_l, $(l \neq k)$ can be set to zero in the absence of the laser drive. Using rescaled optical amplitudes $\tilde{a}_j = \kappa a_j/E$, mechanical amplitude $\tilde{b} = Jb/\kappa$ and time $\tilde{t} = \kappa t$, the equations of motion can be expressed as

$$\frac{\mathrm{d}\tilde{b}}{\mathrm{d}\tilde{t}} = i\tilde{\Delta}_M\tilde{b} - i\mathcal{P}\tilde{a}_1^*\tilde{a}_2 + \frac{\tilde{\gamma}_1}{2}\tilde{b} - \tilde{\gamma}_2|\tilde{b}|^2\tilde{b}, \tag{2.9.4}$$

$$\frac{\mathrm{d}\tilde{a}_k}{\mathrm{d}\tilde{t}} = i\tilde{\Delta}_O\tilde{a}_k - i - i\left(\delta_{1,k}\tilde{b}^* + \delta_{2,k}\tilde{b}\right)\tilde{a}_l - \frac{1}{2}\tilde{a}_k, \tag{2.9.5}$$

$$\frac{\mathrm{d}\tilde{a}_l}{\mathrm{d}\tilde{t}} = -i\left(\delta_{1,k}\tilde{b} + \delta_{2,k}\tilde{b}^*\right)\tilde{a}_k - \frac{1}{2}\tilde{a}_l, \tag{2.9.6}$$

which depend on the dimensionless parameters $\tilde{\Delta}_O = \Delta_O/\kappa$, $\tilde{\Delta}_M = \Delta_M/\kappa$, $\tilde{\gamma}_1 = \gamma_1/\kappa$, $\tilde{\gamma_2} = \kappa\gamma_2/J^2$ as well as the rescaled driving power $\mathcal{P} = J^2E^2/\kappa^4$.

However, the classical equations of motion do not depend on the quantum parameter

$$\zeta = \frac{J}{\kappa}, \tag{2.9.7}$$

which has been shown to control the strength of quantum fluctuations in the standard optomechanical setup [53, 62]. Since ζ determines the scaling of the mechanical amplitude, it controls the strength of quantum fluctuations for the van-der-Pol oscillator. The quantum parameter γ_2/γ_1 of the van-der-Pol oscillator [52] can be re-expressed as

$$\frac{\gamma_2}{\gamma_1} = \frac{\tilde{\gamma}_2}{\tilde{\gamma}_1}\zeta^2 \tag{2.9.8}$$

in terms of the standard optomechanical quantum parameter ζ and the two classical

parameters $\tilde{\gamma}_1$ and $\tilde{\gamma}_2$. As a result, the strength of quantum fluctuations in our model with the quantum van-der-Pol oscillator is controlled by the quantum parameter ζ.

In the classical regime, where quantum fluctuations are negligible, the optical and mechanical amplitudes can be rescaled and the system dynamics is described by the rescaled equations of motion (2.9.4), (2.9.5) and (2.9.6). These classical equations are similar to equations (2.4.1), (2.4.2) and (2.4.3) studied in sections 2.4 and 2.5. As we discussed in section 2.4, the dynamics of the mechanical phase gives rise to the synthetic electric field for photons

$$\tilde{\mathcal{E}} = \frac{\mathrm{d}\phi}{\mathrm{d}\tilde{t}} = \tilde{\Delta}_M - \mathcal{P}\frac{|\tilde{a}_1||\tilde{a}_2|}{|\tilde{b}|}\cos\left(\phi - \theta_2 + \theta_1\right), \tag{2.9.9}$$

where θ_j is the phase of the optical mode a_j. Further to equations (2.4.1), (2.4.2) and (2.4.3), equations of motion (2.9.4), (2.9.5) and (2.9.6) take into account the effects of radiation pressure on the mechanical amplitude. This modification of the mechanical amplitude does not qualitatively change the steady state of the model (for a detailed analysis, see appendix 2.F). If light propagates from the lower to the higher optical frequency, a synthetic electric field is generated above a threshold driving power, and, as a consequence, light transport is suppressed. The synthetic electric field vanishes if light propagates from the higher to the lower optical frequency. This leads to unidirectional light transport via the dynamically generated synthetic electric field as discusses in section 2.5.

2.10 Synthetic electric fields in the quantum regime

Now we study the effect of quantum fluctuations both close to the classical limit, $\zeta \to 0$, as well as deep in the quantum regime, $\zeta \gtrsim 1$.

We investigate steady states of the system in the resonant case, i.e., $\Delta_M = \Delta_O = 0$, for which the effects, studied here, are most pronounced. We consider driving the lower optical frequency, where the synthetic electric field is dynamically generated and light transmission is suppressed as discussed in sections 2.4 and 2.5. In the case of driving the higher optical frequency, no synthetic electric field is generated and light can freely propagate to the lower optical frequency (see appendix 2.G for more details).

To understand how the dimensionless parameters introduced in the previous section

influence the dynamics of the quantum model, we rewrite the master equation (2.8.2) in terms of these parameters. The master equation then reads

$$\frac{\mathrm{d}\hat{\rho}}{\mathrm{d}\tilde{t}} = -i\left[\hat{\mathcal{H}},\hat{\rho}\right] + \sum_{j=1}^{2}\mathcal{D}\left[\hat{a}_j\right]\hat{\rho} + \tilde{\gamma}_1\mathcal{D}[\hat{b}^\dagger]\hat{\rho} + \zeta^2\tilde{\gamma}_2\mathcal{D}[\hat{b}^2]\hat{\rho}, \tag{2.10.1}$$

where

$$\hat{\mathcal{H}} = \zeta\left(\hat{b}\hat{a}_2^\dagger\hat{a}_1 + \text{h.c.}\right) + \frac{\sqrt{\mathcal{P}}}{\zeta}(\hat{a}_1 + \hat{a}_1^\dagger). \tag{2.10.2}$$

We can see that the quantum parameter ζ, controls the scaling of optical amplitudes, since the driving strength is $\sqrt{\mathcal{P}}/\zeta$. It also determines the scaling of the mechanical amplitude which is proportional to the ratio of negative damping rate, $\tilde{\gamma}_1$, and the nonlinear damping rate, $\zeta^2\tilde{\gamma}_2$. As we have shown in the previous section, the scaling of optical and mechanical amplitudes does not influence the classical dynamics of the system. The absolute strength of quantum fluctuations, $\left[\hat{b},\hat{b}^\dagger\right] = 1$, does not depend on the scaling of the mechanical amplitude, $\sqrt{\langle\hat{b}^\dagger\hat{b}\rangle} \propto 1/\zeta$. As a result, the relative strength of quantum fluctuations compared to the mechanical amplitude increases with ζ.

Since time is now expressed in the units of photon decay rate κ, the dimensionless parameter $\tilde{\gamma}_1$ represents the ratio of the optical coherence time and the mechanical coherence time. This parameter determines to which extent the mechanical amplitude is influenced by the coupling to the optical modes. We choose $\tilde{\gamma}_1 = 10$, in which case the mechanical dissipative processes are fast compared to the dynamics of optical modes and they dominate the dynamics of the system. In this regime, the modification of the mechanical amplitude due to the coupling to optical modes is marginal. On the other hand, the mechanical phase undergoes a slow dynamics which arise from the coupling to the optical modes since the mechanical dissipative processes are phase insensitive. In this regime, we can study the dynamics of the synthetic gauge field, i.e. the mechanical phase, since the effects originating from the dynamics of the mechanical amplitude are eliminated.

We consider the relative phase, $\varphi = \phi - \theta_2 + \theta_1$, between the mechanical mode of phase ϕ and the optical modes of phases θ_j to study the generation of synthetic electric fields. The relative phase φ determines the action of the radiation pressure force on the

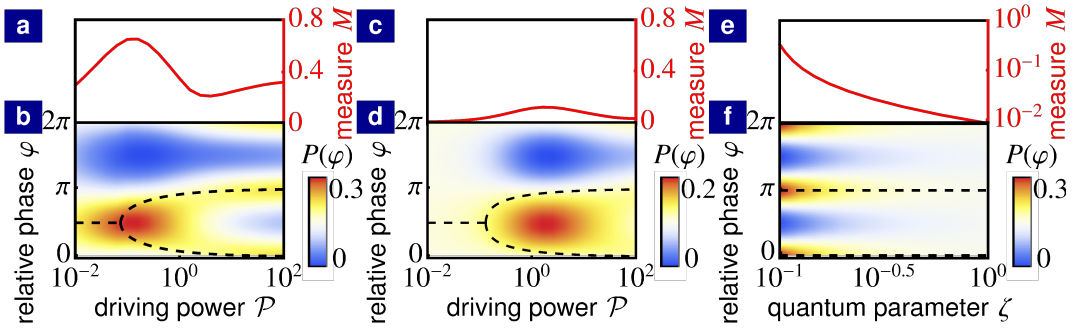

Figure 2.10.1: Relative phase between mechanical and optical modes if the lower optical frequency is driven. Relative phase distribution as a function of driving power $\mathcal{P}$ at the onset of a finite synthetic electric field: (b) close to the classical limit and (d) in the quantum regime. Corresponding phase coherence measure: (a) close to the classical limit and (c) in the quantum regime. Classical-to-quantum crossover: (f) relative phase distribution (shown on a logarithmic scale) and (e) phase coherence measure as a function of the quantum parameter ζ for a large synthetic electric field. The black dashed lines show the classical values of the relative phase. (Master equation simulations for: (a) and (b) $\tilde{\gamma}_1 = 10$, $\tilde{\gamma}_2 = 200$, and $\zeta = 0.1$; (c) and (d) $\tilde{\gamma}_1 = 10$, $\tilde{\gamma}_2 = 40$, and $\zeta = 1$; and (e) and (f) $\tilde{\gamma}_1 = 10$, $\tilde{\gamma}_2 = 200$, and $\mathcal{P} = 10000$.)

mechanical phase and as a consequence also the value of the synthetic electric field as it can be read off from the classical equation (2.9.9). The distribution

$$P(\varphi) = \iiint_0^{2\pi} \mathrm{d}\phi \mathrm{d}\theta_1 \mathrm{d}\theta_2 \, \delta(\phi - \theta_2 + \theta_1 - \varphi) p(\phi, \theta_1, \theta_2) \tag{2.10.3}$$

of the relative phase can be calculated from the steady-state density matrix $\hat{\rho}_{SS}$, where

$$p(\phi, \theta_1, \theta_2) = \mathrm{Tr}\left[|\phi, \theta_1, \theta_2\rangle\langle\phi, \theta_1, \theta_2| \hat{\rho}_{\mathrm{SS}}\right], \tag{2.10.4}$$

$|\phi, \theta_1, \theta_2\rangle = \frac{1}{(2\pi)^{3/2}} \sum_{n,m,l=0}^{\infty} e^{i(n\phi + m\theta_1 + l\theta_2)} |n, m, l\rangle$, $|n\rangle$ is the Fock state. To study the effect of fluctuations on the relative phase φ, we employ

$$M = 2\pi \max\left(P(\varphi)\right) - 1, \tag{2.10.5}$$

as a measure, which was used in Refs. [54, 113]. The quantity M is the height of a peak in the relative phase distribution, $P(\varphi)$. In the following, we will refer to M as the phase coherence measure.

In figure 2.10.1, we show the relative phase distribution and the phase coherence measure as a function of driving power, $\mathcal{P}$, close to the classical limit and deep in the quantum regime. In the classical limit, the relative phase (black dashed lines) has a single value $\varphi = \pi/2$ at small driving power, see figure 2.10.1b, indicating that the synthetic electric field vanishes in steady state (see appendix 2.F). For sufficiently large driving powers, the relative phase bifurcates to values different from $\pi/2$ and a finite synthetic electric field is generated, see section 2.4.

While the classical equations of motion neglect fluctuations in the relative phase, the master equation simulation (see appendix 2.H for more details) takes these fluctuations into account and we study them using the relative phase distribution. Close to the classical limit, the relative phase distribution is peaked around the classical value of the relative phase, see figure 2.10.1b. Fluctuations of the relative phase are reduced in the vicinity of the classical threshold value of driving power. This can be seen from the sharper peak in the relative phase distribution around the classical value (figure 2.10.1b) and the increase of the phase coherence measure at the onset of a finite synthetic electric field, see figure 2.10.1a. In the classical limit, the steady state is bistable above threshold. Depending on the initial conditions, the system ends up in one of the stationary solutions of the classical equations (2.9.4), (2.9.5) and (2.9.6). Fluctuations lead to transitions between these two classically stable stationary solutions and to a unique steady state distribution of the relative phase, which is peaked around the two classical stationary values.

The dynamics deep in the quantum regime shares several features with that in the classical regime, see figure 2.10.1d. At small driving power, the relative phase distribution is peaked around $\varphi = \pi/2$ indicating a vanishing synthetic electric field. For sufficiently large driving powers, the synthetic electric field is generated leading to a bimodal relative phase distribution. The onset of a finite synthetic electric field is shifted to larger driving powers compared to the classical case (black dashed lines). This can be seen both in the relative phase distribution in figure 2.10.1d and the phase coherence measure in figure 2.10.1c. The shifted onset of a finite synthetic electric field is due to a special feature of the quantum van-der-Pol oscillator: the nonlinear (two-phonon) damping cannot dissipate the last remaining phonon [52]. This is not captured by the classical equations of motion. As a result, the mechanical amplitude according to the full quantum model (green solid line) is larger than classically expected,

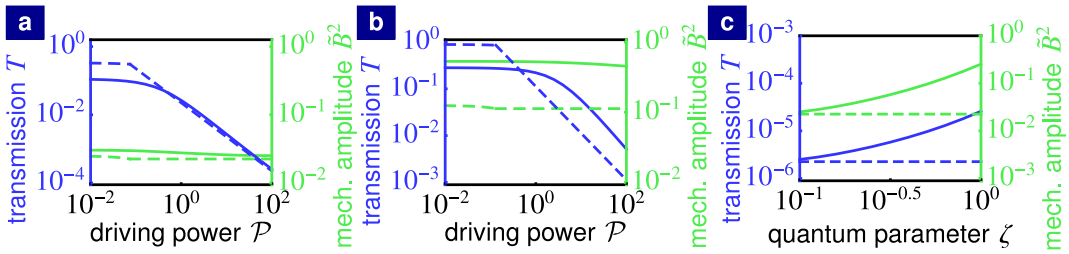

Figure 2.10.2: Light propagation if the lower optical frequency is driven. Optical transmission T and expectation value of the mechanical amplitude $\tilde{B}^2 = \zeta^2\langle\hat{b}^\dagger\hat{b}\rangle$ as a function of driving power $\mathcal{P}$ at the onset of a finite synthetic electric field: (a) close to the classical limit and (b) deep in the quantum regime. (c) Classical-to-quantum crossover: optical transmission and mechanical amplitude as a function of the quantum parameter for large synthetic electric fields. The dashed lines show the classical limit. (Master equation simulations for: (a) $\tilde{\gamma}_1 = 10$, $\tilde{\gamma}_2 = 200$, and $\zeta = 0.1$; (b) $\tilde{\gamma}_1 = 10$, $\tilde{\gamma}_2 = 40$, and $\zeta = 1$; and (c) $\tilde{\gamma}_1 = 10$, $\tilde{\gamma}_2 = 200$, and $\mathcal{P} = 10000$.)

see figure 2.10.2b. Since the mechanical amplitude has to be overcome by the lower-frequency optical amplitude to generate the synthetic electric field (see section 2.5), the onset of a finite synthetic electric field is shifted to larger driving powers.

If a synthetic electric field is generated, it leads to a suppression of light propagation to the higher-frequency optical mode. In figure 2.10.2, the optical transmission T is shown as a function of driving power $\mathcal{P}$. The transmission T is the ratio of the output power leaking from the higher-frequency optical mode, $\kappa\langle\hat{a}_2^\dagger\hat{a}_2\rangle$, to the driving power, $\kappa\mathcal{P}/\zeta^2$. Close to the classical limit, the transmission T is slightly decreased for small driving powers. This is due to fluctuations broadening the mechanical frequency by more than the optical linewidth so that the resonant condition, $\Omega = \nu_2 - \nu_1$, is not satisfied for every scattering event (absorption of a phonon). For large driving powers, the generated synthetic electric field significantly suppresses the transmission T by many orders of magnitude. A similar dependence of the transmission T on driving power is found in the quantum regime, see figure 2.10.2b. For small driving powers, the transmission is marginally reduced by fluctuations. For sufficiently large driving powers, the transmission is strongly suppressed by the dynamically generated synthetic electric field. However, the same amount of suppression occurs for larger driving powers than in the classical limit since the onset of a finite synthetic electric field is shifted due to larger mechanical amplitude $\tilde{B}^2$.

2.11 Classical-to-quantum crossover

To shed more light on the influence of quantum fluctuations and the quantization of energy levels, we study transmission across the classical-to-quantum crossover.

We consider driving powers well above the onset of a finite synthetic electric field. The synthetic electric field then remains constant as the quantum regime is approached for increasing ζ. As a result, the relative phase distribution $P(\varphi)$ is always peaked around its classical value, see figure 2.10.1f. On the other hand, as the quantum regime is reached, the relative phase distribution is washed out by quantum fluctuations. As a consequence, the phase coherence measure significantly decreases, as seen in figure 2.10.1e.

This demonstrates the robustness of the synthetic electric field generation against noise. According to the classical equations of motion, the synthetic electric field, $\tilde{\mathcal{E}} \propto -\cos(\varphi)$, depends on the relative phase, φ, see (2.9.9). The relative phase distribution is washed out by quantum fluctuations as the quantum regime is approached. However, the dynamics of the mechanical phase still results in the generation of the synthetic electric field. It causes a shift in the frequency of the nondriven optical mode, which can be seen in the power spectrum of this mode (shown in appendix 2.I). As a result, the dynamically generated synthetic electric field detunes the phonon-assisted photon tunneling from resonance leading to a suppression of light transmission even in the quantum regime (see figure 2.10.2c). This shows that while the values of the optical and mechanical phases are sensitive to noise, the synthetic electric field, represented by the time evolution of the mechanical phase, is robust.

Even though the generation of synthetic electric fields is not prevented by quantum fluctuations, transmission (solid blue line) increases as the quantum regime is approached, see figure 2.10.2c. However this increase can be explained by the larger mechanical amplitude according to the full quantum model (green solid line) than classically expected (green dashed line). For sufficiently large driving powers, the transmission, $T \approx 4\tilde{B}^2/\tilde{\mathcal{E}}^2$, depends linearly on the mechanical amplitude, $\tilde{B}^2$ (see appendix 2.F for the full analytical expression).

The generation of synthetic electric fields and the suppression of light propagation in the direction of higher optical frequencies is robust against noise. They are also present deep in the quantum regime where quantum fluctuations wash out the relative

phase, φ, which is sensitive to noise. However, transmission in the blockaded direction is increased due to a larger mechanical amplitude, which is increased in the quantum regime compared to the classical limit.

2.12 Conclusions

While synthetic gauge fields for photons have been investigated thoroughly in recent years, little was known about their dynamics. In this work, we have uncovered how a synthetic electric field can be spontaneously created in a readily realizable optomechanical setup. The resulting nonlinear photon-diode type of unidirectional transport can lead to a large isolation ratio, especially in arrays. We demonstrate how the interplay of nonlinearity, dynamics, and artificial gauge fields can produce novel physical effects and possible new devices.

In the second step, we have investigated synthetic dynamical gauge fields in the quantum regime, where quantum fluctuations have to be taken into account. We have shown that even though the mechanical phase is very sensitive to noise and its steady-state value is washed out by quantum fluctuations, its nonlinear dynamics still results in the generation of synthetic electric fields. As a result, unidirectional light transport via synthetic dynamical gauge fields is robust against noise and it leads, also in the quantum regime, to significant isolation ratios. They are, however, reduced compared to the classical regime due to an increased mechanical amplitude. Our work paves the way for studying both the classical and the quantum dynamics of synthetic gauge fields in optomechanics.

Appendices

2.A Phonon-assisted photon tunneling

In this section, we derive the Hamiltonian (2.2.1) that describes our scenario in the main text including the photon-phonon interaction term $\hat{b}\hat{a}_2^\dagger\hat{a}_1$. This term is obtained in optomechanical systems with two (or more) optical modes. Qualitatively, this term arises whenever there are two optical modes that couple to the same mechanical resonator, and the term becomes important dynamically if the mechanical frequency matches the optical frequency difference. The earliest, well-known example is the membrane-in-the-middle setup of the Harris group [108, 109]. More generally, such a three-body interaction term will arise in systems of nonlinearly coupled modes (e.g. between three optical modes in a $\chi^{(2)}$-medium, or between microwave modes in the presence of a Josephson nonlinearity).

We consider a membrane in a cavity whose vibrational mode $\hat{b}$ couples to two optical modes of the cavity. The position of the membrane determines the frequencies ω_L and ω_R of the optical modes $\hat{a}_L$ (to the left of the membrane) and $\hat{a}_R$ (to the right of the membrane), respectively. Placing the membrane exactly in the middle of the cavity results in equal optical frequencies. Dislocating the membrane slightly from the center introduces splitting $\omega = \omega_R - \omega_L$ between the optical frequencies. Without loss of generality, we assume $\omega \geq 0$. The optical modes $\hat{a}_{L/R}$ coupled to the mechanical mode $\hat{b}$ are described by the Hamiltonian

$$\begin{aligned}\hat{H} =&\omega_L\hat{a}_L^\dagger\hat{a}_L + \omega_R\hat{a}_R^\dagger\hat{a}_R + \Omega\,\hat{b}^\dagger\hat{b} + J_0\left(\hat{a}_L^\dagger\hat{a}_R + \text{h.c.}\right)\\ &- g_0\left(\hat{a}_L^\dagger\hat{a}_L - \hat{a}_R^\dagger\hat{a}_R\right)\left(\hat{b}^\dagger + \hat{b}\right),\end{aligned} \tag{2.A.1}$$

where Ω is the mechanical frequency, g_0 is the single-photon optomechanical coupling strength and J_0 is the optical coupling strength. For optical modes with a different transversal spatial profile, J_0 can be arbitrarily tuned by the tilt of the membrane

[109]. Due to the optical coupling, the cavity modes hybridize and that gives rise to supermodes

$$\hat{a}_1 = \frac{-J_0\,\hat{a}_L + \lambda\,\hat{a}_R}{\sqrt{J_0^2+\lambda^2}}, \tag{2.A.2}$$

$$\hat{a}_2 = \frac{\lambda\,\hat{a}_L + J_0\,\hat{a}_R}{\sqrt{J_0^2+\lambda^2}}, \tag{2.A.3}$$

at frequencies $\nu_1 = \omega_L - \lambda$ and $\nu_2 = \omega_R + \lambda$, where $\lambda = \sqrt{\frac{\omega^2}{4} + J_0^2} - \frac{\omega}{2}$. In terms of the supermodes, the Hamiltonian reads

$$\begin{aligned}\hat{H} = &\sum_{j=1}^{2} \nu_j \hat{a}_j^\dagger \hat{a}_j + \Omega\,\hat{b}^\dagger\hat{b} \\ &+ \left[J_{\rm res}\left(\hat{a}_2^\dagger\hat{a}_2 - \hat{a}_1^\dagger\hat{a}_1\right) + J\left(\hat{a}_1^\dagger\hat{a}_2 + h.c.\right)\right]\left(\hat{b}^\dagger + \hat{b}\right),\end{aligned} \tag{2.A.4}$$

where

$$J = \frac{g_0}{\sqrt{1+\frac{\omega^2}{4J_0^2}}}, \tag{2.A.5}$$

$$J_{\rm res} = \frac{g_0}{\sqrt{1+\frac{4J_0^2}{\omega^2}}}. \tag{2.A.6}$$

Next, we assume driving of $\hat{a}_{L/R}$ with lasers of strengths $E_{L/R}$ at frequencies $\nu_{D,L/R}$. Neglecting quantum fluctuations around large optical amplitudes, we can derive equations of motion

$$\dot{\phi} = \Delta_M + \frac{J_{\mathrm{res}}}{B}\left(|a_1|^2 - |a_2|^2\right)\cos\left[\phi - \delta t\right] - \frac{J}{B}\mathrm{Re}\left[a_1^* a_2 e^{-i\phi} + a_1 a_2^* e^{-i\phi+2i\delta t}\right], \quad (2.A.7)$$

$$\dot{a}_1 = i\Delta_1 a_1 - iE_1 - iE_1^{\mathrm{res}} e^{-i\delta t} + iB\left[J_{\mathrm{res}} a_1\left(e^{-i\phi+i\delta t} + e^{i\phi-i\delta t}\right) - Ja_2\left(e^{-i\phi} + e^{i\phi-i2\delta t}\right)\right] - \frac{\kappa}{2}a_1, \quad (2.A.8)$$

$$\dot{a}_2 = i\Delta_2 a_2 - iE_2 + iE_2^{\mathrm{res}} e^{i\delta t} - iB\left[J_{\mathrm{res}} a_2\left(e^{-i\phi+i\delta t} + e^{i\phi-i\delta t}\right) + Ja_1\left(e^{i\phi} + e^{-i\phi+2i\delta t}\right)\right] - \frac{\kappa}{2}a_2, \quad (2.A.9)$$

in frames rotating at suitable frequencies (mode a_1 at $\nu_{D,L}$, mode a_2 at $\nu_{D,R}$ and mode b at $\delta = \nu_{D,R} - \nu_{D,L}$), where we assume mechanical limit-cycle oscillations $\langle\hat{b}\rangle = Be^{i\phi}$ with a fixed amplitude B. We define $\Delta_1 = \nu_{D,L} - \nu_1$, $\Delta_2 = \nu_{D,R} - \nu_2$, $\Delta_M = \delta - \Omega$, $E_1 = E_L/\sqrt{1+\lambda^2/J_0^2}$, $E_1^{\mathrm{res}} = E_R/\sqrt{1+J_0^2/\lambda^2}$, $E_2 = E_R/\sqrt{1+\lambda^2/J_0^2}$ and $E_2^{\mathrm{res}} = E_L/\sqrt{1+J_0^2/\lambda^2}$.

Now we consider the resonant case, $\Delta_1 = \Delta_2 = 0$, when the generation of the synthetic electric fields is the most pronounced. In this case, driving of $\hat{a}_L$ mostly addresses supermode $\hat{a}_1$, since the laser is on resonance with its frequency and the overlap of $\hat{a}_L$ with the other supermode $\hat{a}_2$ is small provided that $\omega \gg J_0$. As a result, we can neglect the residual driving of the supermode $\hat{a}_2$. Similarly, driving of $\hat{a}_R$ leads to addressing mostly the supermode $\hat{a}_2$. If the residual drivings are negligible and we tune the mechanical frequency such that $\Omega = \nu_2 - \nu_1$, the coupling term $\hat{b}\hat{a}_2^\dagger\hat{a}_1$ is selected and the other coupling terms in the Hamiltonian (2.A.4) are off resonance. Neglecting the off-resonant coupling terms within the rotating-wave approximation, which is valid for $\Omega = \nu_2 - \nu_1 \approx \omega \gg \kappa, g_0, g_0 B$, the equations of motion reduce to equations (2.4.1), (2.4.2) and (2.4.3) considered in the main text with the effective tunneling amplitude J given by equation (2.A.5). The tunneling amplitude J decreases with decreasing J_0. As a result, a fine tuning of the ratio ω/J_0 is necessary to achieve the optimal trade-off between eliminating the residual driving of unwanted supermodes and maximizing the amplitude of the term $\hat{b}\hat{a}_2^\dagger\hat{a}_1$.

We have derived the Hamiltonian (2.2.1) for optical supermodes, which is considered as the starting point in the main text, from the fundamental optomechanical Hamiltonian (2.A.1) for two optical modes coupled to a single mechanical mode. In summary, whenever two optical modes and one mechanical resonator are in a mutual interaction,

and when the mechanical frequency matches the optical frequency difference (at least approximately), the interaction term $\hat{a}_2^\dagger \hat{a}_1 \hat{b} + \text{h.c.}$ assumed in our work is the generic outcome.

2.B Steady states of the two-site system

In this section, we analyze the steady states of the two-site system with single mode being driven. They are stationary solutions of the equations of motion (equations (2.4.1), (2.4.2) and (2.4.3) in the main text) constant in time. We first apply a time-dependent gauge transformation to express the time-evolution of the mechanical phase in a form of an effective optical frequency shift. Then we find a stationary condition for the synthetic electric field $\mathcal{E}$. Finally, we use an effective potential for the synthetic electric field to study stability of its stationary solutions.

As mentioned in the main text, we assume that only one mode is driven. We label the driven mode by the index $k = 1, 2$. Driving strengths can then be expressed as $E_j = E\,\delta_{j,k}$ for $j = 1, 2$, where $\delta_{j,k}$ is the Kronecker delta. The detuning of the nondriven mode can be set to zero, since there is no driving frequency. Therefore, the optical detunings can be expressed as $\Delta_j = \Delta_\mathrm{O}\,\delta_{j,k}$. We make use of the time-dependent gauge transformation

$$\phi = \tilde{\phi} + \chi, \tag{2.B.1}$$

$$a_1 = \tilde{a}_1 e^{-i\chi\,\delta_{2,k}}, \tag{2.B.2}$$

$$a_2 = \tilde{a}_2 e^{i\chi\,\delta_{1,k}}, \tag{2.B.3}$$

which moves the dynamics of the mechanical phase to the time-dependent gauge parameter χ. By appropriately choosing χ, we can always achieve $\tilde{\phi} = 0$. The time-dependent gauge transformation leaves the absolute values of the optical amplitudes unchanged. As a result, a particular value of the gauge parameter is irrelevant. Only its first derivative $\dot{\chi} = \dot{\phi}$ influences the optical occupations. The time evolution of the mechanical phase results in an effective shift $(\delta_{2,k} - \delta_{1,k})\,\dot{\chi}$ of the nondriven optical mode's frequency. Note that the driven mode, a_k, is forced to oscillate with the frequency of the laser drive, and thus it does not experience any frequency shift.

The role of the optical frequency shift $\dot{\chi}$ can be understood in analogy to electromag-

netism. The mechanical phase corresponds to an effective vector potential. According to conventional electromagnetism, the time evolution of the vector potential generates an electric field. This electric field can be also represented by a scalar potential gradient. In this analogy, the time evolution of the mechanical phase generates a synthetic electric field $\mathcal{E} = \dot{\chi}$ for photons, which represent an effective optical frequency shift.

To provide the fixed point analysis for the both cases $k = 1, 2$ at once, we use general indexes $(k, l) \in \{(1, 2), (2, 1)\}$ to label the optical modes. According to the gauge transformation (2.B.1), (2.F.2), and (2.F.3), the equations of motion transform to

$$\dot{\tilde{\phi}} = \mathcal{E} - \Delta_{\mathrm{M}} + \frac{J}{B} \operatorname{Re}\left[\tilde{a}_k^* \tilde{a}_l\right] = 0, \tag{2.B.4}$$

$$\dot{\tilde{a}}_k = i\Delta_{\mathrm{O}} \tilde{a}_k - iE - iJB\tilde{a}_l - \frac{\kappa}{2}\tilde{a}_k, \tag{2.B.5}$$

$$\dot{\tilde{a}}_l = i\left(\delta_{2,k} - \delta_{1,k}\right)\mathcal{E}\tilde{a}_l - iJB\tilde{a}_k - \frac{\kappa}{2}\tilde{a}_l, \tag{2.B.6}$$

where we substituted $\mathcal{E} = \dot{\chi}$. Taking the time derivative of equation (2.B.4), we obtain the equation of motion for the synthetic electric field

$$\begin{aligned}\dot{\mathcal{E}} = &-\kappa\left(\mathcal{E} - \Delta_{\mathrm{M}}\right) + \frac{EJ}{B} \operatorname{Im}\left[\tilde{a}_l\right] \\ &+ \frac{J}{B}\left(\left(\delta_{2,k} - \delta_{1,k}\right)\mathcal{E} - \Delta_{\mathrm{O}}\right) \operatorname{Im}\left[\tilde{a}_k^* \tilde{a}_l\right].\end{aligned} \tag{2.B.7}$$

To find stationary solutions of the equations of motion (2.B.5), (2.B.6), and (2.B.7), we first use that the equations (2.B.5) and (2.B.6) are linear in terms of optical amplitudes. For a given value of the synthetic electric field $\mathcal{E}$, the stationary optical amplitudes read

$$\tilde{a}_k = E\frac{\left(\delta_{2,k} - \delta_{1,k}\right)\mathcal{E} + i\frac{\kappa}{2}}{-J^2B^2 + \left(\delta_{2,k} - \delta_{1,k}\right)\mathcal{E}\Delta_{\mathrm{O}} - \left(\frac{\kappa}{2}\right)^2 + i\frac{\kappa}{2}\left[\left(\delta_{2,k} - \delta_{1,k}\right)\mathcal{E} + \Delta_{\mathrm{O}}\right]}, \tag{2.B.8}$$

$$\tilde{a}_l = \frac{JB}{\left(\delta_{2,k} - \delta_{1,k}\right)\mathcal{E} + i\frac{\kappa}{2}}\tilde{a}_k. \tag{2.B.9}$$

In following, we set $\Delta_{\mathrm{O}} = \Delta_{\mathrm{M}} = 0$ to present the important features of the steady states. These features are not changed by finite detunings. We discuss the effects of

finite detunings at the end of this section. By substituting the stationary values of the optical amplitudes (2.B.8), (2.B.9) into equation (2.B.7), we obtain the stationary condition for the synthetic electric field

$$\dot{\mathcal{E}} = -\kappa\mathcal{E}\,\frac{\left(\frac{\mathcal{E}}{\kappa}\right)^2 + 4\left[\left(\frac{JB}{\kappa}\right)^2 + \frac{1}{4}\right]^2 + 4\left(\delta_{2,k} - \delta_{1,k}\right)\left(\frac{EJ}{\kappa^2}\right)^2}{\left(\frac{\mathcal{E}}{\kappa}\right)^2 + 4\left[\left(\frac{JB}{\kappa}\right)^2 + \frac{1}{4}\right]^2} \tag{2.B.10}$$

$$= 0 \tag{2.B.11}$$

For $k = 2$, when the mode with the higher optical frequency, a_2, is driven, only the single stationary solution, $\mathcal{E} = 0$, exists. For $k = 1$, when the mode with the lower optical frequency, a_1, is driven, stationary solutions with a finite synthetic electric field

$$\mathcal{E}_\pm = \pm 2\kappa\sqrt{\left(\frac{EJ}{\kappa^2}\right)^2 - \left[\left(\frac{JB}{\kappa}\right)^2 + \frac{1}{4}\right]^2} \tag{2.B.12}$$

emerge for $4EJ/\kappa^2 > 4\left(BJ/\kappa\right)^2 + 1$ in addition to $\mathcal{E} = 0$.

To gain intuition about the stability of these stationary solutions, we find the potential

$$\begin{aligned} V(\mathcal{E}) =& \frac{\kappa^3}{2}\left(\frac{\mathcal{E}}{\kappa}\right)^2 + 2\kappa^3\left(\delta_{2,k} - \delta_{1,k}\right)\left(\frac{JE}{\kappa^2}\right)^2 \\ & \times \ln\left(\left(\frac{\mathcal{E}}{\kappa}\right)^2 + 4\left[\left(\frac{JB}{\kappa}\right)^2 + \frac{1}{4}\right]^2\right). \end{aligned} \tag{2.B.13}$$

such that $-\mathrm{d}V(\mathcal{E})/\mathrm{d}\mathcal{E}$ is equal to the right hand side of equation (2.B.10). The potential shows that the stationary solution $\mathcal{E} = 0$ is always a stable steady state for $k = 2$ when the optical mode with the higher optical frequency is driven (see figure 2.B.1). The stability of the steady state does not depend on the system parameters. For $k = 1$, when the mode with the lower optical frequency is driven, the stability of the steady state depends on the two dimensionless parameters EJ/κ^2 and BJ/κ. The potential in figure 2.B.1 shows that the steady state $\mathcal{E} = 0$ is the only stationary solution and it

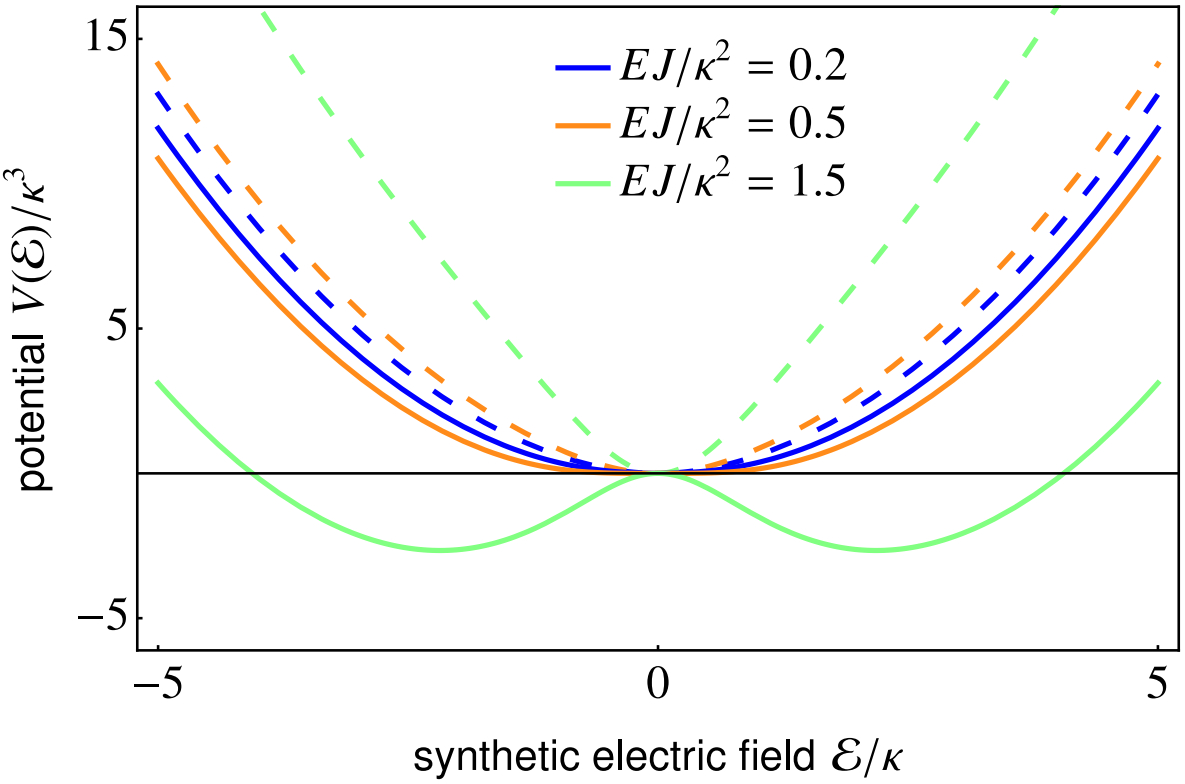

Figure 2.B.1: The potential for the synthetic electric field. It has a single minimum at $\mathcal{E} = 0$ for $k = 2$ (dashed lines) when the higher optical frequency is driven. For $k = 1$, when the lower optical frequency is driven, the stationary value $\mathcal{E} = 0$ becomes unstable with increasing EJ/κ^2 as two minima with a finite frequency shift emerge (solid lines). (The potential is plotted for $BJ/\kappa = 0.5$.)

is stable in the white region of the phase diagram depicted in figure 2.3.1 of the main text. It becomes unstable as the two steady states with a finite synthetic electric field emerge in the colored region of the phase diagram in figure 2.3.1 of the main text. Note that the potential does not provide conclusive information about the stability of the steady states because it does not take into account the dynamics of the optical modes. Therefore, the linear stability analysis was used to confirm that the stability of the steady states is determined correctly by the potential $V(\mathcal{E})$.

A finite mechanical detuning, $\Delta_{\mathrm{M}} \neq 0$, detunes the phonon-assisted photon tunneling process from resonance. In this way, the mechanical detuning represents a static synthetic electric field for photons in contrast to the dynamically generated synthetic electric field $\mathcal{E}$. If the higher optical frequency is driven, the dynamically generated

synthetic electric field $\mathcal{E}$ acts against this static synthetic electric field and increases transmission to the lower optical frequency with the increasing laser amplitude. On the other hand, for the lower optical frequency being driven, the dynamically generated synthetic electric field detunes the tunneling process further from resonance with the increasing laser amplitude. As a result, it decreases light propagation to the nondriven optical mode. Above some threshold of the laser amplitude, the synthetic electric field bifurcates as the effective potential have two local minima. This again happens only for the lower frequency being driven.

A finite laser detuning, $\Delta_{\mathrm{O}} \neq 0$, suppresses the coherent driving, which results in a smaller optical amplitude of the driven mode. For the higher optical frequency being driven, the synthetic electric field always vanishes even for a finite optical detuning. It vanishes also when the lower optical frequency is driven for small laser amplitudes. Similarly as in the resonant case, the synthetic electric field bifurcates to finite values over the threshold of the laser amplitude for the lower frequency being driven. The threshold and the values of the bifurcated synthetic electric field are modified by the finite optical detuning since it changes the population and the phase of the driven optical mode. However, the qualitative features of the synthetic electric field remain the same. The synthetic electric field is generated only above threshold and only for the lower optical frequency being driven.

2.C Numerical simulations of the full equations of motion

In this section, we present numerical simulations of the system described by the fundamental Hamiltonian (2.A.1) when we consider the laser drive coupling to the original (uncoupled) cavity modes, out of which the supermodes are formed. In this way, we demonstrate the validity of the results presented in the main text where the description of the system is simplified by assuming that individual supermodes can be separately coupled to the laser drive.

We now simulate the dynamics of the uncoupled optical modes $\hat{a}_L$ and $\hat{a}_R$ according to the fundamental Hamiltonian (2.A.1). To this end, we derive classical equations of motion

$$\dot{\phi} = -\Omega + \frac{g_0}{B}\left(|a_L|^2 - |a_R|^2\right)\cos\phi, \tag{2.C.1}$$

$$\dot{a}_L = i\left(\Delta_L + 2g_0 B\cos\phi\right)a_L - iE_L - iJ_0 a_R - \frac{\kappa}{2}a_L, \tag{2.C.2}$$

$$\dot{a}_R = i\left(\Delta_R - 2g_0 B\cos\phi\right)a_R - iE_R - iJ_0 a_L - \frac{\kappa}{2}a_R, \tag{2.C.3}$$

neglecting quantum fluctuations around the expectation values $a_{L/R} = \langle \hat{a}_{L/R}\rangle$, where we again assume that the mechanical mode, $\langle \hat{b}\rangle = Be^{i\phi}$, performs limit-cycle oscillation with a fixed amplitude B as well as $\Delta_L = \nu_D - \omega_L$, $\Delta_R = \nu_D - \omega_R$, and ν_D is the frequency of the laser drive. We consider driving of a single uncoupled optical mode at resonance with the corresponding supermode, i.e. $\nu_D = \nu_1$ for $E_L \neq 0$ or $\nu_D = \nu_2$ for $E_R \neq 0$, and $\Omega = \nu_2 - \nu_1$. The generated synthetic electric field and the optical transmission are shown in figure 2.C.1 as a function of the rescaled driving strength Eg_0/κ^2. One can see in figure 2.C.1a that a large synthetic electric field is generated for mode a_L being driven (solid lines). As a result, the transmission to the right (solid lines) is significantly suppressed, see figure 2.C.1b.

For driving mode a_R, a small synthetic electric field (dashed lines) is generated. This is in contrast to the simplified model in the main text, where the synthetic electric field completely vanishes when light propagates to the lower optical frequency. The small generated synthetic electric field is a result of the residual driving of the supermode a_1 due to its nonvanishing overlap with the driven uncoupled mode a_R. Since the mechanical frequency, $\Omega = \nu_2 - \nu_1$, is chosen to match the optical frequency difference, the supermode a_1 is driven on the blue sideband. However, the residual driving can be suppressed by increasing the sideband ratio ω/κ, see figure 2.C.1a. As a result, a significant suppression of the optical transmission to the right (solid lines) in comparison to the transmission to the left (dashed lines) can be reached, see figure 2.C.1b. This leads to unidirectional transport of light which works especially well in one-dimensional arrays. In such an array, the transmission ratio is exponentiated by the length of the array, which results in a large suppression of transport in one direction.

Simulating the dynamics of the uncoupled optical modes, we have shown that unidirectional light transport via synthetic electric fields is achieved for the fundamental model described by the Hamiltonian (2.A.1). This demonstrates that the model in

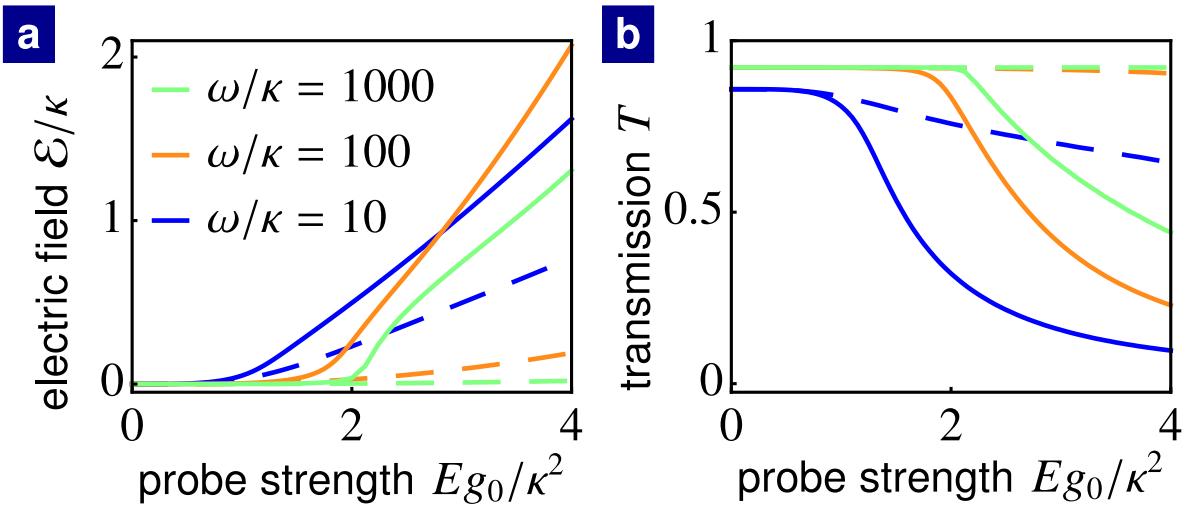

Figure 2.C.1: Dynamically generated synthetic electric fields in the two site system considering the model described by the fundamental Hamiltonian (2.A.1). (a) For the uncoupled optical mode, a_L, being driven with a laser at frequency ν_1 (solid lines), a large synthetic electric field $\mathcal{E}$ develops. For driving the uncoupled optical mode, a_R, with a laser at frequency ν_2 (dashed lines), a small synthetic electric field develops, however, it is reduced as the sideband ratio ω/κ increases (see the legend). (b) As a result, the optical transmission T to the right (solid lines) is significantly suppressed in comparison to the transmission to the left (dashed lines). In a one-dimensional array, this transmission ratio gets exponentiated by the length of the array, leading to a very significant suppression of transport in one direction. (Plotted for $Bg_0/\kappa = 2$, $J_0/\omega = 0.085$.)

the main text indeed captures the important features of the interaction between the two optical modes and the mechanical mode in our scenario. Our results show that unidirectional light transport is more pronounced with the increasing sideband ratio ω/κ.

2.D Phase locking

In this section, we provide a brief summary of phase locking, which can be reached in the two site system by simultaneously driving both optical modes. Note that the analysis presented in the main text is for a single mode driven only. We present here quantitative features of phase locking, which has been previously well studied in a similar optomechanical system [77].

The starting point of the analysis are the equations of motion (2.4.1), (2.4.2) and (2.4.3) in the main text. The stationary values for the optical amplitudes are

$$a_1 = -\frac{JBE_2 e^{-i\phi} + i\frac{\kappa}{2}E_1}{J^2B^2 + \left(\frac{\kappa}{2}\right)^2}, \tag{2.D.1}$$

$$a_2 = -\frac{JBE_1 e^{i\phi} + i\frac{\kappa}{2}E_2}{J^2B^2 + \left(\frac{\kappa}{2}\right)^2}. \tag{2.D.2}$$

Note that if both optical modes are driven, the phases φ_1 and φ_2 of the laser amplitudes E_1 and E_2, respectively, determine the phases θ_1 and θ_2 of the intracavity modes. This is different to the case when only a single optical mode is driven, where the phase of the driving amplitude is irrelevant.

The stationary value of the mechanical phase ϕ obeys the Adler equation

$$\Delta_M - |a_1||a_2|\cos(\phi - \theta) = 0. \tag{2.D.3}$$

where $\theta = \theta_2 - \theta_1$. However, the absolute values of the optical amplitudes $|a_1|$ and $|a_2|$ depend on the phase difference $\phi - \theta$. The Adler equation still determines uniquely the stationary value of $\cos(\phi - \theta)$ but the full analytical expression of this equation is complicated. Thus it is simpler to switch to the phase difference $\varphi = \varphi_2 - \varphi_1$ of the laser phases φ_1 and φ_2. The Adler equation then has the form

$$\Delta_M - \frac{J}{B}\frac{|E_1||E_2|}{J^2B^2 + \left(\frac{\kappa}{2}\right)^2}\cos(\phi - \varphi) = 0. \tag{2.D.4}$$

We can easily read off that the stationary solution of ϕ exists for

$$|\Delta_M| \leq \frac{J}{B}\frac{|E_1||E_2|}{J^2B^2 + \left(\frac{\kappa}{2}\right)^2}. \tag{2.D.5}$$

The mechanical phase ϕ is locked under this condition to the difference φ of the laser drives' phases. Since there is one-to-one correspondence between the laser drives' phases and the intracavity modes' phases, the mechanical phase ϕ can be equivalently though to be locked to the phase difference θ of the intracavity modes.

2.E One-dimensional arrays

Here we provide details about one-dimensional arrays analyzed in the main text. We consider an array, depicted in figure 2.2.1c of the main text, represented by a stack of membranes inside a cavity. The sites of the array support optical modes a_j whose frequencies ν_j increase with site index $j = 1, .., n$. We assume that the phonon-assisted photon tunneling processes are resonant: $\Omega_j = \nu_{j+1} - \nu_j$, where Ω_j is the frequency of the mechanical oscillator assisting tunneling between modes $\hat{a}_j$ and $\hat{a}_{j+1}$. Specifically, we will consider a situation where some optical mode $j = d$ is driven resonantly from the side, to study light propagation towards the left ($j < d$), and towards the right ($j > d$). Alternatively to membrane stacks, suitably designed coupled cavity arrays in optomechanical crystals could implement such a setup.

The mechanical oscillators are again assumed to perform limit cycle oscillations $\langle \hat{b}_j \rangle = B\, e^{i\phi_j}$ with free phases and with a fixed amplitude B equal for all mechanical oscillators. By straightforward extension of equations (2.4.1), (2.4.2), and (2.4.3) (in the main text), we obtain the coupled equations of motion for the optical amplitudes and the mechanical phases

$$\dot{\phi}_j = -\frac{J}{B} \mathrm{Re}\left[a_j^* a_{j+1} e^{-i\phi_j}\right], \tag{2.E.1}$$

$$\dot{a}_j = -iE_j\delta_{j,d} - iJBe^{-i\phi_j}a_{j+1} - iJBe^{i\phi_{j-1}}a_{j-1} - \frac{\kappa}{2}a_j, \tag{2.E.2}$$

where $\delta_{j,d}$ is the Kronecker delta. The optical modes are expressed in the frames rotating with their frequencies ν_j and the mechanical modes are in the frames rotating with the difference of optical frequencies on the neighboring sites: $\nu_{j+1} - \nu_j$.

We study the dynamics of one-dimensional arrays by numerically solving the classical equations of motion (2.E.1) and (2.E.2). The system converges to a steady state for any values of the parameters EJ/κ^2 and BJ/κ. Properties of the steady states are discussed in the main text.

2.F Steady states of the setup with the classical van-der-Pol oscillator

In this section, we study the steady state in the classical limit, $\zeta \to 0$, of the two optical modes coupled by phonon-assisted tunneling where the phonon mode is described by the van-der-Pol oscillator. To this end, we find the stationary solutions of the classical equations of motion (2.9.4), (2.9.5), and (2.9.6). We proceed in the same way as in appendix 2.B. First, we use a time-dependent gauge transformation to represent the time evolution of the mechanical phase in a form of the effective optical frequency shift, which corresponds to the synthetic electric field. Then, we use linearity of the equations of motion for the optical modes to find their stationary values. Finally, by substituting in the stationary optical amplitudes, we obtain the stationary values of the mechanical amplitude and the effective optical frequency shift.

The evolution of the mechanical phase and the mechanical amplitude can be separated by the time-dependent gauge transformation

$$\tilde{b} \to \tilde{b}e^{i\chi}, \tag{2.F.1}$$

$$\tilde{a}_1 \to \tilde{a}_1 e^{-i\chi\,\delta_{2,k}}, \tag{2.F.2}$$

$$\tilde{a}_2 \to \tilde{a}_2 e^{i\chi\,\delta_{1,k}}, \tag{2.F.3}$$

where $\chi = \chi(t)$ is a time-dependent gauge choice. We set $\chi = -\phi$ to express the time evolution of the mechanical phase in the form of an effective optical frequency shift, $\tilde{\mathcal{E}} = \mathrm{d}\chi/\mathrm{d}\tilde{t}$, which represents the synthetic electric field. Here, ϕ is the phase of the mechanical mode $\tilde{b} = \tilde{B}e^{i\phi}$. After the time-dependent gauge transformation, the mechanical phase is set to zero. Under the time-dependent gauge transformation

(2.F.1), (2.F.2) and (2.F.3), the equations of motion transform to

$$\frac{\mathrm{d}\tilde{B}}{\mathrm{d}\tilde{t}} = (\delta_{1,k} - \delta_{2,k})\,\mathcal{P}\,\mathrm{Im}\left[\tilde{a}_k^* \tilde{a}_l\right] + \frac{\tilde{\gamma}_1}{2}\tilde{B} - \tilde{\gamma}_2 \tilde{B}^3, \tag{2.F.4}$$

$$\begin{aligned}\frac{\mathrm{d}\tilde{\mathcal{E}}}{\mathrm{d}\tilde{t}} =& \left(\tilde{\Delta}_M - \tilde{\mathcal{E}}\right)\left(1 + \frac{\tilde{\gamma}_1}{2} - \tilde{\gamma}_2 \tilde{B}^2\right) + \frac{\mathcal{P}}{\tilde{B}}\,\mathrm{Im}\left[\tilde{a}_l\right] \\ &- \left[(\delta_{2,k} - \delta_{1,k})\left(\tilde{\Delta}_M - 2\tilde{\mathcal{E}}\right) + \tilde{\Delta}_O\right]\frac{\mathcal{P}}{\tilde{B}}\,\mathrm{Im}\left[\tilde{a}_k^* \tilde{a}_l\right],\end{aligned} \tag{2.F.5}$$

$$\frac{\tilde{a}_k}{\mathrm{d}\tilde{t}} = i\tilde{\Delta}_{\mathrm{O}}\tilde{a}_k - i - i\tilde{B}\tilde{a}_l - \frac{1}{2}\tilde{a}_k, \tag{2.F.6}$$

$$\frac{\tilde{a}_l}{\mathrm{d}\tilde{t}} = i\,(\delta_{2,k} - \delta_{1,k})\,\tilde{\mathcal{E}}\tilde{a}_l - i\tilde{B}\tilde{a}_k - \frac{1}{2}\tilde{a}_l. \tag{2.F.7}$$

We study the stationary solutions of the equations of motion for $\Delta_O = \Delta_M = 0$. Finite optical and mechanical detunings do not qualitatively change the steady states of the system, see appendix 2.B. The optical amplitudes' stationary values for a given mechanical amplitude and a given synthetic electric field, read

$$\tilde{a}_k = \frac{(\delta_{2,k} - \delta_{1,k})\,\tilde{\mathcal{E}} + i\frac{1}{2}}{-\tilde{B}^2 - \frac{1}{4} + i\frac{1}{2}(\delta_{2,k} - \delta_{1,k})\,\tilde{\mathcal{E}}}, \tag{2.F.8}$$

$$\tilde{a}_l = \frac{\tilde{B}}{-\tilde{B}^2 - \frac{1}{4} + i\frac{1}{2}(\delta_{2,k} - \delta_{1,k})\,\tilde{\mathcal{E}}}. \tag{2.F.9}$$

When the mode with the higher optical frequency, a_2, is driven, the system converges to a unique steady state with vanishing synthetic electric field $\tilde{\mathcal{E}}$ for all parameters. The stationary condition for the mechanical amplitude $\tilde{B}$ reads

$$(\delta_{2,k} - \delta_{1,k})\,\frac{\mathcal{P}}{2} + \frac{\tilde{\gamma}_1}{32} + \left(\frac{\tilde{\gamma}_1}{4} - \frac{\tilde{\gamma}_2}{16}\right)\tilde{B}^2 + \left(\frac{\tilde{\gamma}_1}{2} - \frac{\tilde{\gamma}_2}{2}\right)\tilde{B}^4 - \tilde{\gamma}_2\tilde{B}^6 = 0, \tag{2.F.10}$$

which is a cubic equation for $\tilde{B}^2$ with a single real-valued root.

When the mode with the lower optical frequency, a_1, is driven, the synthetic electric field vanishes for small driving powers $\mathcal{P}$ and the mechanical amplitude satisfies the stationary condition (2.F.10). When driving power exceeds the threshold value

$$\mathcal{P}^{\mathrm{th}} = \left[\frac{2\,(\tilde{\gamma}_1 - 1) + \tilde{\gamma}_2}{4\tilde{\gamma}_2}\right]^2, \tag{2.F.11}$$

the synthetic electric field bifurcates to finite values

$$\tilde{\mathcal{E}} = \pm 2\sqrt{\mathcal{P} - \mathcal{P}^{\mathrm{th}}}. \tag{2.F.12}$$

The steady state is then bistable. Depending on the initial conditions, the synthetic electric field is either positive or negative. For the nonvanishing synthetic electric field, the stationary mechanical amplitude reads

$$\tilde{B} = \sqrt{\frac{\tilde{\gamma}_1 - 1}{2\tilde{\gamma}_2}}. \tag{2.F.13}$$

Above threshold, the mechanical amplitude does not depend on driving power. Importantly, light transport provided by the phonon-assisted photon tunneling is suppressed above threshold by the synthetic electric field.

To study the suppression of light propagation by the generated synthetic electric field, we use optical transmission T. It is the ratio of the output power leaking from the nondriven mode, $\kappa|a_2|^2$ (if mode a_1 is driven) or $\kappa|a_1|^2$ (if mode a_2 is driven), and the input power, $\kappa\mathcal{P}/\zeta^2$. The transmission

$$T = \frac{\tilde{B}^2}{\left(\tilde{B}^2 + \frac{1}{4}\right)^2 + \frac{1}{4}\tilde{\mathcal{E}}^2} \tag{2.F.14}$$

is suppressed by the synthetic electric field. As a result, the transmission in the direction to the higher optical frequency (mode a_1 being driven) is suppressed above threshold compared to the transmission to the lower optical frequencies (mode a_2 being driven).

The synthetic electric field $\tilde{\mathcal{E}}$ changes the relative phase $\varphi = \phi - \theta_2 + \theta_1$ between the mechanical mode and the optical modes. The relative phase is equal to

$$\varphi = \frac{\pi}{2} + \arctan\left(2\tilde{\mathcal{E}}\right), \text{ or} \tag{2.F.15}$$

$$\varphi = -\frac{\pi}{2} + \arctan\left(2\tilde{\mathcal{E}}\right), \tag{2.F.16}$$

when mode $\hat{a}_1$ or mode $\hat{a}_2$, respectively, is driven.

The model of two optical modes with tunneling assisted by the van-der-Pol oscillator reduces in the classical limit to a model similar to that studied in sections 2.4 and 2.5. In

addition to that model, the modification of the mechanical amplitude due to radiation pressure is considered. However, this modification does not qualitatively change the generation of synthetic electric fields and unidirectional light transport.

The extent by which the mechanical amplitude is modified due to radiation pressure depends on the parameter $\tilde{\gamma}_1$, which is the ratio of the optical coherence time $1/\kappa$ and the mechanical coherence time $1/\gamma_1$. For $\tilde{\gamma}_1 \ll 1$, many phonons are emitted or absorbed by photons as they decay much faster than phonons. This results in a large modification of the mechanical amplitude. On the other hand, for $\tilde{\gamma}_1 \gg 1$, the mechanical amplitude is only marginally modified by radiation pressure since the interaction of the phonon mode with bath dominates its dynamics. However, this simultaneously suppresses phonon-assisted photon tunneling. To study the dynamics of the synthetic gauge field represented by the mechanical phase, we want to eliminate the modification of the mechanical amplitude but, at the same time, to preserve phonon-assisted photon tunneling. To this end, we set $\tilde{\gamma}_1 = 10$ in the main text, which provides a good trade-off between eliminating the modification of the mechanical amplitude and preserving phonon-assisted photon tunneling.

2.G Propagation to lower optical frequencies

In this section, we analyze propagation to lower optical frequencies where no synthetic electric fields are generated. We assume the model analyzed in the main text, now in the case when the higher-frequency optical mode is driven.

Results of the analysis are shown in figure 2.G.1 and figure 2.G.2. One can see in figure 2.G.1b and figure 2.G.1d that the synthetic electric field always vanishes as the relative phase distribution is peaked around the value, $\varphi = 3\pi/2$, for all driving powers. This happens both close to the classical limit, $\zeta = 0.1$, and deep in the quantum regime, $\zeta = 1$. With increasing driving power the relative phase distribution is more peaked around the value, $\varphi = 3\pi/2$, and consequently the phase coherence measure increases, see figure 2.G.1.

Close to the classical limit, numerical simulations are restricted to small driving powers since many energy levels of the van-der-Pol oscillator have to be taken into account. The computational demand is even larger than in the case if the lower-frequency optical mode is driven. In contrast to that case, many energy levels of the nondriven

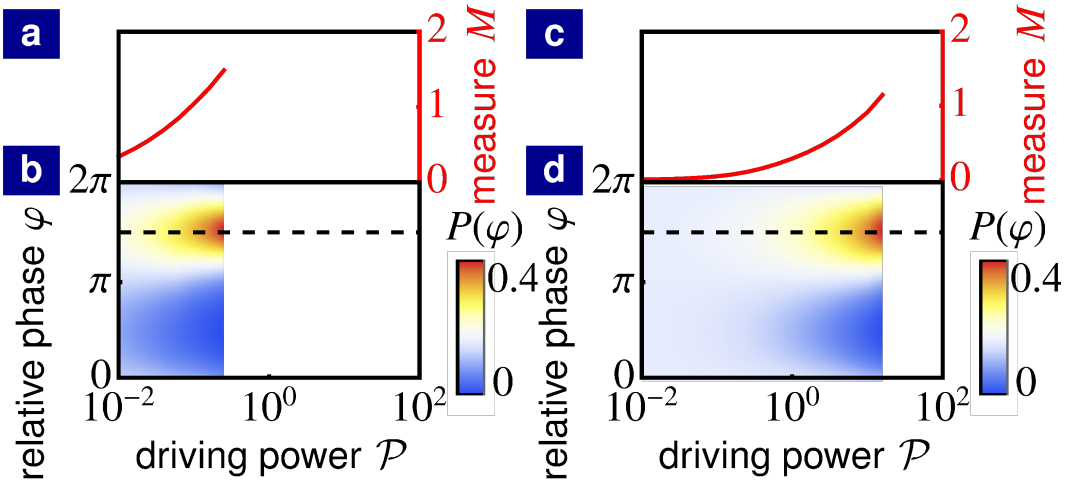

Figure 2.G.1: Relative phase between mechanical and optical modes in the case when the mode, $\hat{a}_2$, with the higher optical frequency is driven. Relative phase distribution as a function of driving power $\mathcal{P}$: (b) close to the classical limit, and (d) in the quantum regime. Corresponding phase coherence measure: (a) close to the classical limit and (c) in the quantum regime. The black dashed lines show the classical value of the relative phase. (Master equation simulations for: (a) and (b) $\tilde{\gamma}_1 = 10$, $\tilde{\gamma}_2 = 200$, and $\zeta = 0.1$; and (c) and (d) $\tilde{\gamma}_1 = 10$, $\tilde{\gamma}_2 = 40$, and $\zeta = 1$.)

optical mode are populated as the phonon-assisted photon tunneling is not suppressed for the vanishing synthetic electric field, see figure 2.G.2.

For $\zeta = 0.1$, when the quantum fluctuations are moderately strong, the mechanical amplitude according to the full quantum model (solid green line) is well approximated by its classical limit as it can be seen in figure 2.G.2a. However, in the quantum regime, for $\zeta = 1$, only a few mechanical energy levels are populated and their quantization has to be taken into account. Since the quantization of energy levels is neglected for the classical equations of motion, they predict significantly different mechanical amplitude than the full quantum model, see figure 2.G.2b.

The transmission to the lower-frequency optical mode is decreased by quantum fluctuations for any value of driving power both close to the classical limit and deep in the quantum regime, see figure 2.G.2. The transmission slightly increases with increasing driving power. This is in contrast to the large suppression of transmission to higher optical frequencies caused by the synthetic electric field (figure 2.10.2). As a result, significant isolation ratios of transmission to the lower and to the higher optical frequencies can be achieved.

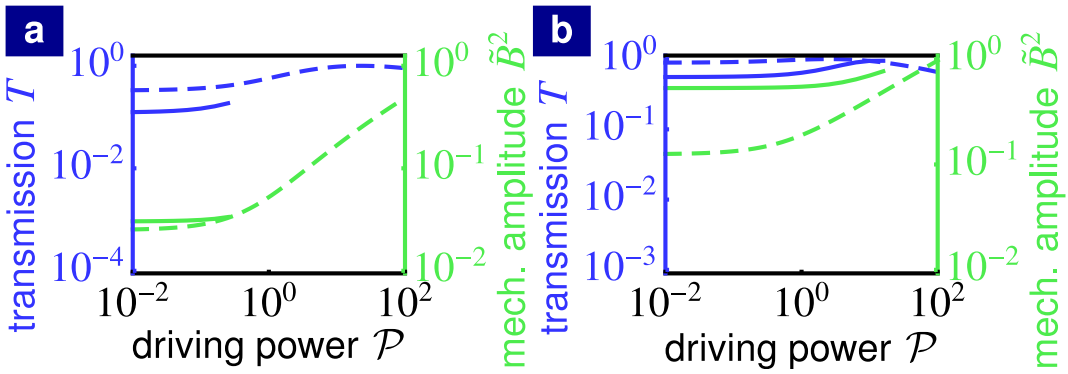

Figure 2.G.2: Light propagation through the device in the case when the mode, $\hat{a}_2$, with the higher optical frequency is driven. Optical transmission T and expectation value of the mechanical amplitude $\tilde{B}^2 = \zeta^2\langle\hat{b}^\dagger\hat{b}\rangle$ as a function of driving power $\mathcal{P}$ at the onset of a finite synthetic electric field: (a) close to the classical limit and (b) in the quantum regime. The dashed lines show classical limit. (Master equation simulations for: (a) and (b) $\tilde{\gamma}_1 = 10$, $\tilde{\gamma}_2 = 200$, and $\zeta = 0.1$; and (c) and (d) $\tilde{\gamma}_1 = 10$, $\tilde{\gamma}_2 = 40$, and $\zeta = 1$.)

2.H Numerical master equation simulations

In this section, we provide details about master equations simulations, with which the main result of this chapter were obtained.

The starting point of our analysis is the master equation (2.8.2). This equation can be rewritten as

$$\dot{\hat{\rho}} = \mathcal{L}\hat{\rho}, \tag{2.H.1}$$

in terms of the superoperator $\mathcal{L}$. We solve this equation for a steady state satisfying the equation

$$\mathcal{L}\hat{\rho} = 0. \tag{2.H.2}$$

The system described by equation (2.8.2) has a unique steady state.

To numerically solve equation (2.H.2), we express the superoperator $\mathcal{L}$ in the truncated Fock basis taking into account N_1, N_2 and N_m lowest Fock states of modes $\hat{a}_1$, $\hat{a}_2$ and $\hat{b}$, respectively. The dimensions of the matrix $\mathcal{L}$, $(N_1\,N_2\,N_m)^2 \times (N_1\,N_2\,N_m)^2$, rapidly increase with the size of the truncated Hilbert space. This represents the major restriction on occupations of optical and mechanical modes. To partially bypass this

restriction, we make use of the displacement transformation

$$\hat{\rho} \to \mathcal{D}^{\dagger}(\alpha_1, \alpha_2)\hat{\rho}\mathcal{D}(\alpha_1, \alpha_2), \tag{2.H.3}$$

where

$$\mathcal{D}(\alpha_1, \alpha_2) = e^{\alpha_1 \hat{a}_1^{\dagger} - \alpha_1^* \hat{a}_1}\, e^{\alpha_2 \hat{a}_2^{\dagger} - \alpha_2^* \hat{a}_2}, \tag{2.H.4}$$

is the displacement operator and α_j are complex numbers. The displacement transformation allows numerical simulations of strongly driven optical modes in the case when they are in a state close to a coherent state.

The master equation simulations were efficient in the case of the lower optical frequency being driven. The dynamically generated synthetic electric field suppresses the transmission to the higher-frequency optical mode. As a result, the occupation of the higher-frequency optical mode remains small and the lower-optical frequency mode is in a state close to a coherent state. In this case, the displacement transformation allows simulating a very strong coherent driving. In the case of the higher frequency being driven, the transmission is not suppressed, which leads to a large occupations also of the lower-frequency optical mode. As a result, master equation simulations are restricted to lower driving powers especially close to the classical regime where the occupation of the mechanical self-oscillator is large.

The figures in this chapter were produced for the following truncations: figures 2.10.1a, 2.10.1b and 2.10.2a for ($N_1 = 3$, $N_2 = 15$, $N_m = 15$); figures 2.10.1c, 2.10.1d and 2.10.2b for ($N_1 = 5$, $N_2 = 5$, $N_m = 5$); figures 2.10.1e, 2.10.1f and 2.10.2c for ($N_1 = 3$, $N_2 = 15$, $N_m = 15$); figures 2.G.1a, 2.G.1b and 2.G.2a for ($N_1 = 18$, $N_2 = 4$, $N_m = 11$); 2.G.1c, 2.G.1d and 2.G.2b for ($N_1 = 30$, $N_2 = 7$, $N_m = 5$) as well as figure 2.I.1 for ($N_1 = 5$, $N_2 = 5$, $N_m = 5$).

2.I Optical power spectrum in the quantum regime

In this section, we study the power spectrum of the nondriven optical mode in the quantum regime. The shift in frequency of this mode due to the time evolution of the mechanical phase corresponds the synthetic electric field.

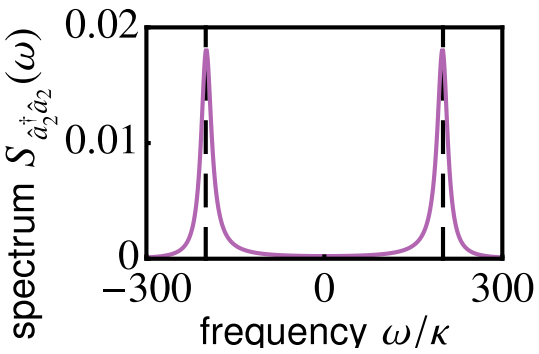

Figure 2.I.1: Power spectrum, $S_{\hat{a}_2^\dagger \hat{a}_2}(\omega)$, of the nondriven optical mode, $\hat{a}_2$, in the frame rotating with the resonant frequency, ν_2. The black dashed lines show the values of the synthetic electric field $\tilde{\mathcal{E}}$ according to the classical equations of motion. (Master equation simulations for: $\tilde{\gamma}_1 = 10$, $\tilde{\gamma}_2 = 200$, $\zeta = 1$, and $\mathcal{P} = 10000$.)

The power spectrum of the optical mode, $\hat{a}_2$, reads

$$S_{\hat{a}_2^\dagger \hat{a}_2}(\omega) = \int \mathrm{d}t\, e^{i\omega t} \langle \hat{a}_2^\dagger(t) \hat{a}_2(0) \rangle, \tag{2.I.1}$$

where $\langle \hat{a}_2^\dagger(t) \hat{a}_2(0) \rangle = \mathrm{Tr}\left[\hat{a}_2^\dagger(t) \hat{a}_2(0) \hat{\rho}_{SS}\right]$ and $\hat{\rho}_{SS}$ is the steady state density matrix. The power spectrum $S_{\hat{a}_2^\dagger \hat{a}_2}(\omega)$, can be efficiently computed in the quantum regime where only few optical and mechanical energy levels are occupied. The spectrum is depicted in figure 2.I.1 for the case where mode, $\hat{a}_1$, is driven by a laser of large power. In this case, a significant suppression of light transmission is reached, as discussed in the main text. One can see that the spectrum features two peaks at frequencies shifted from the resonant frequency ($\omega = 0$ in the rotating frame). The peaks are located at frequencies corresponding to the classical values of the synthetic electric field $\tilde{\mathcal{E}} \approx \pm 2\sqrt{\mathcal{P}}$. This shows that the synthetic electric field is generated also in the quantum regime and its values agree with the ones predicted by classical equations of motion.

The power spectrum of the nondriven optical mode demonstrates that the synthetic electric field is robust against noise. This is in contrast to the relative phase, φ, which is washed out by quantum fluctuations in the quantum regime.

3 Topological lasing

3.1 Introduction

Topological photonics has made rapid strides in the past years [33], investigating effects of gain and loss on the topology of photonic energy bands [114, 115, 116], topology in synthetic dimensions [101, 117, 118, 119] as well as the interplay of topology and nonlinear optics phenomena [120]. Lasing in topological photonic structures has recently attracted a lot of attention not only because it allows studying topology in a novel nonlinear non-Hermitian regime but also because topological structures can offer a new design of laser devices. First, lasing of zero-dimensional edge modes has been demonstrated in one-dimensional photonic arrays [121, 122, 123]. These pioneering works have been followed by experiments reporting lasing of one-dimensional chiral edge modes in two-dimensional photonic arrays [39, 43, 124, 125]. In a two-dimensional array, lasing of a single edge mode extending over the whole edge of the photonic array has been demonstrated [43]. The single-mode laser operation is robust against on-site disorder in contrast to topologically-trivial laser arrays [44]. For this reason, topological lasers are a promising candidate for highly-efficient lasers with a robust emission spectrum. The rich dynamics of topological lasers are subject to current theoretical investigation [126, 127]. However, a theory for coherence properties of topological lasers, which would be relevant for recent experiments demonstrating stable laser operation [43], is still missing.

One essential characteristic of lasers is their large temporal coherence of the emitted light field, which is required for practical applications [45]. The coherence is fundamentally limited by the phase diffusion of the light field caused by the intrinsic noise due to spontaneous emission [32]. Phase diffusion leads to a finite linewidth of the emitted light field, which, in the absence of other noise sources, is determined by the Schawlow-

Townes formula [50]. In realistic lasers, the coherence of the emitted light is affected by the dynamics of the gain medium as well as the presence of multiple lasing modes, leading to an additional broadening of the laser linewidth [128]. In this chapter, we study how the coherence of the light field emitted by a topological laser is affected by the elementary excitations around the mean-field steady state, which are excited by intrinsic noise. To focus on the effects of the elementary excitations, we neglect the dynamics of the gain medium assuming the gain medium instantaneously responds to the dynamics of the light field.

In this chapter, we consider the Haldane model based on a two-dimensional photonic array pumped along the edge. On the mean-field level neglecting quantum and thermal fluctuations in the laser, we obtain lasing of a single edge mode. Depending on initial conditions, lasing of edge modes with different lasing frequencies can be achieved as it was described in Ref. [127]. We take fluctuations into account using nonlinear semiclassical Langevin equations. We linearize the Langevin equations around the mean-field steady-state solution to study elementary excitations. We consider weak gain and loss in comparison to the coupling of optical sites in the array and a moderate size of the array such that the frequency separation of edge modes is larger that the linewidth of these modes. This regime is relevant for recent experiments on arrays of micron-scale ring resonators [23, 43]. We study how normal modes of elementary excitations are formed from the normal modes of a passive system, which does not experience either gain or loss. We show that the hybridization of edge modes gives rise to long-lived elementary excitations, which lead to large phase fluctuations and a decreased coherence of the emitted light field. The emergence of long-lived elementary excitations is not a unique feature of topological lasers as they generically appear in laser arrays with a linear frequency dispersion. However, the fact that the long-lived elementary excitations in a topological laser are formed from topological edge modes makes them robust against disorder. We show that, in contrast to long-lived elementary excitations in a trivial laser, the life-time and the oscillation frequency of these topological long-lived elementary excitations are robust against moderate on-site disorder.

The lifetime of elementary excitations strongly depends on the dispersion of edge-mode frequencies around the lasing frequency. Any deviation from a linear dispersion leads to a detuning for normal modes of elementary excitations, which can obstruct their hybridization and, as a consequence, reduce their lifetime. For lasing at frequencies

which do not lie in the middle of the passive-system band gap, the deviation from a linear dispersion is sufficient to reduce the lifetime of elementary excitations by at least one order of magnitude. This leads to a large suppression of phase fluctuations and an increase of light coherence. On the other hand, amplitude fluctuations of the emitted light field are increased resulting in a moderately larger second-order autocorrelation function. We confirm our results by numerical simulations of full Langevin equations, which take nonlinear noise dynamics into account. The results presented in this chapter are included in a preprint Ref. [3].

3.2 Topological insulators

Topological insulators are a relatively recently discovered phase of matter with unconventional conduction properties including the integer quantum Hall effect and the quantum spin Hall effect [34, 35]. In Chern insulators, which are a particular example of topological insulators, conducting channels called edge states appear on the boundary of an insulating two-dimensional bulk, leading to a quantized Hall conductance. The emergence and properties of these edge states are tied together with global properties of the insulating bulk via the *bulk-boundary correspondence*, which makes the edge states robust against local defects and imperfections in the crystalline structure of an electronic material. More recently, it was understood that topological edge states and the bulk-boundary correspondence are generic features of waves in a periodic medium. Topological properties of classical waves have been uncovered in various physical platforms such as light in photonic structures [33], mechanical waves in acoustic metamaterials [41], geophysical waves [129] and electromagnetic waves in arrays of LC circuits [42]. In this section, we provide an overview of the basic concepts in the theory of topological insulators, considering the example of an insulating two-dimensional electronic material.

An insulator is an electronic material with a gap in the electronic band structure, which is a range of energies with no allowed electronic states. To induce electron transport, a sufficient energy has to be supplied to excite electrons over the band gap, otherwise we observe a vanishing conductance at zero temperature.

Topology is a field of mathematics describing properties of geometric objects which are unchanged under continuous deformations. Two geometric objects are topologically

equivalent if we can continuously deform one object into the other. The concept of global topological properties, which are independent of particular local features that change under continuous deformations, can be employed to bring insight into the properties of insulators. In particular, we can introduce a topological classification, in which two electronic materials with a band gap are topologically equivalent if we can continuously deform one material into the other without closing the band gap.

In two-dimensional materials, topological properties of each electronic band n can be characterized by a topological invariant called a *Chern number*

$$C_n = -\frac{1}{2\pi}\int_{\mathrm{BZ}} \mathcal{B}^{(n)}\mathrm{d}\mathbf{k}, \tag{3.2.1}$$

where the integral is taken over the first Brillouin zone,

$$\mathcal{B}^{(n)} = \vec{\nabla}_k \times i\langle\psi_n|\vec{\nabla}_k|\psi_n\rangle \tag{3.2.2}$$

is the Berry curvature, $|\psi_n\rangle$ is the electronic state corresponding to the electronic band n and $\mathbf{k}$ is the quasi-momentum. The Chern number takes integer values. The sum of the Chern number over all bands is equal to zero. Using the Chern number, we can introduce a quantitative topological classification: two electronic materials are topologically equivalent if the sum of the Chern numbers over all filled bands is the same.

Interesting physics arises on the boundary of two gapped materials which are not topologically equivalent. Since we cannot continuously deform one material into the other without closing the band gap, the band gap has to close somewhere at the boundary between these two materials, giving rise to a conducting channel along the boundary. We schematically show the resulting situation in figure 3.2.1. The conducting channels correspond to edge states (figure 3.2.1b), which connect the valence (last filled) band and the conduction (first empty) band, see figure 3.2.1a.

The change of the topological Chern number, which is a property of an insulating bulk, across a boundary between two materials and the emergence of edge states on the boundary are tied together via the so-called *bulk-boundary correspondence* [130]. The bulk-boundary correspondence guarantees the appearance of *topological edge states* independent of the particular shape of the boundary. This is in contrast to conventional

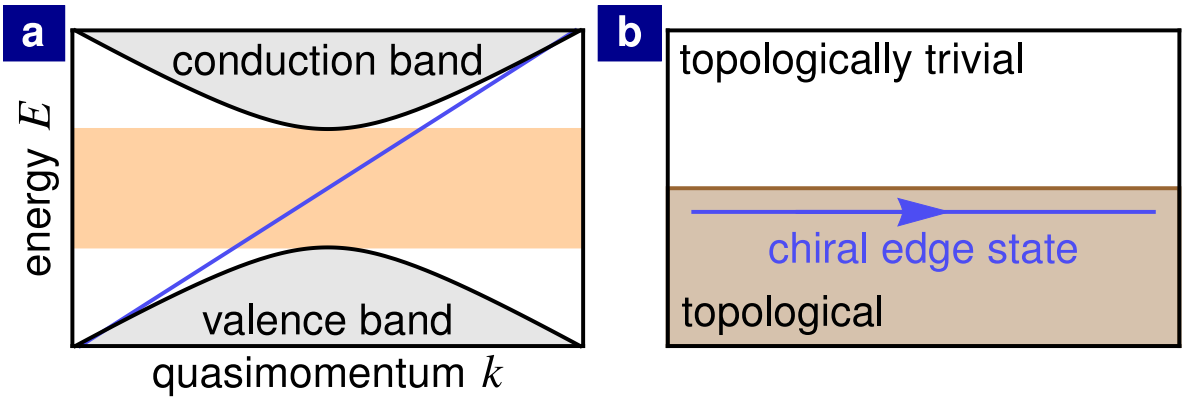

Figure 3.2.1: Boundary between two topologically inequivalent materials. (a) Band structure of a topologically nontrivial material with a band gap (orange region) between the conduction band and the valence band as well as a chiral edge state (blue line) emerging on the boundary with a topologically trivial material. (b) Boundary between topologically nontrivial material (brown) and topologically trivial material (white) as well as the chiral edge mode (blue arrow).

edge states corresponding, for example, to whispering gallery modes, which are dependent on the shape of the boundary.

Using the Chern number, we can determine the number of topological edge states, which emerge on the boundary of two materials. Each of the two materials $i = 1, 2$ is characterized by the sum $\sum_n C_n^{(i)}$ of Chern numbers over all filled bands n. The number of topological edge states on the boundary of these two materials is equal to the difference $\sum_n C_n^{(1)} - \sum_n C_n^{(2)}$ in the sum of Chern numbers. The vacuum can be thought of as a topologically trivial material with the Chern number of all bands equal to zero. As a result, the number of topological edge states on the boundary of a material with the topologically trivial vacuum is given by the sum $\sum_n C_n$ of Chern numbers over all filled bands. A material having a nonzero sum of the Chern number over all filled bands is called a *Chern insulator*.

Importantly, topological edge states are chiral, which means that they provide unidirectional electron transport along the boundary. The sign of the summed Chern number $\sum_n C_n$ over all filled bands determines the chirality of all edge states. If the summed Chern number is positive (negative), all edge states provide clockwise (counterclockwise) electron transport along the boundary.

The *integer quantum Hall effect* is historically the first observed phenomenon, which

is connected to the topology of an electronic band structure. A quantized Hall conductance was measured in a two-dimensional electron gas subject to a strong perpendicular magnetic field [131]. Within linear response theory, the Hall conductance

$$\sigma_{xy} = -\frac{e^2}{h} \sum_n C_n \tag{3.2.3}$$

can be related to the Chern number C_n of electronic energy bands, where the sum is over all filled bands n and h is Planck's constant [132]. The formula (3.2.3) for the Hall conductance can be interpreted as follows: the Hall conductance is provided by topological edge states whose total number is $\sum_n C_n$ and each edge state contributes with a quantum of conductance $-e^2/h$ [133].

Later, it was understood that the breaking of time-reversal symmetry is the fundamental ingredient leading to a topologically-nontrivial band structure and to the integer quantum Hall effect. Haldane proposed a particular example of a system with a staggered magnetic field, which breaks time-reversal symmetry, while the net magnetic field through a unit cell vanishes [134]. The fact that the integer quantum Hall effect can be observed only in systems with the broken time-reversal symmetry is consistent with the chirality of edge states as unidirectional electron transport is not compatible with time-reversal symmetry.

Topologically-trivial edge states can appear on the boundary of a material depending on the particular shape of the boundary. However, imperfections in the material such as slight variations of system parameters between unit cells or defects lead to backscattering of electrons, which largely affects the conducting properties of topologically-trivial edge states.

In contrast to trivial edge states, the appearance of topological edge states is independent of the particular shape of the boundary, guaranteed by the bulk-boundary correspondence. The chirality of topological edge states plays an important role when imperfections in a material are taken into account. Unidirectional electron transport provided by topological edge states is immune to backscattering, since there are no edge states that would provide electron transport in the reverse direction. As a result, the quantized Hall conductance is robust against imperfections and it does not depend on the particular shape of the boundary. This is commonly referred to as *topological robustness* and it is guaranteed by the topological properties of the bulk of the material

as far as the imperfections are not strong enough to close the topological band gap in the bulk.

In this section, we discussed Chern insulators, which are an example of topological insulators. In Chern insulators with a broken time-reversal symmetry, topological edge states, which are robust against imperfections, provide a quantized Hall conductance. However, topological effects are not limited to systems with broken time-reversal symmetry. If spin is taken into account, topologically-nontrivial band structure can be obtained even for the case of unbroken time-reversal symmetry, leading to the *quantum spin Hall effect* [135, 136]. In this case, the topologically-nontrivial band structure of individual spin components gives rise to Helical edge state, i.e. edge states providing transport in one direction for spin up and transport in the reverse direction for spin down. We refer the reader to reviews Refs. [34, 35] for more details about the quantum spin Hall effect, in particular, and topological insulators, in general.

3.3 Topological photonics

The topology of energy bands is a very general concept that is not limited to electrons in a solid-state material. The theory for the topology of energy bands can be straightforwardly extended to electromagnetic waves in periodic dielectrics, despite the very different nature of electrons in a solid-state material and electromagnetic waves in a dielectric.

Photonic crystals are dielectrics with a periodic change of the refractive index, which affects electromagnetic waves propagating through the crystal in the same way as a periodic potential in a solid-state material affects the movement of electrons. As a result, the propagation of electromagnetic waves can be suppressed at certain frequencies. This gives rise to a *photonic band structure*, where photonic bands (band gaps) correspond to frequencies at which the propagation is allowed (suppressed).

The topological properties of photonic bands can be characterized analogously to the topological properties of electronic bands, namely by associating a Chern number to each photonic band [17, 137]. In Refs. [17, 137], it has been proposed that the time-reversal symmetry can be broken in a photonic crystal due to the magneto-optical effect, leading to the opening of a topological band gap and a topologically-nontrivial band structure. The bulk-boundary correspondence implies the appearance of topolog-

ical edge modes on the boundary of the photonic crystal, which unidirectionally guide electromagnetic waves along the boundary. The resulting unidirectional propagation of electromagnetic waves is immune to back-scattering on imperfections in the array such as local defects or local disorder in system parameters. This is analogous to the topological robustness of chiral electron transport in topological insulators. Frequencies of edge modes lie within the topological band gap. As a result, edge-mode frequencies are protected against local imperfections as long as they are not strong enough to close the topological gap in the bulk of the photonic crystal.

A topological band structure has been implemented in a two-dimensional magneto-optical photonic crystal with a clear signature of the nontrivial band topology in a form of the unidirectional propagation of a microwave signal along the edge of the photonic crystal [18]. Similar experiments in the optical domain remain challenging due to a weak magneto-optical effect at optical frequencies. A more practical approach to implementing a topological band structure in the optical domain exploits synthetic gauge fields for photons, which give rise to an artificial magnetic field. Synthetic gauge fields can be realized using (i) a periodic modulation of photonic degrees of freedom [20] or (ii) the evanescent coupling of micron-scale ring resonators giving rise to an analogue of a tight-binding Hamiltonian [19]. Synthetic gauge fields have been experimentally realized employing the approach (i) in Ref. [138] and the approach (ii) in Ref [23]. These pioneering works have been followed by a considerable research activity in the emerging field of topological photonics, which deals with topological photonic structures [33].

Topological photonics has recently attracted a lot of attention, both implementing a new type of topological photonic devices and opening new avenues of fundamental research [33]. A robust unidirectional light propagation along the edges of topological photonic structures holds a great promise for novel photonic devices such as waveguides immune to backscattering, robust delay lines and optical isolators. The spectral robustness of edge modes can be employed to implement spectrally-robust quantum emitters and topological lasers. From the perspective of fundamental research, topological photonic structures can be employed to investigate the topology of energy bands in a novel non-Hermitian regime as loss and gain are inherently present in photonic structures. In topological photonic structures, we can also study topology in synthetic dimensions as well as the interplay of topology and optical nonlinearities. We are particularly interested in the combination of topologically-protected unidirectional light transport and

nonlinear laser amplification in topological lasers.

3.4 Topological lasers

We consider an array of optical sites, whose complex amplitudes c_j, $j = 1, ..., N$, are described by the semiclassical Langevin equations

$$i\frac{\mathrm{d}}{\mathrm{d}t}c_j = \left[\nu_j - i\gamma + i\frac{\mathbb{P}_j g}{1+\frac{|c_j|^2}{I_{\mathrm{sat}}}}\right] c_j + \sum_{k=1}^{N} H_{jk}c_k + Q_{jj}c_{j,\mathrm{in}}, \tag{3.4.1}$$

where $\hbar = 1$, ν_j are the frequencies of the optical sites, the Hamiltonian H_{jk} describes the coupling of these sites, and N is the number of the optical sites in the array. Intrinsic optical losses lead to a decay at rate γ. Incoherent pumping of optical sites is described by a saturable gain g, where I_{sat} is the saturation intensity. We allow for a spatial pump profile where $\mathbb{P}_j = 1$ for pumped sites and $\mathbb{P}_j = 0$ for not pumped sites. Incoherent pumping is associated with intrinsic noise due to spontaneous emission at rate q, which is the dominant source of fluctuations at the pumped sites. At sites without pumping, the dominant source of fluctuations is shot noise at rate 2γ. Both intrinsic noise due to spontaneous emission and shot noise can be described by Gaussian white noise $\langle c_{j,\mathrm{in}}(t)c^*_{k,\mathrm{in}}(t')\rangle = \delta_{jk}\delta(t-t')$ with a correlation matrix $\mathbf{Q}\mathbf{Q}^\dagger$, where $\mathbf{Q}$ is a diagonal matrix, $Q_{jk} = \delta_{jk}\left[\sqrt{2\gamma}(1-\mathbb{P}_j) + \sqrt{q}\mathbb{P}_j\right]$, and δ_{jk} is the Kronecker delta.

We focus on the Haldane Hamiltonian $\hat{H} = t_1\sum_{\mathrm{n.n.}}\hat{c}_j^\dagger\hat{c}_k + t_2\sum_{\mathrm{n.n.n.}}e^{i\phi_{jk}}\hat{c}_j^\dagger\hat{c}_k$ based on a honeycomb array (see Fig 3.4.1b) including the nearest-neighbor hopping with a real amplitude t_1 and the next-nearest-neighbor hopping with a complex amplitude $t_2e^{i\phi_{jk}}$ [134, 139]. $\phi_{jk} = \phi$ for hopping in the directions shown by green arrows in Fig 3.4.1b and $\phi_{jk} = -\phi$ in the reverse directions, where ϕ is the Haldane flux. In figure 3.4.1c, we plot the band structure of the passive Haldane model (black lines) for no gain and no loss in the photonic array. For $\phi \neq 0, \pi$, the time-reversal symmetry of the system is broken and a topological band gap opens (orange region). Cutting the array in the shape of an infinite strip, chiral edge modes (blue lines) appear at the boundaries of the array. Frequencies of the chiral edge modes lie in the topological band gap.

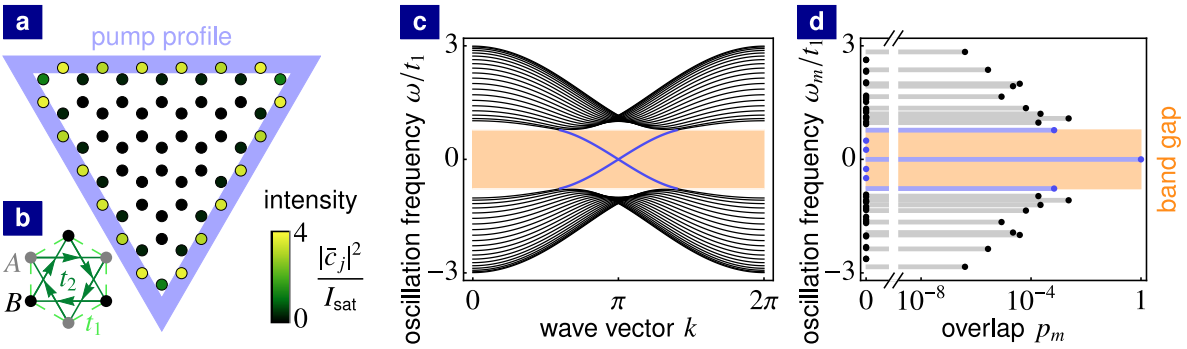

Figure 3.4.1: Mean-field steady state of topological laser. (a) The honeycomb photonic array with photon tunneling described by the Haldane model pumped in the blue region. The color scale shows the mean-field steady state occupations $|\bar{c}_j|^2$ of local optical sites. (b) Unit cell of the Haldane model consisting of the sublattice A (gray points), the sublattice B (black points), the nearest-neighbor hopping with a real tunneling t_1 and the next-nearest-neighbor hopping with a complex amplitude $t_2 e^{\phi_{jk}}$. (c) Band structure of the passive Haldane model (no gain no loss) with bulk modes (black lines), topological band gap (orange region) and topological edge modes (blue lines) for an infinite strip with zig-zag edges. (d) The overlap p_m of the mean-field steady-state solution with normal modes $\mathbf{e}^{(m)}$ of the passive system (no gain no loss) for the mode with frequency $\Omega/t_1 = 0$ lasing. (Parameters: $t_2/t_1 = 0.15$, $\phi = \pi/2$, $\gamma/t_1 = 0.01$, $g/t_1 = 0.05$, $N = 61$)

3.5 Mean-field steady state

We first find steady states of the mean-field dynamical equations for optical amplitudes, which are obtained by omitting stochastic terms in the Langevin equations (3.4.1). We consider a finite array depicted in figure 3.4.1a, where optical sites in the blue region are pumped. We assume that gain and loss are weak in comparison to the hopping amplitudes, i.e. $g, \gamma \ll t_1, t_2$. In this regime, lasing of a single topological edge mode is achieved, which was theoretically shown in Ref. [44] and experimentally demonstrated in Ref. [43]. In figure 3.4.1d, we show the overlap $p_m = |\sum_{j=1}^{N} \bar{c}_j^* e_j^{(m)}| / \sqrt{\sum_{j=1}^{N} |\bar{c}_j|^2}$ of the mean-field steady state solution $\bar{c}_j$ with the normal modes $\mathbf{e}^{(m)}$ of the passive system (no gain no loss). Depending on the initial conditions, one of the edge modes wins the gain competition. Since all edge modes extend across the whole pump region, a single edge mode saturates the gain at all pumped optical sites and prevents lasing of the other edge modes. As a result, the overlap of the mean-field steady state with a single edge mode is close to unity and the overlaps with the remaining passive-system normal modes is very small. Lasing of different edge modes leads to different lasing

frequencies and different steady-state distributions of optical phases $\bar{\theta}_j$ along the edge of the array (see figure 3.6.1a and 3.6.1b). However, the occupation of optical sites, $|\bar{c}_j|^2$, (see figure 3.4.1a) is almost identical for lasing of any edge mode, since all edge modes have very similar spatial profile $|e_j^{(m)}|^2$. The mean-field dynamics of complex amplitudes $c_j/\sqrt{I_{\mathrm{sat}}}$ and the mean-field steady state $\bar{c}_j/\sqrt{I_{\mathrm{sat}}}$ are independent of the absolute scaling I_{sat}.

3.6 Elementary excitations

The dynamics in the vicinity of a mean-field steady state can be described in terms of elementary excitations, which represent small perturbations around the steady state. These perturbations can correspond to fluctuations due to intrinsic noise or to an excitation by a weak coherent probe. All elementary excitations around a stable steady state are damped away. On the other hand, exponentially-growing elementary excitations lead to a dynamical instability of the steady state. In this section, we show how the normal modes of elementary excitations are formed from the passive-system normal modes.

To study elementary excitations around the mean-field steady state, we decompose optical amplitudes $c_j = (\bar{c}_j + \delta c_j)\, e^{-i\Omega t}$ into the mean-field steady-state solution $\bar{c}_j$ and a modulation δc_j, where Ω is the frequency of the lasing mode. Considering small modulations around the mean-field steady state, we derive the linear Langevin equations

$$i\frac{\mathrm{d}}{\mathrm{d}t}\begin{pmatrix}\delta\mathbf{c}\\ \delta\mathbf{c}^*\end{pmatrix} = \mathcal{D}\begin{pmatrix}\delta\mathbf{c}\\ \delta\mathbf{c}^*\end{pmatrix} + \mathcal{Q}\begin{pmatrix}\mathbf{c}_{\mathrm{in}}e^{i\Omega t}\\ \mathbf{c}_{\mathrm{in}}^*e^{-i\Omega t}\end{pmatrix}, \tag{3.6.1}$$

where $\mathcal{D}$ is the dynamical matrix for elementary excitations around the mean-field steady state, $\mathcal{Q} = \mathbf{Q}\otimes\sigma_z$ and σ_z is the Pauli matrix. See appendix 3.A for the derivation of equation (3.6.1). The dynamical matrix

$$\mathcal{D} = \mathcal{H} + \mathcal{A} = \begin{pmatrix}\mathbf{H} - \Omega\,\mathbb{1} & 0\\ 0 & -\mathbf{H}^* + \Omega\,\mathbb{1}\end{pmatrix} + i\begin{pmatrix}\mathbf{\Gamma} & \mathbf{\Delta}\\ \mathbf{\Delta}^* & \mathbf{\Gamma}\end{pmatrix} \tag{3.6.2}$$

can be decomposed into the Hermitian part $\mathcal{H}$ and the anti-Hermitian part $\mathcal{A}$, where

H_{jk} is the Hamiltonian of the passive system, $\mathbb{1}$ is the $N \times N$ identity matrix,

$$\Gamma_{jj} = -\gamma + \frac{\mathbb{P}_j\, g}{\left(1 + \frac{|\bar{c}_j|^2}{I_{\mathrm{sat}}}\right)^2}, \quad \Delta_{jj} = -\frac{\mathbb{P}_j\, g\, \frac{\bar{c}_j^2}{I_{\mathrm{sat}}}}{\left(1 + \frac{|\bar{c}_j|^2}{I_{\mathrm{sat}}}\right)^2}, \tag{3.6.3}$$

and $\Gamma_{jk} = \Delta_{jk} = 0$ for $j \neq k$. The dynamical matrix depends only on rescaled mean-field optical amplitudes $\bar{c}_j/\sqrt{I_{\mathrm{sat}}}$. As a result, elementary excitations do not depend on the absolute scaling, I_{sat}, of the mean-field optical amplitudes.

For elementary excitations, the number of normal modes is doubled compared to the number of passive-system normal modes. The dynamical matrix $\mathcal{D}$ exhibits the following symmetry $\mathcal{X}\mathcal{D}\mathcal{X} = -\mathcal{D}^*$, where $\mathcal{X} = \mathbb{1} \otimes \sigma_x$ and σ_x is the Pauli matrix. Due to this symmetry, the complex frequencies $\epsilon^{(\alpha)}$, $\alpha = 1, ..., 2N$, of elementary excitations are purely imaginary or appear in pairs $\left(\epsilon^{(\alpha)}, \tilde{\epsilon}^{(\alpha)}\right)$, where $\tilde{\epsilon}^{(\alpha)} = -\left(\epsilon^{(\alpha)}\right)^*$.

We first diagonalize the Hermitian part $\mathcal{H}$ by switching to the basis of passive-system normal modes $\mathcal{E}_p^{(m)} = \mathbf{e}^{(m)} \otimes (1,0)^T$ and $\tilde{\mathcal{E}}_p^{(m)} = \left(\mathbf{e}^{(m)}\right)^* \otimes (0,1)^T$, where $\mathbf{e}^{(m)}$, $m = 1, ..., N$, are eigenmodes of $\mathbf{H}$. The eigenfrequencies of the Hermitian part are directly formed from the passive-system eigenfrequencies ω_m , giving rise to two branches $\epsilon_p^{(m)} = \omega_m - \Omega$ and $\tilde{\epsilon}_p^{(m)} = -\omega_m + \Omega$. The anti-Hermitian part

$$\tilde{\mathcal{A}} = i \begin{pmatrix} \tilde{\mathbf{\Gamma}} & \tilde{\mathbf{\Delta}} \\ \tilde{\mathbf{\Delta}}^* & \tilde{\mathbf{\Gamma}}^* \end{pmatrix} \tag{3.6.4}$$

introduces a coupling between passive-system normal modes, where $\tilde{\mathbf{\Gamma}} = \mathbf{U}^\dagger\, \mathbf{\Gamma}\, \mathbf{U}$, $\tilde{\mathbf{\Delta}} = \mathbf{U}^\dagger\, \mathbf{\Delta}\, \mathbf{U}^*$. Columns of the transformation matrix $\mathbf{U}$ are eigenmodes $\mathbf{e}^{(m)}$. Due to the anti-Hermitian coupling, the passive-system normal modes hybridize.

We now discuss the coupling of modes $\mathcal{E}_p^{(m)}$ and $\tilde{\mathcal{E}}_p^{(n)}$ from the two different branches due to the off-diagonal blocks $\tilde{\mathbf{\Delta}}$ and $\tilde{\mathbf{\Delta}}^*$ of the dynamical matrix. The coupling between modes $\mathcal{E}_p^{(m)}$ and $\tilde{\mathcal{E}}_p^{(n)}$ is described by the 2×2 dynamical matrix

$$\tilde{\mathcal{D}}^{(m,n)} = \begin{pmatrix} \omega_m - \Omega & 0 \\ 0 & -\omega_n + \Omega \end{pmatrix} + i \begin{pmatrix} \tilde{\Gamma}_{mm} & \tilde{\Delta}_{mn} \\ \tilde{\Delta}^*_{nm} & \tilde{\Gamma}_{nn} \end{pmatrix}, \tag{3.6.5}$$

if their frequencies are isolated from the rest of the passive-system spectrum, i.e. $|\omega_{m/n} + \omega_q - 2\Omega| \gg |\tilde{\Delta}_{m/nq}|$, $|\omega_{m/n} - \omega_q| \gg \tilde{\Gamma}_{m/nq}$ for all $q \neq m, n$. The frequencies of the edge

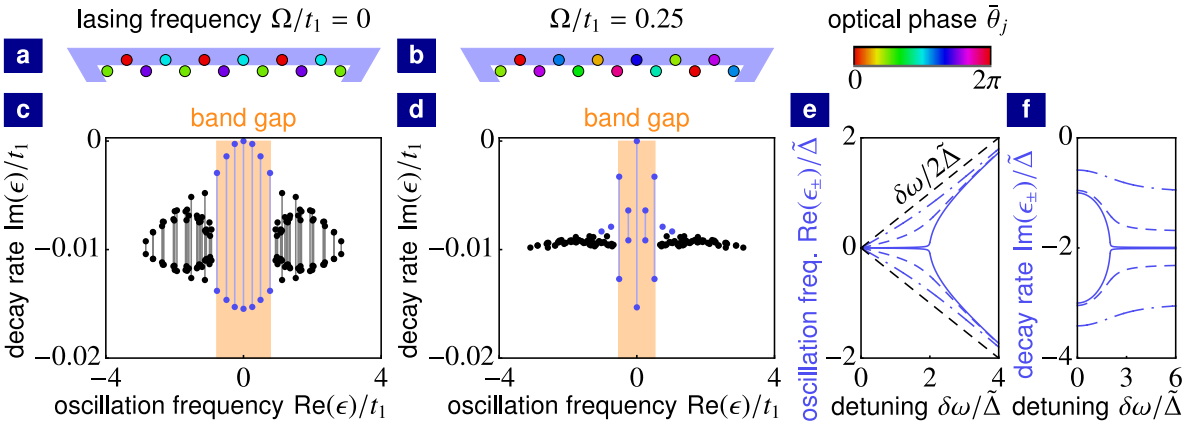

Figure 3.6.1: Elementary excitations for lasing of different edge modes. (a) and (b) Mean-field steady-state distribution of optical phases along the top edge of the photonic array for the lasing frequency $\Omega/t_1 = 0$ and $\Omega/t_1 = 0.25$, respectively. (c) and (d) Complex spectrum of elementary excitations with band gap (orange region), bulk modes (black points) as well as edge modes (blue points) for the lasing frequency $\Omega/t_1 = 0$ and $\Omega/t_1 = 0.25$, respectively. Gray and blue lines show the splitting in imaginary parts of complex frequencies due to the hybridization of bulk modes and edge modes, respectively. (e) and (f) Real part and imaginary part, respectively, of complex frequencies $\epsilon_\pm$ for two hybridized modes as a function of the detuning $\delta\omega$ for different values of the decay-rate difference $\delta\Gamma/\tilde{\Delta} = 0.02$ (full lines), $\delta\Gamma/\tilde{\Delta} = 0.6$ (dashed lines) and $\delta\Gamma/\tilde{\Delta} = 2$ (dot-dashed lines). (Parameters: (a-d) $t_2/t_1 = 0.15$, $\phi = \pi/2$, $\gamma//t_1 = 0.01$, $g/t_1 = 0.05$, $N = 61$; (e) and (f) $\bar{\omega}/\tilde{\Delta} = 0$, $\bar{\Gamma}/\tilde{\Delta} = -2$)

modes in the band gap of the passive system satisfy this condition for moderate system sizes and for $t_1, t_2 \gg g, \gamma$ as considered in this work. Diagonalizing the 2×2 dynamical matrix, we obtain complex frequencies of hybridized modes

$$\epsilon_\pm^{(m,n)} = \bar{\omega}_{mn} - i\bar{\Gamma}_{mn} \pm \frac{1}{2}\sqrt{(\delta\omega_{mn} + i\delta\Gamma_{mn})^2 - 4|\tilde{\Delta}_{mn}|^2}, \tag{3.6.6}$$

where $\bar{\omega}_{mn} = (\omega_m - \omega_n)/2$, $\delta\omega_{mn} = \omega_m + \omega_n - 2\Omega$, $\bar{\Gamma}_{mn} = -\left(\tilde{\Gamma}_{mm} + \tilde{\Gamma}_{nn}\right)/2$, and $\delta\Gamma_{mn} = \tilde{\Gamma}_{mm} - \tilde{\Gamma}_{nn}$. The real parts of complex frequencies correspond to oscillation frequencies and the imaginary parts of complex frequencies correspond to decay rates or amplification rates. The real part and the imaginary part of the complex frequencies $\epsilon_\pm^{(m,n)}$ are shown in figures 3.6.1e and 3.6.1f, respectively, as a function of the detuning $\delta\omega_{mn}$. One can see that due to the anti-Hermitian coupling of passive-system normal modes, the real parts of the complex frequencies are attracted to each other,

$\mathrm{Re}\left(\epsilon_+^{(m,n)} - \epsilon_-^{(m,n)}\right) < |\delta\omega_{mn}|$. On the other hand, the imaginary parts of the complex frequencies split. This is an example of level attraction, which is a general concept appearing in various physical platforms [140, 141, 142]. For $2\bar{\Gamma}_{mn} > \sqrt{\delta\Gamma_{mn} + 4|\tilde{\Delta}|^2}$, both hybridized modes decay as the imaginary parts of the complex frequencies are negative. The splitting in the imaginary parts of the complex frequencies is large for small detunings $\delta\omega$ leading to a slowly-decaying mode and a fast-decaying mode. For a large detuning $|\delta\omega_{mn}| \gg |\tilde{\Delta}_{mn}|$, the hybridization is negligible and the frequencies of uncoupled modes $\epsilon_+^{(m,n)} \approx \omega_m - \Omega + i\tilde{\Gamma}_{mm}$ as well as $\epsilon_-^{(m,n)} \approx -\omega_n + \Omega + i\tilde{\Gamma}_{nn}$ are recovered.

The hybridization of two edge modes from the two different branches described by the 2×2 dynamical matrix $\tilde{\mathcal{D}}^{(m,n)}$ will be shown in the next section to have important consequences for the complex spectrum of elementary excitations.

3.7 Spectrum of elementary excitations

We now investigate the complex spectrum of elementary excitations in the regime $t_1, t_2 \gg g, \gamma$. In figure 3.6.1d, we plot the complex spectrum of elementary excitations for lasing of the edge mode with the frequency $\Omega/t_1 = 0.25$. This spectrum reveals generic features of elementary excitations in topological lasers.

Normal modes of elementary excitations are formed from either bulk modes (black points) or edge modes (blue points) of the passive system. In the regime $t_1, t_2 \gg g, \gamma$, the oscillation frequencies (real parts of complex frequencies) of elementary excitations are predominantly determined by the eigenfrequencies of the Hermitian part $\mathcal{H}$, which consists of two branches $\epsilon_p^{(m)} = \omega_m - \Omega$ and $\tilde{\epsilon}_p^{(m)} = -\omega_m + \Omega$ formed from the passive system frequencies ω_m. These two branches are shifted with respect to each other by the lasing frequency Ω. Since the lasing frequency lies in the passive-system band gap, the band gaps of the two branches overlap, giving rise to a band gap in the spectrum of elementary excitations (orange region in figure 3.6.1d). The band gap in the spectrum of elementary excitations represents a range of frequencies within which no bulk modes are excited by elementary excitations. As the lasing frequency $\Omega/t_1 = 0.25$ does not lie in the middle of the passive-system band gap, the band gaps of the two branches overlap only partially. As a result, the band gap in the spectrum of elementary excitations is smaller than that of the passive system.

All imaginary parts of complex frequencies are negative (except from a single frequency with a vanishing imaginary part discussed later) confirming the stability of the steady state. For the moderate system sizes that we consider here, $|\omega_m - \omega_n| \gg g, \gamma$ for all $m \neq n$ and edge-mode frequencies ω_m lying in the band gap of the passive system. As a result, every edge mode $\mathcal{E}_p^{(m)}$ can significantly hybridize only with a single mode $\tilde{\mathcal{E}}_p^{(n)}$ from the other branch and their coupling is described by the 2×2 dynamical matrix (3.6.5). Due to the large spatial overlap of edge modes in the pumped region $\mathbb{P}_j$, the coupling $|\tilde{\Delta}_{mn}|$ between edge modes overcomes the detuning of their passive-system frequencies $|\delta\omega_{mn}|$. This leads to a large hybridization of edge modes and to a distinctive splitting in the imaginary parts of their complex frequencies (blue lines in figure 3.6.1d).

Two passive-system normal modes formed from the lasing mode $\mathbf{e}^{(l)}$ are always degenerate at frequency $\epsilon_p^{(l)} = \tilde{\epsilon}_p^{(l)} = 0$. The hybridization of these two modes gives rise to a non-decaying mode with the complex frequency $\epsilon_+^{(l,l)} = 0$ and a fast-decaying mode with the complex frequency $\epsilon_-^{(l,l)} = -2i\bar{\Gamma}_{ll}$ (see appendix 3.B for more details). These non-decaying and fast-decaying excitations correspond to undamped fluctuations in the phase of the lasing mode and largely-damped fluctuations in the amplitude of the lasing mode, respectively, which are characteristic for a laser driven above threshold [32].

Note that the hybridization of edge modes $\mathcal{E}_p^{(m)}$ and $\mathcal{E}_p^{(n)}$ from the same branch is negligible because the detuning of passive-system frequencies $|\delta\omega_{mn}| = |\omega_m - \omega_n|$ is always larger than the coupling term $|\tilde{\Gamma}_{mn}|$ between these modes.

Since couplings $\tilde{\Delta}_{nm}$ and $\tilde{\Gamma}_{nm}$ between bulk modes are small, the hybridization of bulk modes is typically also negligible. Complex frequencies of non-hybridized bulk modes (black points in figure 3.6.1d) acquire imaginary parts $\mathrm{Im}\,\epsilon^{(m)} \approx -\gamma$ and $\mathrm{Im}\,\tilde{\epsilon}^{(m)} \approx -\gamma$ due to the diagonal term $\tilde{\Gamma}_{mm} \approx -\gamma$ in the anti-Hermitian part of the dynamical matrix.

Note that for the value of the Haldane flux $\phi = \pi/2$, a small hybridization of bulk modes occurs for lasing at the frequency $\Omega/t_1 = 0$ (see figure 3.6.1c), because bulk modes are pairwise degenerate due to the symmetry, $\mathbf{S}\,\mathbf{H}\,\mathbf{S} = -\mathbf{H}^*$, of the passive-system Hamiltonian $\mathbf{H}$, where $\mathbf{S}$ is a unitary and $\mathbf{S}^2 = \mathbb{1}$ (see appendix 3.C for more details). However, the splitting in imaginary parts of complex frequencies for bulk modes is small in comparison to the splitting for edge modes and the hybridization of bulk modes does not appear for other values of the Haldane flux $\phi \neq \pi/2$ or for other

lasing frequencies $\Omega/t_1 \neq 0$.

3.8 Long-lived elementary excitations

We now discuss long-lived elementary excitations, which occur in the Haldane model for lasing at a frequency lying in the middle of the passive-system band gap (vicinity of $\Omega/t_1 = 0$ for $\phi \approx \pi/2$).

In figure 3.6.1c, we plot the complex spectrum of elementary excitations for lasing at the frequency $\Omega/t_1 = 0$, which lies in the middle of the passive-system band gap. Long-lived elementary excitations with decay rates, which are orders of magnitude smaller than any other energy scale in the system (γ, g, t_1 and t_2), appear due to a large hybridization of edge modes. The very slow decay of long-lived elementary excitations leads to an ultra slow relaxation of the topological laser towards the mean-field steady state, which was numerically observed in Ref. [127]. In contrast to lasing at the frequency $\Omega/t_1 = 0$, decay rates of slowly-decaying modes are comparable to γ for the lasing at the frequency $\Omega/t_1 = 0.25$ (see figure 3.6.1d).

To understand the dependence of the spectrum for elementary excitations on the selection of a lasing edge mode, we can expand the edge-mode frequencies $\omega_m = \Omega + v_1 (m-l) + v_2 (m-l)^2 + \mathcal{O}\left((m-l)^3\right)$ around the lasing frequency Ω, where the index l labels the lasing mode. For $|v_1| \gg |v_2|$, the frequency of edge mode m is close to the frequency of edge mode $2l - m$ from the other branch of passive-system normal modes and their detuning is $\delta\omega_{m(2l-m)} = 2v_2 (m-l)^2 + \mathcal{O}\left((m-l)^4\right)$. If the nonlinear coefficient $|v_2|$ and, as a consequence, also the detuning $\delta\omega_{m(2l-m)}$ are small compared to the coupling $|\tilde{\Delta}_{m(2l-m)}|$ between the edge modes, the edge modes significantly hybridize giving rise to a large splitting in the imaginary part of the complex frequencies, see equation (3.6.6) and figure 3.6.1f. On the other hand, if the nonlinear coefficient $|v_2|$ is comparable to or larger than the coupling $|\tilde{\Delta}_{m(2l-m)}|$, the resulting detuning $\delta\omega_{m(2l-m)}$ obstructs the hybridization and the splitting in the imaginary parts of edge-mode frequencies is reduced.

For the Haldane model, the dispersion of edge-mode frequencies is linear in the middle of the passive-system band gap for any $\phi \neq 0, \pi$. As v_2 is very small for lasing at a frequency lying in the middle of the passive-system band gap, the long-lived elementary excitations, whose decay rate is orders of magnitude smaller than any other energy scale

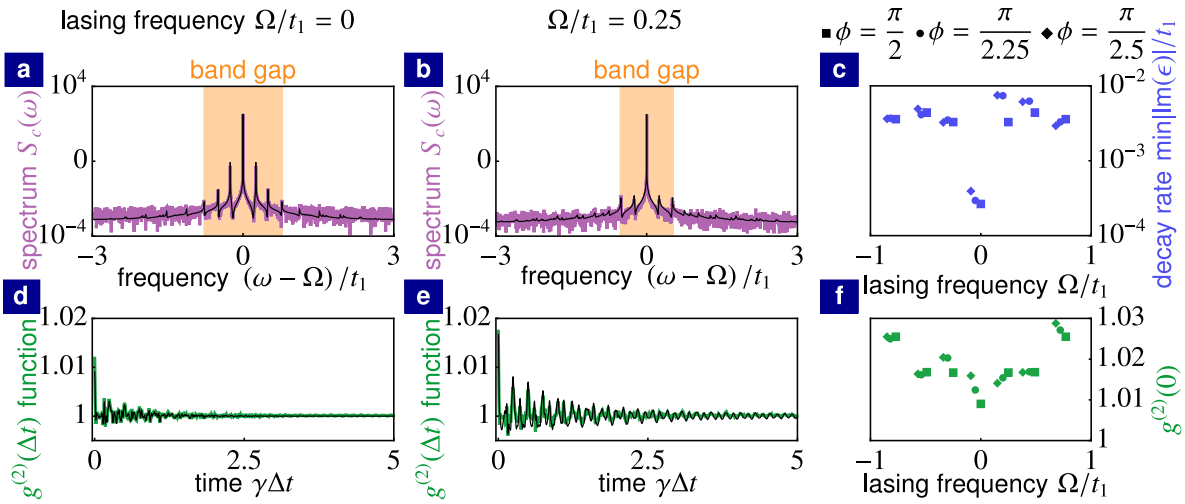

Figure 3.8.1: Coherence properties of topological lasers. (a) and (b) Optical spectrum of a pumped optical site lying at the edge of the topological array for lasing at the frequency $\Omega/t_1 = 0$ and at the frequency $\Omega/t_1 = 0.25$, respectively. Linearization of Langevin equations around the mean-field steady state (black line) and numerical simulations of nonlinear Langevin equations (purple line). The orange region shows the band gap in the spectrum of elementary excitations. (d) and (e) Second-order autocorrelation function of a pumped optical site lying at the edge of the topological array for lasing at the frequency $\Omega/t_1 = 0$ and at the frequency $\Omega/t_1 = 0.25$, respectively. Linearization of Langevin equations around the mean-field steady state (black line) and numerical simulations of nonlinear Langevin equations (green line). (c) Smallest decay rate of elementary excitations $\min_{\alpha\neq\eta}|\mathrm{Im}\,\epsilon^{(\alpha)}|$ as a function of the lasing frequency Ω for Haldane flux $\phi = \pi/2$ (squares), $\phi = \pi/2.25$ (circles) and $\phi = \pi/2.5$ (diamonds). (f) Equal-time second-order autocorrelation function $g^{(2)}(0)$ as a function of the lasing frequency Ω for Haldane flux $\phi = \frac{\pi}{2}$ (squares), $\phi = \frac{\pi}{2.25}$ (circles) and $\phi = \frac{\pi}{2.5}$ (diamonds). (Parameters: $t_2/t_1 = 0.15$, $\gamma/t_1 = 0.01$, $g/t_1 = 0.05$, $I_{\mathrm{sat}}\gamma/q = 25$; (a), (b), (d) and (e) $\phi = \pi/2$)

in the system (γ, g, t_1 and t_2), appear for any value of the Haldane flux. This can be seen in figure 3.8.1c, where we plot the smallest decay rate $\min_{\alpha\neq\eta}|\mathrm{Im}\,\epsilon^{(\alpha)}|$ (index η labels the non-decaying mode) as a function of the lasing frequency Ω for different values of the Haldane flux. On the other hand, for lasing at any frequency, which does not lie in the middle of the passive-system band gap, the nonlinear coefficient v_2 is large enough to give rise to a considerable detuning of edge mode frequencies compared to the coupling of edge modes. The hybridization of edge modes is then obstructed and the smallest decay rate is comparable to γ, see figure 3.8.1c.

Long-lived elementary excitations are not unique to topological lasers. They generically appear in one-dimensional arrays if the dispersion of the passive frequencies is linear around the lasing frequency, see appendix 3.D for more details. However, in contrast to topological lasers, long-lived elementary excitations in topologically trivial lasers are sensitive to disorder. Even moderate disorder in the on-site frequencies ν_j can obstruct or enhance the hybridization of the passive-system normal modes, leading to a large change in the decay rate of the long-lived elementary excitations as well as in their oscillation frequency, see appendix 3.G. On the other hand, long-lived elementary excitations in a topological laser ($\phi \neq 0, \pi$) are robust against moderate on-site disorder. Their decay rate is only marginally affected and thus it remains orders of magnitude smaller than γ in the presence of disorder (see appendix 3.F for more details). The oscillation frequency of long-lived elementary excitations is unaffected by the disorder. The long-lived elementary excitations are robust against disorder since they appear due to the hybridization of topological edge modes, which are protected against disorder as long as disorder is not strong enough to close the topological band gap [23, 44].

In general, long-lived elementary excitations appear due to the hybridization of edge modes for any topological model with a linear dispersion of edge-mode frequencies. The lifetime of elementary excitations can be suppressed by selecting a lasing frequency around which the dispersion of edge-mode frequencies is no longer linear. The long-lived elementary excitations will be shown in the next section to have crucial consequences for light coherence.

3.9 Coherence properties

We now discuss coherence properties of topological lasers and how they are influenced by long-lived elementary excitations, investigating the emission spectrum of pumped optical sites and the second-order autocorrelation function.

We start by studying the autocorrelation of complex optical amplitudes $\langle c_j(t) c_j^*(t+\Delta t)\rangle$. The dominant contribution in this autocorrelation is determined by phase fluctuations $\delta\theta_j$, where $c_j = \left(\bar{C}_j + \delta C\right)\, e^{i\left(-\Omega t + \bar{\theta}_j + \delta\theta_j\right)}$ and $\bar{c}_j = \bar{C}_j e^{i\bar{\theta}_j}$ (see appendix 3.E for more details). The amplitude fluctuations δC_j are negligible in comparison to the large mean-field occupation $\bar{C}_j^2$ [32]. Amplitude fluctuations δC_j and phase fluctuations $\delta\theta_j$ are linearly related to the fluctuations of complex amplitudes δc_j and δc_j^* as well as to

the normal modes of the elementary excitations

$$\begin{pmatrix} \delta\mathbf{C} \\ \delta\mathbf{\Theta} \end{pmatrix} = \mathcal{W}\mathcal{N}, \tag{3.9.1}$$

where $\delta\Theta_j = \bar{C}_j\,\delta\theta_j$, the vector $\mathcal{N}$ contains the complex amplitudes of the normal modes and $\mathcal{W}$ is the transformation matrix. This allows us to express the autocorrelations of complex optical amplitudes

$$\begin{aligned} \langle c_j(t)c_j^*(t+\Delta t)\rangle &\approx \bar{C}_j^2\, e^{i\Omega\Delta t - |\Delta t|/\tau_c} \\ &+ \sum_{\alpha\neq\eta} n_\alpha |\mathcal{W}_{(j+N)\alpha}|^2\, e^{i\left(\mathrm{Re}\,\epsilon^{(\alpha)}+\Omega\right)\Delta t + \mathrm{Im}\,\epsilon^{(\alpha)}|\Delta t|} \end{aligned} \tag{3.9.2}$$

in terms of the complex frequencies of elementary excitations $\epsilon^{(\alpha)}$ and the occupations $n_\alpha = \frac{1}{2|\mathrm{Im}\,\epsilon^{(\alpha)}|}\left(\mathcal{R}\mathcal{R}^\dagger\right)_{\alpha\alpha}$ of the corresponding normal modes, where

$$\tau_c = 2\bar{C}_j^2 |\mathcal{W}_{(j+N)\eta}|^{-2} / \left(\mathcal{R}\mathcal{R}^\dagger\right)_{\eta\eta} \tag{3.9.3}$$

is a coherence time, the index η labels the non-decaying mode, and

$$\mathcal{R}\mathcal{R}^\dagger = \frac{1}{2}\mathcal{W}^{-1}\mathcal{Q}\mathcal{Q}^\dagger\left(\mathcal{W}^{-1}\right)^\dagger \tag{3.9.4}$$

is the correlation matrix for the normal modes (see appendix 3.E for a detailed derivation).

The Fourier transform of the autocorrelation $\langle c_j(t)c_j^*(t+\Delta t)\rangle$ is the optical spectrum $S_{c_j}(\omega)$. The light field emitted by optical sites is proportional to the complex amplitudes of the optical sites as described by the input-output formalism [32]. As a result, the emission spectrum is proportional to the optical spectrum $S_{c_j}(\omega)$. The optical spectrum of a pumped optical site located at the edge of the array is shown in figures 3.8.1a and 3.8.1b for lasing at the frequency $\Omega/t_1 = 0$ and $\Omega/t_1 = 0.25$, respectively. We find a good quantitative agreement between the optical spectrum determined from the linearized Langevin equations (black lines), see equation (3.9.2), and the optical spectrum obtained from numerical simulations (purple line) of the nonlinear Langevin equations (3.4.1). The ensemble average $\langle c_j(t)c_j^*(t+\Delta t)\rangle$ can be replaced by a time average for a steady-state laser operation.

For lasing at both frequencies, the optical spectrum contains a central peak at the lasing frequency corresponding to the first term in equation (3.9.2). Undamped fluctuations in the phase of the lasing mode associated with the non-decaying normal mode of elementary excitations lead to a phase diffusion of light field, giving rise to a Lorentzian shape of the central peak with a linewidth $2/\tau_c$ [32]. The linewidth is proportional to the strength of fluctuations q as well as inversely proportional to the number of pumped sites and the occupation of the pumped optical site $\bar{C}_j^2$. The linewidth is approximately constant for lasing of any edge mode. Small deviations in the linewidth occur due to moderate discrepancies in the spatial profile $|\mathcal{W}_{j\alpha}|^2$ of individual edge modes.

For lasing at the frequency $\Omega/t_1 = 0$ lying in the middle of the passive-system band gap, the optical spectrum contains also satellite peaks (see figure 3.8.1a). The satellite peaks appear due to the incoherent population of normal modes for elementary excitations, corresponding to the terms on the second line of equation (3.9.2). The occupation n_α of normal modes for elementary excitations is inversely proportional to the decay rate $|\mathrm{Im}\,\epsilon^{(\alpha)}|$ and proportional to the strength of noise q. As a result, long-lived elementary excitations with a very small decay rate are largely populated giving rise to the satellite peaks in the optical spectrum. This large incoherent population of normal modes for elementary excitations leads to large phase fluctuations in the emitted light field decreasing its coherence.

Since elementary excitations are not dependent on the absolute scaling, I_{sat}, of the mean-field steady-state solution, the occupation of normal modes n_α does not depend on the mean number of photons in the lasing mode $\bar{n}$. As a result, the height of the satellite peaks is also independent of the mean number of photons in the lasing mode $\bar{n}$.

Our results show that large phase fluctuations and the decreased light coherence of emitted light field persist even when moderate on-site disorder is introduced (see appendix 3.F). This is due to the robustness of edge modes and their frequencies against disorder. As a result, long-lived elementary excitations with a very small decay rate and a large occupation n_α of the corresponding normal modes occur even if moderate on-site disorder is considered.

On the other hand, the incoherent population of elementary excitations and corresponding phase fluctuations can be suppressed by selecting a different lasing frequency. As it was shown in the previous section, the lifetime of elementary excitations is reduced

by at least one order of magnitude for lasing at a frequency which does not lie in the middle of the passive-system band gap, see figure 3.8.1c. As a result, the incoherent population of elementary excitations and the corresponding satellite peaks in the optical spectrum are suppressed (see figure 3.8.1b) leading to a larger coherence of emitted light than for $\Omega/t_1 = 0$.

The second-order autocorrelation function $g_j^{(2)}$ describes correlations in the intensity of emitted light at different times [32]. For a laser, it is desirable that these intensity correlations vanish corresponding to $g_j^{(2)} = 1$. The second-order autocorrelation function is determined by amplitude fluctuations [32]

$$\begin{aligned} g_j^{(2)}(\Delta t) &= \frac{\langle c_j(t)c_j(t+\Delta t)c_j^*(t+\Delta t)c_j^*(t)\rangle}{\langle c_j(t)c_j^*(t)\rangle\langle c_j(t+\Delta t)c_j^*(t+\Delta t)\rangle} \\ &= 1 + \frac{4}{\bar{C}_j^2}\langle \delta C_j(t)\delta C_j(t+\Delta t)\rangle + \mathcal{O}\left(\frac{1}{\bar{C}_j^4}\right). \end{aligned} \tag{3.9.5}$$

Amplitude autocorrelations $\langle \delta C_j(t)\delta C_j(t+\Delta t)\rangle$ can be expressed in terms of normal modes correlations (see appendix 3.E). The second-order autocorrelation function $g_j^{(2)}(\Delta t)$ for a pumped optical site located at the edge of the array is shown in figures 3.8.1d and 3.8.1e for lasing at the frequency $\Omega/t_1 = 0$ and $\Omega/t_1 = 0.25$, respectively. We compare the results determined from the linearized Langevin equations (black line) to numerical simulations (green line) of the nonlinear Langevin equations (3.4.1). The ensemble average $\langle c_j(t)c_j(t+\Delta t)c_j^*(t+\Delta t)c_j^*(t)\rangle$ can be replaced by a time average for a steady-state laser operation.

For lasing at both frequencies, the equal-time second-order autocorrelation function $g_j^{(2)}(0)$ is close to unity as expected for a laser, which is driven well above threshold. With the time difference Δt, $g_j^{(2)}(\Delta t)$ decays to unity at time comparable to $1/\gamma$. This shows that amplitude fluctuations correspond to fast-decaying elementary excitations. We can see that $g_j^{(2)}(0)$ and temporal oscillations of $g_j^{(2)}(\Delta t)$ are larger for lasing at the frequency $\Omega/t_1 = 0.25$ than for lasing at the frequency $\Omega/t_1 = 0$ lying in the middle of the band gap.

In figure 3.8.1f, we plot $g_j^{(2)}(0)$ as a function of the lasing frequency Ω for different values of the Haldane flux. One can see that $g_j^{(2)}(0)$ is, in general, moderately larger for lasing at a frequency which does not lie in the middle of the band gap for all values

of the Haldane flux. This shows that lasing at these frequencies leads to moderately larger amplitude fluctuations.

In this section, we showed that long-lived elementary excitations lead to large phase fluctuations of the emitted light field and a decrease of light coherence. For this reason, long-lived elementary excitations represent a limiting feature for practical applications of topological lasers as a source of coherent light. The long-lived elementary excitations generically appear in topological lasers since they are robust against disorder. Their appearance has to be prevented if large coherence of the emitted light is desired. To this end, one can select a suitable lasing mode, for which the edge-mode dispersion is sufficiently nonlinear and, as a consequence, the lifetime of elementary excitations is largely reduced. As a result, phase fluctuations of the emitted light field are suppressed and large light coherence is achieved. On the other hand, this leads to a moderate increase in amplitude fluctuations and the second-order autocorrelation function.

3.10 Experimental parameters

We estimate parameters of our model (3.4.1) to be relevant for recent experiments [43]. Typical parameters for arrays of coupled microring resonators are the decay rate $\gamma \sim 1\,\mathrm{GHz}$ and the hopping amplitude $t_1 \sim 100\,\mathrm{GHz}$ with a feasible ratio $\gamma/t_1 \sim 0.01$ [23]. Based on the Haldane model (see Fig. 3.4.1a) with the group velocity of edge modes $v_g/t_1 \sim 1$ (in units of the lattice constant), we can estimate that the frequency separation $|\omega_m - \omega_n| \sim \gamma, g$ of edge modes $m \neq n$ is comparable to their linewidth γ and gain g for a total number of microring resonators $N \sim 10^4$. For $N \sim 100$ (as implemented in Ref. [43]), $|\omega_m - \omega_n| \gg g, \gamma$. As a result, each edge mode can distinctively hybridize only with one edge mode from the other branch of passive-system frequencies as the anti-Hermitian coupling to all other modes is negligible compared to their large frequency separation.

The dominant source of noise is the spontaneous emission at rate $q \sim 100\,\mathrm{GHz}$ [143]. A typical circulating power in the lasing mode of a single microring resonator is $P_c \sim 1\,\mathrm{mW}$ which corresponds to a typical number of photons $\bar{n} \sim 10^3$ in the lasing mode [143]. We conclude that our model with $I_{\mathrm{sat}}\gamma/q \sim 10$ describes an experimentally-relevant relative strength of noise compared to the number of photons in the lasing mode.

3.11 Conclusions

We have demonstrated that long-lived elementary excitations, which emerge due to the hybridization of topological edge modes, lead to large phase fluctuations and a decrease in the coherence of the emitted light field. In contrast to long-lived elementary excitations in a trivial laser, the decay rate and the oscillation frequency of long-lived elementary excitations in a topological laser are robust against disorder. Even though we focus in this chapter on the Haldane model, long-lived elementary excitations appear for any topological model if the dispersion of edge-mode frequencies is approximately linear around the lasing frequency. Our results for the Haldane model show that the deviation from a linear dispersion around lasing frequencies, which do not lie in the middle of the passive-system band gap, is sufficient to obstruct the hybridization of edge modes. As a result, the lifetime of elementary excitations is reduced by orders of magnitude and the phase fluctuations are largely suppressed. On the other hand, this leads to a moderate increase in amplitude fluctuations and the second-order autocorrelation function. However, the second-order autocorrelation function still remains close to unity. In the future, different topological models can be studied to provide insight into how elementary excitations in topological lasers are affected by the presence of several topological band gaps supporting edge modes with opposite chirality [33], a pseudospin degree of freedom in pseudo quantum spin Hall systems [19, 23] or topological lasing in synthetic dimensions [118].

Appendices

3.A Linearization of Langevin euqations

We now derive the linear Langevin equations (3.6.1) for elementary excitations around the mean-field steady state. To this end we substitute the decomposition of the complex optical amplitude $c_j = (\bar{c}_j + \delta c_j)\, e^{-i\Omega t}$ into the full nonlinear Langevin equations (3.4.1). Omitting second- and higher-order terms in optical modulations δc_j, we obtain the linearized Langevin equations

$$i\frac{\mathrm{d}}{\mathrm{d}t}\delta c_j = -\Omega\delta c_j + \sum_{k=1}^{N} H_{jk}\delta c_k + i\Gamma_{jj}\delta c_j + i\Delta_{jj}\delta c_j^* + Q_{jj}c_{j,\mathrm{in}}e^{i\Omega t}, \tag{3.A.1}$$

$$i\frac{\mathrm{d}}{\mathrm{d}t}\delta c_j^* = \Omega\delta c_j^* - \sum_{k=1}^{N} H_{jk}^*\delta c_k^* + i\Delta_{jj}\delta c_j + i\Gamma_{jj}\delta c_j^* - Q_{jj}c_{j,\mathrm{in}}^*e^{-i\Omega t}, \tag{3.A.2}$$

where

$$\Gamma_{jj} = -\gamma + \frac{\mathbb{P}_j\, g}{\left(1+\frac{|\bar{c}_j|^2}{I_{\mathrm{sat}}}\right)^2}, \quad \Delta_{jj} = -\frac{\mathbb{P}_j\, g\, \frac{\bar{c}_j^2}{I_{\mathrm{sat}}}}{\left(1+\frac{|\bar{c}_j|^2}{I_{\mathrm{sat}}}\right)^2}, \tag{3.A.3}$$

and we used that

$$\left[-i\gamma + i\frac{\mathbb{P}_j g}{1+\frac{|\bar{c}_j|^2}{I_{\mathrm{sat}}}}\right]\bar{c}_j + \sum_{k=1}^{N} H_{jk}\bar{c}_k = 0. \tag{3.A.4}$$

(3.A.1) and (3.A.2) can be written in form of a matrix equation (3.6.1).

3.B Non-decaying mode

Here we discuss the hybridization of two passive-system normal modes which are formed from the lasing mode, giving rise to the non-decaying mode. We label the lasing mode by the index l. Since $\omega_l = \Omega$, the pair of passive-system normal modes is degenerate $\epsilon_p^{(l)} = \tilde{\epsilon}_p^{(l)} = 0$ leading to a large hybridization of the pair. The lasing mode coincides with the mean-field steady-state solution $e_j^{(l)} \approx \bar{c}_j\, e^{i\varphi}/\sqrt{\bar{n}}$, where $\bar{n}$ is the mean number

of photons in the lasing mode and φ is an arbitrary phase. This gives

$$\bar{\Gamma}_{ll} = \tilde{\Delta}_{ll}\, e^{2i\varphi} = g \sum_{j=1}^{N} \mathbb{P}_j \, \frac{\frac{|\bar{c}_j|^4}{I_{\mathrm{sat}}\bar{n}}}{\left(1+\frac{|\bar{c}_j|^2}{I_{\mathrm{sat}}}\right)^2}, \tag{3.B.1}$$

and $\delta\Gamma_{ll}$ trivially vanishes. Using also $\bar{\omega}_{ll} = 0$ and $\delta\omega_{ll} = 0$, we see from equation (3.6.6) that the hybridization of this mode pair gives rise a non-decaying mode with the complex frequency $\epsilon_{+}^{(l,l)} = 0$ and a fast-decaying mode with the complex frequency $\epsilon_{-}^{(l,l)} = -2i\bar{\Gamma}_{ll}$.

3.C Haldane flux $\phi = \pi/2$

The value of the Haldane flux $\phi = \pi/2$ represents a special case because the Hamiltonian $\mathbf{H}$ of the passive system then exhibits the following symmetry $\mathbf{S}\,\mathbf{H}\,\mathbf{S} = -\mathbf{H}^*$, where $\mathbf{S}$ is a unitary matrix and $\mathbf{S}^2 = \mathbb{1}$. The unitary transformation $\mathbf{S}$ introduces the phase shift π between the two sublattices of the Haldane model, i.e. $c_j \to c_j$ for sublattice A and $c_j \to -c_j$ for sublattice B. Due to this symmetry, the spectrum of the passive system consists of a zero frequency and frequency pairs $(\omega_m, \omega_{\tilde{m}})$, $\omega_{\tilde{m}} = -\omega_m$. As a result, all passive-system normal modes are pairwise degenerate for $\Omega/t_1 = 0$ leading to the hybridization of all degenerate pairs described by the 2×2 dynamical matrix $\tilde{\mathcal{D}}^{(m,\tilde{m})}$, see equation (3.6.5). As the unitary $\mathbf{S}$ introduces only a local phase shift, $|e_j^{(m)}| = |e_j^{(\tilde{m})}|$ leading to $\bar{\Gamma}_{m\tilde{m}} = \tilde{\Gamma}_{mm} = \tilde{\Gamma}_{\tilde{m}\tilde{m}}$ and $\delta\Gamma_{m\tilde{m}} = 0$. Using also $\delta\omega_{m\tilde{m}} = 0$, the complex frequencies of hybridized modes are $\epsilon_{\pm}^{(m,\tilde{m})} = \omega_m + i\left(\bar{\Gamma}_{mm} \pm |\tilde{\Delta}_{m\tilde{m}}|\right)$. Since the coupling $\tilde{\Delta}_{mn}$ between bulk modes is small, the hybridization leads to a small splitting in imaginary parts of complex frequencies for bulk modes (gray lines in figure 3.6.1c). On the other hand, the large coupling of edge modes leads to a large splitting in the imaginary parts of complex frequencies (blue lines in figure 3.6.1c).

3.D One-dimensional laser array

In this appendix, we discuss how long-lived elementary excitations generically appear in one-dimensional laser arrays. We consider a one-dimensional array with N optical sites, whose complex amplitudes are described by the Langevin equations (3.4.1). All optical sites in the one-dimensional array are pumped, i.e. $\mathbb{P}_j = 1$ for all j. We do not

consider any particular Hamiltonian H_{jk}. We only assume periodic boundary conditions $c_{N+j} = c_j$, that $\nu_j = \nu = \text{const}$, and that the Hamiltonian H_{jk} is translationally invariant, i.e. that the Hamiltonian is invariant under the transformation $c_j \to c_{j+R}$ for any integer R. In this case, the passive-system normal modes are plane waves with complex amplitudes $\mathcal{N}_m = \frac{1}{\sqrt{N}} \sum_{j=1}^{N} e^{ijm} c_j$. The index m represents a quasi-momentum and it spans values $m = \frac{2\pi}{N}, \frac{4\pi}{N}, ..., 2\pi$. The mean-field equations of motion (omitting stochastic terms in the Langevin equations) for the complex amplitudes $\mathcal{N}_m$ are

$$i\frac{\mathrm{d}}{\mathrm{d}t}\mathcal{N}_m = (\omega_m - i\gamma)\,\mathcal{N}_m + \sum_{j=1}^{N} \frac{i\frac{g}{N}\sum_n e^{ij(m-n)}\mathcal{N}_n}{1 + \sum_{n,o} e^{-ij(n-o)}\mathcal{N}_n\mathcal{N}_o^*/I_{\mathrm{sat}}}, \tag{C1}$$

where ω_m is the oscillation frequency of the normal mode $\mathcal{N}_m$. These mean-field equations of motion have a stationary solution $\bar{\mathcal{N}}_m = \delta_{ml}\sqrt{N I_{\mathrm{sat}}\left(\frac{g}{\gamma} - 1\right)}\, e^{-i\varphi}$ corresponding to the lasing of a single mode l, where φ is an arbitrary phase. Note that a stationary solution exists for any normal mode l lasing. Switching back to the basis of local optical modes, the stationary optical amplitudes are $\bar{c}_j = \sqrt{I_{\mathrm{sat}}\left(\frac{g}{\gamma} - 1\right)}\, e^{-i(jl+\varphi)}$.

We linearize the full Langevin equations (3.4.1) around the stationary mean-field solution $c_j = (\bar{c}_j + \delta c_j)\, e^{-i\Omega t}$ obtaining the linearized Langevin equations (3.6.1), where $\Omega = \omega_l$. The dynamical matrix $\mathcal{D}$ is given by equation (3.6.2), where $\Gamma_{jj} = -\gamma + \frac{\gamma^2}{g} = -\bar{\gamma}$, $\Delta_{jj} = -\bar{\gamma}e^{-2i(jl+\varphi)}$, and $\Gamma_{jk} = \Delta_{jk} = 0$ for $j \neq k$. Switching to the basis of passive-system normal modes, we diagonalize the Hermitian part $\mathcal{H}$ of the dynamical matrix. Since the passive-system normal modes are plain waves, the matrix elements of the anti-Hermitian part $\tilde{\mathcal{A}}$ can be explicitly evaluated, $\tilde{\Gamma}_{mm} = -\bar{\gamma}$, $\tilde{\Delta}_{m(2l-m)} = -\bar{\gamma}e^{-2i\varphi}$, and $\tilde{\Gamma}_{mn} = \tilde{\Delta}_{m(2l-n)} = 0$ for $m \neq n$. The diagonal block $\tilde{\mathbf{\Gamma}}$ describes decay of the normal modes at rate $\bar{\gamma}$. The off-diagonal block $\tilde{\mathbf{\Delta}}$ describes the coupling of passive-system normal modes whose quasi-momenta m and n satisfy the condition $m + n = 2l$. Since this condition is satisfied only for mode pairs $(m, 2l-m)$, the coupling of passive-system normal modes is exactly described by the 2×2 dynamical matrix $\tilde{\mathcal{D}}^{(m,2l-m)}$ given by equation (3.6.5). The complex spectrum of elementary excitations is exactly determined by the eigenvalues of the 2×2 dynamical matrix

$$\epsilon_{\pm}^{(m,2l-m)} = \bar{\omega}_{m(2l-m)} - i\bar{\gamma} \pm \frac{1}{2}\sqrt{\delta\omega_{m(2l-m)}^2 - 4\bar{\gamma}^2}, \tag{C2}$$

$\bar{\omega}_{m(2l-m)} = \frac{1}{2}(\omega_m - \omega_{(2l-m)})$, $\delta\omega_{m(2l-m)} = \omega_m + \omega_{2l-m} - 2\Omega$.

The spectrum of elementary excitations in the one-dimensional laser array depends only on the dispersion of the passive system frequencies ω_m. If $|\delta\omega_{m(2l-m)}| > 0$ for all $m \neq l$, lasing of a single mode l is a stable steady state as all $\mathrm{Im}\,\epsilon_{\pm}^{(m)} < 0$ except from the non-decaying mode $\epsilon_{+}^{(l)} = 0$. We can expand the dispersion of passive-system frequencies $\omega_m = \Omega + v_1\,(m-l) + v_2\,(m-l)^2 + \mathcal{O}\left((m-l)^3\right)$ around the lasing frequency Ω. If higher order terms in the expansion are negligible, the detuning between modes m and $2l-m$ is $\delta\omega_{m(2l-m)} = 2v_2\,(m-l)^2 + \mathcal{O}\left((m-l)^4\right)$. If the nonlinear coefficient v_2 is sufficiently small such that $|v_2|(m-l)^2 \ll \bar{\gamma}$ for m close to l, the complex frequencies are $\epsilon_{+}^{(m,2l-m)} \approx \bar{\omega}_m - i\frac{v_2^2}{2\bar{\gamma}}\,(m-l)^4$ and $\epsilon_{-}^{(m,2l-m)} \approx \bar{\omega}_m - i\left[2\bar{\gamma} - \frac{v_2^2}{2\bar{\gamma}}\,(m-l)^4\right]$ corresponding to slowly-decaying modes and fast-decaying modes, respectively. For a small nonlinear coefficient v_2, the decay rate of the slowly-decaying modes can be orders of magnitude smaller than any other energy scale in the system g, γ, ω_m, leading to long-lived elementary excitations.

Long-lived elementary excitations generically appear in one-dimensional laser arrays if the dispersion of the passive-system frequencies ω_m is linear around the lasing frequency.

3.E Correlations of amplitude and phase fluctuations

Here, we provide details about how the optical spectrum and the second-order autocorrelation function are derived and how they are related to the normal modes of elementary excitations.

It is convenient to study noise in terms of amplitude and phase fluctuations, due to the $U(1)$ symmetry of the mean-field dynamical equations, $c_j \to c_j\,e^{i\varphi}$, where φ is an arbitrary overall phase. The coherence properties of a laser driven well above threshold are directly determined by the correlations in amplitude fluctuations and phase fluctuations [32]. Amplitude fluctuations δC_j and phase fluctuations $\delta\theta_j$ are linearly related to the fluctuations of complex amplitudes δc_j and δc_j^*

$$\delta C_j = \frac{e^{-i\bar{\theta}_j}\delta c_j + e^{i\bar{\theta}_j}\delta c_j^*}{2}, \quad \delta\theta_j = \frac{e^{-i\bar{\theta}_j}\delta c_j - e^{i\bar{\theta}_j}\delta c_j^*}{2i\bar{C}_j}, \tag{C1}$$

where $\bar{c}_j = \bar{C}_j e^{i\bar{\theta}_j}$. This relation can be described by the linear transformation

$$\begin{pmatrix} \delta\mathbf{C} \\ \delta\mathbf{\Theta} \end{pmatrix} = \mathcal{T} \begin{pmatrix} \delta\mathbf{c} \\ \delta\mathbf{c}^* \end{pmatrix}, \tag{C2}$$

where $\delta\Theta_j = \bar{C}_j\, \delta\theta_j$. The linearized Langevin equations around the mean-field steady-state for the amplitude and phase fluctuations are

$$i\frac{\mathrm{d}}{\mathrm{d}t} \begin{pmatrix} \delta\mathbf{C} \\ \delta\mathbf{\Theta} \end{pmatrix} = \mathcal{T}\mathcal{D}\mathcal{T}^{-1} \begin{pmatrix} \delta\mathbf{C} \\ \delta\mathbf{\Theta} \end{pmatrix} + \frac{i}{\sqrt{2}}\mathcal{Q} \begin{pmatrix} \mathbf{C}_{\mathrm{in}} \\ \mathbf{\Theta}_{\mathrm{in}} \end{pmatrix}, \tag{C3}$$

where $\mathbf{C}_{\mathrm{in}}$ and $\mathbf{\Theta}_{\mathrm{in}}$ describe real-valued Gaussian white noise, with following correlations $\langle C_{j,\mathrm{in}}(t) C_{k,\mathrm{in}}(t')\rangle = \delta_{jk}\delta(t-t')$, $\langle \Theta_{j,\mathrm{in}}(t)\Theta_{k,\mathrm{in}}(t')\rangle = \delta_{jk}\delta(t-t')$, and $\langle \bar{C}_{j,\mathrm{in}}(t)\Theta_{k,\mathrm{in}}(t')\rangle = 0$. Amplitude and phase fluctuations are linearly related to the normal modes of elementary excitations

$$\begin{pmatrix} \delta\mathbf{C} \\ \delta\mathbf{\Theta} \end{pmatrix} = \mathcal{W}\mathcal{N}, \tag{C4}$$

where $\mathcal{W} = \mathcal{V}\mathcal{T}$, columns of the matrix $\mathcal{V}$ are the normal modes of elementary excitations $\mathcal{E}^{(\alpha)}$ described in Sec. 3.6 and the vector $\mathcal{N}$ contains the complex amplitudes of these normal modes. Non-equal-time phase and amplitude autocorrelations can be expressed in terms of normal modes' correlations

$$\langle \delta C_j(t)\delta C_j(t+\Delta t)\rangle = \sum_{\alpha,\beta=1}^{2N} \mathcal{W}_{j\alpha}\langle \mathcal{N}_\alpha(t)\mathcal{N}^*_\beta(t+\Delta t)\rangle \mathcal{W}^\dagger_{\beta j}, \tag{C5}$$

$$\begin{aligned} &\langle [\delta\theta_j(t) - \delta\theta_j(t+\Delta t)]^2\rangle \\ &= \frac{1}{\bar{C}_j^2}\sum_{\alpha,\beta=1}^{2N} \mathcal{W}_{(j+N)\alpha}\langle |\mathcal{N}_\alpha(t) - \mathcal{N}_\beta(t+\Delta t)|^2\rangle \mathcal{W}^\dagger_{\beta(j+N)}. \end{aligned} \tag{C6}$$

The correlations of normal modes are

$$\langle \mathcal{N}_\alpha(t)\mathcal{N}^*_\beta(t+\Delta t)\rangle = \frac{i\left(\mathcal{R}\mathcal{R}^\dagger\right)_{\alpha\beta}}{\left(\epsilon^{(\beta)}\right)^* - \epsilon^{(\alpha)}}\, e^{i\epsilon^{(\alpha)}\Delta t},\ \Delta t < 0, \tag{C7}$$

$$\langle \mathcal{N}_\alpha(t)\mathcal{N}^*_\beta(t+\Delta t)\rangle = \frac{i\left(\mathcal{R}\mathcal{R}^\dagger\right)_{\alpha\beta}}{\left(\epsilon^{(\beta)}\right)^* - \epsilon^{(\alpha)}}\, e^{i\left(\epsilon^{(\beta)}\right)^*\Delta t},\ \Delta t > 0, \tag{C8}$$

for all normal modes α and β except from the autocorrelation of the non-decaying mode, i.e. for $\alpha = \beta = \eta$ and $\epsilon^{(\eta)} = 0$. Note that the non-decaying mode is related only to phase fluctuations. As a result, the relevant autocorrelation of the non-decaying mode is

$$\langle |\mathcal{N}_\eta(t) - \mathcal{N}_\eta(t+\Delta t)|^2 \rangle = \left(\mathcal{R}\mathcal{R}^\dagger\right)_{\eta\eta} |\Delta t|. \tag{C9}$$

The dominant contribution in the autocorrelation of complex optical amplitudes reads

$$\langle c_j(t) c_j^*(t+\Delta t) \rangle \approx \bar{C}_j^2 \, e^{i\Omega\Delta t} \, e^{-\langle [\delta\theta_j(t) - \delta\theta_j(t+\Delta t)]^2 \rangle / 2}, \tag{C10}$$

where amplitude fluctuations are neglected, since they are small in comparison to the large mean-field occupation $\bar{C}_j^2$ [32]. Using equation (C6), $\langle [\delta\theta_j(t) - \delta\theta_j(t+\Delta t)]^2 \rangle$ can be expressed in terms of correlations in the normal modes of elementary excitations (C7), (C8) and (C9) to derive the optical spectrum equation (3.9.2) in the main text, where we neglect correlations between different normal modes $\langle |\mathcal{N}_\alpha(t) - \mathcal{N}_\beta(t+\Delta t)|^2 \rangle$ for $\alpha \neq \beta$. Only long-lived elementary excitations have significant contribution to the optical spectrum due to their large occupation n_α. Since the corresponding normal modes are formed from edge modes, they have a large detuning in the real parts of complex frequencies, which suppresses the correlations between different normal modes $\langle |\mathcal{N}_\alpha(t) - \mathcal{N}_\beta(t+\Delta t)|^2 \rangle$ for $\alpha \neq \beta$.

Similarly, we can express the second-order autocorrelation function (3.9.5) in terms of correlations in the normal modes of elementary excitations.

3.F Disorder

Here we study effects of a moderate on-site disorder on the spectrum of elementary excitations and long-lived elementary excitations. We consider lasing at a frequency, which lies in the middle of the passive-system band gap. The on-site disorder is represented by a Gaussian distribution of on-site frequencies ν_j with a zero mean value and a standard deviation σ. We consider a moderate disorder with the standard deviation σ smaller than the size of the passive-system band gap $6\sqrt{3}t_2 \sin\phi$ but larger than the decay rate γ and gain g.

We compare the spectrum of elementary excitations for 30 disorder realizations and

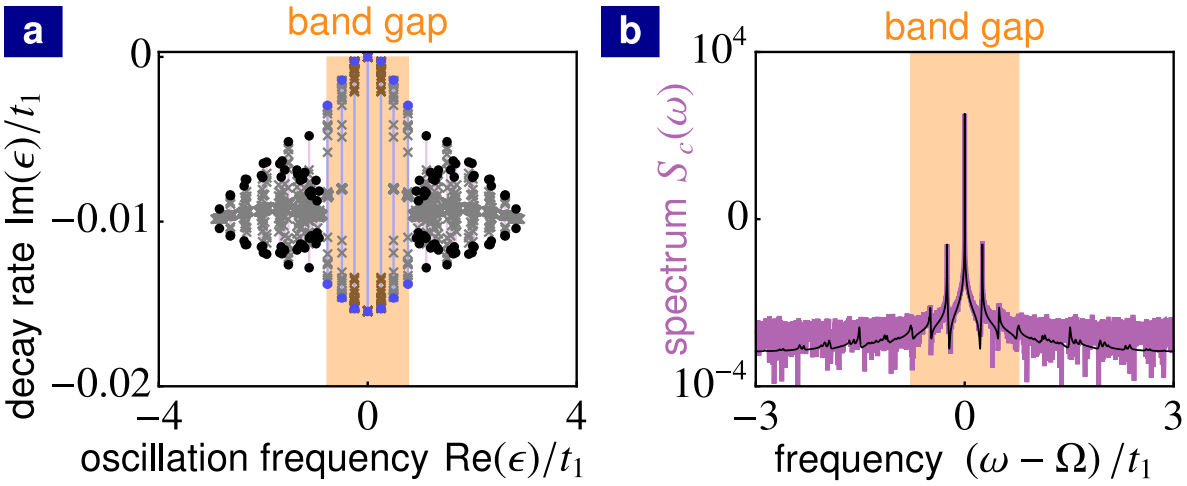

Figure 3.F.1: Effects of moderate disorder. (a) Complex spectrum of elementary excitations for 30 disorder realizations (brown and gray crosses) for $\Omega/t_1 \approx 0$ compared to complex spectrum of elementary excitations without disorder with band gap (orange region), bulk modes (black points) as well as edge modes (blue points) for the lasing frequency $\Omega/t_1 = 0$. Purple and blue lines show the splitting in imaginary parts of complex frequencies due to the hybridization of bulk modes and edge modes, respectively. (b) Optical spectrum of a pumped optical site lying at the edge of the topological array for a single disorder realization and for lasing at the frequency $\Omega/t_1 = 0.01$. Linearization of Langevin equations around the mean-field steady state (black line) and numerical simulations of nonlinear Langevin equations (purple line). The orange region shows the band gap in the spectrum of elementary excitations. (Parameters: (a) and (b) $t_2/t_1 = 0.15$, $\phi = \pi/2$, $\gamma/t_1 = 0.01$, $g/t_1 = 0.05$, $\sigma/t_1 = 0.1$; (b) $I_{\mathrm{sat}}\gamma/q = 25$, $\Omega = 0.01$)

the spectrum of elementary excitations without disorder in figure 3.F.1a. The large hybridization of edge modes with frequencies close to the lasing frequency leads to long-lived elementary excitations with a very small decay rate for all disorder realizations (brown crosses). This shows the robustness of long-lived elementary excitations against disorder. The incoherent occupation n_α of the corresponding slowly-decaying normal modes is large even in the presence of moderate on-site disorder and it leads to satellite peaks in the optical spectrum, see figure 3.F.1b.

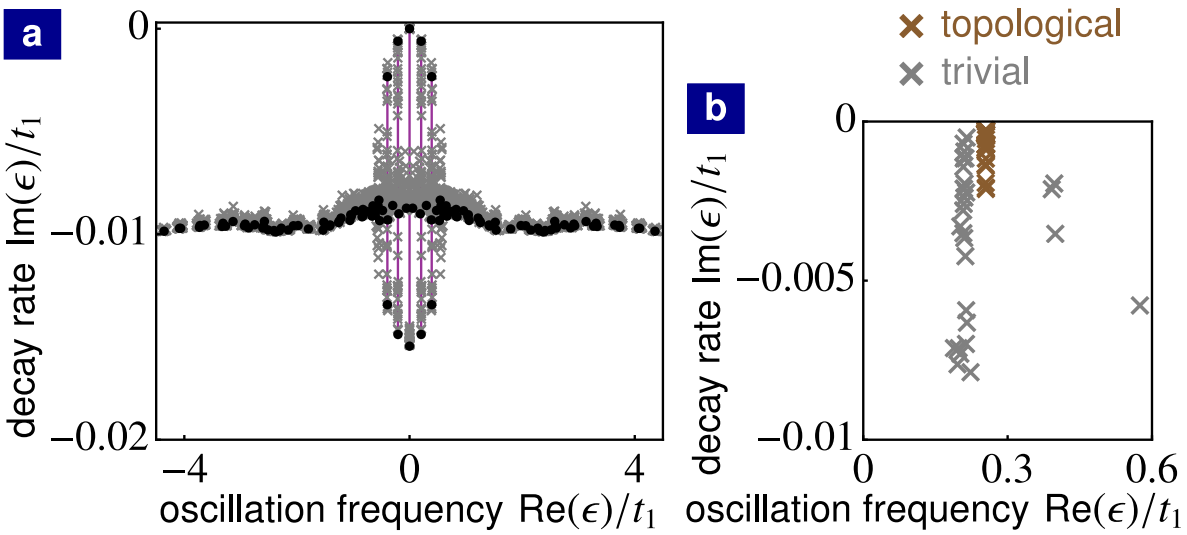

Figure 3.G.1: Effects of moderate disorder in a trivial laser based on the Haldane model compared to a topological laser. (a) Complex spectrum of elementary excitations in a trivial laser for 30 disorder realizations (gray crosses) and for the lasing frequency $\Omega/t_1 \approx 1$ compared to complex spectrum of elementary excitations without disorder (black points) for $\Omega/t_1 = 1.03$. Purple lines show the splitting in the imaginary parts of complex frequencies due to the hybridization of trivial edge modes. (b) The complex frequency with the smallest imaginary part $\min_{\alpha\neq\eta}|\mathrm{Im}\epsilon^{(\alpha)}|$ for each disorder realization (30 in total), for a trivial laser with $\Omega/t_1 \approx 1$ (gray crosses) as well as for the topological laser with $\Omega \approx 0$ (brown crosses). (Parameters: (a) and (b) $t_2/t_1 = 0.15$, $\gamma/t_1 = 0.01$, $g/t_1 = 0.05$, $\sigma/t_1 = 0.1$; (a) and (b) gray crosses $\phi = 2\pi/3$, $M/t_1 = 0.8$; (b) brown crosses $\phi = \pi/2$, $M/t_1 = 0$)

3.G Long-lived elementary excitations in a trivial laser

We now study long-lived elementary excitations in a trivial laser based on the Haldane model. We focus on the effects of disorder on the long-lived elementary excitations and we compare them to the effects of disorder on long-lived elementary excitations in a topological laser studied in appendix 3.F.

We introduce the Haldane mass term M in the Hamiltonian

$$\hat{H} = M\sum_j \mu_j \hat{c}_j^\dagger \hat{c}_j + t_1 \sum_{\text{n.n.}} \hat{c}_j^\dagger \hat{c}_k + t_2 \sum_{\text{n.n.n.}} e^{i\phi_{jk}} \hat{c}_j^\dagger \hat{c}_k, \tag{C1}$$

which is a staggered on-site potential with $\mu_j = 1$ for sites in sublattice A and $\mu_j = -1$ for sites in sublattice B [134]. For $|M| > 3\sqrt{3}t_2|\sin\phi|$, a trivial band gap opens. For

this topologically trivial phase, the finite-size array depicted in figure 3.4.1a has trivial edge modes, whose energies lie within the bulk bands. On the mean-field level, we observe single-mode lasing of a trivial edge mode. We plot the spectrum of elementary excitations (black points) in figure 3.G.1a for the lasing frequency $\Omega/t_1 = 1.03$. For this lasing frequency, long-lived elementary excitations whose decay rates are one order of magnitude smaller than any other energy scale in the system (γ, g, t_1 and t_2) appear due to a large hybridization of trivial edge modes. This is analogous to the long-lived elementary excitations in a topological laser due to the hybridization of topological edge modes discussed in Sec. 3.8.

For moderate on-site disorder, the single-mode lasing is still stable. We compare the spectrum of elementary excitations (gray crosses) for 30 disorder realizations and the spectrum of elementary excitations without disorder (black points) in figure 3.G.1a. The decay rate of elementary excitations with small oscillation frequencies varies strongly in each disorder realization. For some disorder realizations, the hybridization of trivial edge modes is obstructed and the decay rate of the corresponding elementary excitations increases by one order of magnitude. This can be seen in figure 3.G.1b where we plot the complex frequency (gray crosses) with the smallest imaginary part $\min_{\alpha\neq\eta}|\mathrm{Im}\epsilon^{(\alpha)}|$ for each disorder realization. In contrast to the long-lived elementary excitations in a trivial laser, the long-lived elementary excitations in a topological laser are robust against disorder, see appendix 3.F. In the topological laser, the smallest decay rate of elementary excitations only moderately changes depending on each disorder realization and the corresponding oscillation frequency is unchanged, see brown crosses in figure 3.G.1b.

4 Conclusion and outlook

In this thesis, we investigated nonlinear dissipative dynamics of synthetic dynamical gauge fields for photons and topological lasers. The chosen models are relevant to state-of-the-art optomechanical experiments as well as to recent implementations of topological lasers based on semiconductor ring resonators and other photonic structures. We presented our results with a focus on applications.

In chapter 2, we investigated the dynamics of mechanical limit-cycle oscillators assisting the tunneling between optical modes in an optomechanical array. In particular, we showed that synthetic electric fields for photons are dynamically generated in one-dimensional optomechanical arrays, leading to the suppression of light transport. Importantly, the generation of synthetic electric fields depends on the direction of light propagation giving rise to unidirectional light transport. In the second part of chapter 2, we investigated the effects of quantum noise on the dynamics of gauge fields in the minimal setup consisting of two optical modes with photon tunneling assisted by a mechanical self-oscillator. Our results show that the dynamical generation of synthetic electric fields is robust against quantum fluctuations and that unidirectional light transport can be achieved also in the quantum regime. Due to the connection to the mathematical formalism of dynamical gauge fields, the uncovered effects can be observed in any physical system where limit-cycle oscillators assist transitions between linear modes.

In the future, one may investigate how the dynamical generation of synthetic electric fields and light propagation in one- and two-dimensional arrays depend on the distribution of optical frequencies in the arrays. Further, the dependence on driving schemes, which might correspond to either multiple sites or all sites in the arrays being driven, as well as to various patterns of driving amplitudes and phases, could be considered. One might also explore the dynamics of synthetic gauge fields in optomechanical arrays,

which have a topologically nontrivial structure [26]. Further investigation of quantum dynamical gauge fields can include effects of quantum nonlinearities such as the Kerr nonlinearity [54] or strong single-photon optomechanical interaction [63, 64], which lead to a negative Wigner function enabling the study of genuine quantum features of dynamical gauge fields. One might also investigate the interplay of gauge-field dynamics and synchronization, both in the classical regime [77, 144] and in the quantum regime [51, 52, 53, 54, 145].

In chapter 3, we studied the dynamics of lasers – a prominent example of limit-cycle oscillators – coupled in a topological array described by the Haldane model. At the mean-field level, we obtained lasing of a single edge mode. We investigated elementary excitations around the mean-field steady state and their consequences for the coherence properties of the emitted light field. We showed that the hybridization of edge modes gives rise to long-lived elementary excitations leading to large phase fluctuations of the emitted light field and hence decreased coherence. In contrast to long-lived elementary excitations in a trivial laser, their counterparts in a topological laser are robust against disorder. Even though we focused on the Haldane model, long-lived elementary excitations appear for any topological model if the dispersion of edge-mode frequencies is approximately linear around the lasing frequency. In the future, different topological models can be studied to provide insight into how elementary excitations in topological lasers are affected by the presence of several topological band gaps supporting edge modes with opposite chirality [33], a pseudospin degree of freedom in pseudo quantum spin Hall systems [19, 23] or topological lasing in synthetic dimensions [118, 146].

Topological lasers combine topologically-protected chiral light transport and laser amplification. To shed more on the role of chiral transport in lasers, one might consider other approaches for implementing chiral laser arrays. In particular, nonreciprocal light transmission in systems composed of several optical modes can be achieved via reservoir engineering [69, 147]. The nonreciprocal coupling can induce chiral currents in one-dimensional arrays with periodic boundary conditions [148]. In laser arrays, this can lead to lasing of chiral modes, which are similar to chiral edge modes in topological lasers. Due to the translational invariance of a one-dimensional ring, mean-field steady states and elementary excitations can be described analytically. One can particularly investigate how reservoir engineering techniques can be exploited to evade the scattering of light between edge modes with the opposite chirality [43], temporal dynamical

instabilities [126], and static multi-stabilities [127] in laser arrays. These experimental limitations are currently hindering the operation of topological lasers.

Topological lasers are not the only light emitters that can benefit from nontrivial band topology. Combining sources of nonclassical light and a topological photonic structure can lead to a new class of topological quantum emitters, whose spectral properties are protected against disorder [149, 150]. Second- and third-order nonlinearities in topological photonic structures have been studied at the mean-field level, demonstrating that the dynamics of Gaussian quantum fluctuations around a mean field can lead to directional quantum-limited amplification [151] and the generation of squeezing in chiral modes [152]. In the future, one might investigate the dissipative dynamics of photonic structures with parametric nonlinearities beyond the mean-field description to explore the non-Gaussian nature of light manifested in a negative Wigner function, focusing on the topologically protected generation of nonclassical light.

Collective lasing represents a synchronization problem since frequencies and phases of local lasing modes can mutually synchronize due to the coupling of these modes in an array [153]. In the future, one can study the synchronization dynamics in topological lasers and the steady-state phase transitions between lasing at a single frequency and lasing at multiple frequencies, which occurs as the topological invariant of photonic energy bands changes [43]. This will provide an insight into the role of topology, which leads to a novel type of chiral arrays, in the context of synchronization.

Bibliography

[1] P. Zapletal, S. Walter, and F. Marquardt, Phys. Rev. A **100**, 023804 (2019).

[2] P. Zapletal and A. Nunnenkamp, Quantum Sci. Technol. **4**, 044001 (2019).

[3] P. Zapletal, B. Galilo, and A. Nunnenkamp, arXiv:2002.12337 (2020).

[4] S. H. Strogatz, *Nonlinear Dynamics and Chaos* (Perseus books, London, 2001).

[5] A. S. Pikovsky, M. Rosenblum, and J. Kurths, *Synchronization: A Universal Concept in Nonlinear Science* (Cambridge University Press, New York, 2001).

[6] M. Aspelmeyer, T. J. Kippenberg, and F. Marquardt, Rev. Mod. Phys. **86**, 1391 (2014).

[7] J. Chan, T. P. M. Alegre, A. H. Safavi-Naeini, J. T. Hill, A. Krause, S. Gröblacher, M. Aspelmeyer, and O. Painter, Nature **478**, 89 (2011).

[8] J. D. Teufel, T. Donner, D. Li, J. W. Harlow, M. S. Allman, K. Cicak, A. J. Sirois, J. D. Whittaker, K. W. Lehnert, and R. W. Simmonds, Nature **475**, 359 (2011).

[9] D. J. Wilson, V. Sudhir, N. Piro, R. Schilling, A. Ghadimi, and T. J. Kippenberg, Nature **524**, 325 (2015).

[10] E. E. Wollman, C. U. Lei, A. J. Weinstein, J. Suh, A. Kronwald, F. Marquardt, A. A. Clerk, and K. C. Schwab, Science **349**, 952 (2015).

[11] J.-M. Pirkkalainen, E. Damskägg, M. Brandt, F. Massel, and M. A. Sillanpää, Phys. Rev. Lett. **115**, 243601 (2015).

[12] F. Lecocq, J. B. Clark, R. W. Simmonds, J. Aumentado, and J. D. Teufel, Phys. Rev. X **5**, 041037 (2015).

[13] C. F. Ockeloen-Korppi, E. Damskägg, J.-M. Pirkkalainen, M. Asjad, A. A. Clerk, F. Massel, M. J. Woolley, and M. A. Sillanpää, Nature **556**, 478 (2018).

[14] J. L. O'Brien, A. Furusawa, and J. Vučković, Nat. Photonics **3**, 687 (2009).

[15] D. Jaksch and P. Zoller, New J. Phys. **5**, 56 (2003).

[16] Y.-J. Lin, R. L. Compton, K. Jiménez-García, J. V. Porto, and I. B. Spielman, Nature **462**, 628 (2009).

[17] F. D. M. Haldane and S. Raghu, Phys. Rev. Lett. **100**, 013904 (2008).

[18] Z. Wang, Y. Chong, J. D. Joannopoulos, and M. Soljačić, Nature **461**, 772 (2009).

[19] M. Hafezi, E. A. Demler, M. D. Lukin, and J. M. Taylor, Nat. Phys. **7**, 907 (2011).

[20] K. Fang, Z. Yu, and S. Fan, Nat. Photonics **6**, 782 (2012).

[21] M. Hafezi and P. Rabl, Opt. Express **20**, 7672 (2012).

[22] M. C. Rechtsman, J. M. Zeuner, A. Tünnermann, S. Nolte, M. Segev, and A. Szameit, Nat. Photonics **7**, 153 (2013).

[23] M. Hafezi, S. Mittal, J. Fan, A. Migdall, and J. M. Taylor, Nat. Photonics **7**, 1001 (2013).

[24] S. Mittal, J. Fan, S. Faez, A. Migdall, J. M. Taylor, and M. Hafezi, Phys. Rev. Lett. **113**, 087403 (2014).

[25] M. Schmidt, S. Kessler, V. Peano, O. Painter, and F. Marquardt, Optica **2**, 635 (2015).

[26] V. Peano, C. Brendel, M. Schmidt, and F. Marquardt, Phys. Rev. X **5**, 031011 (2015).

[27] L. M. Nash, D. Kleckner, A. Read, V. Vitelli, A. M. Turner, and W. T. M. Irvine, Proc. Natl. Acad. Sci. U.S.A. **112**, 14495 (2015).

[28] R. Süsstrunk and S. D. Huber, Science **349**, 47 (2015).

[29] P. Wang, L. Lu, and K. Bertoldi, Phys. Rev. Lett. **115**, 104302 (2015).

[30] N. Goldman, G. Juzeliūnas, P. Öhberg, and I. B. Spielman, Rep. Prog. Phys. **77**, 126401 (2014).

[31] M. J. Hartmann, J. Opt. **18**, 104005 (2016).

[32] C. W. Gardiner and P. Zoller, *Quantum Noise*, Springer Series in Synergetics (Springer, Berlin/Heidelberg, 2004).

[33] T. Ozawa, H. M. Price, A. Amo, N. Goldman, M. Hafezi, L. Lu, M. C. Rechtsman, D. Schuster, J. Simon, O. Zilberberg, and I. Carusotto, Rev. Mod. Phys. **91**, 015006 (2019).

[34] M. Z. Hasan and C. L. Kane, Rev. Mod. Phys. **82**, 3045 (2010).

[35] X.-L. Qi and S.-C. Zhang, Rev. Mod. Phys. **83**, 1057 (2011).

[36] J. D. Joannopoulos, S. G. Johnson, J. N. Winn, and R. D. Meade, *Photonic Crystals: Molding the Flow of Light* (Princeton University Press, Princeton, 2011).

[37] A. Szameit and S. Nolte, J. Phys. B: At. Mol. Opt. Phys. **43**, 163001 (2010).

[38] D. D. Solnyshkov, O. Bleu, and G. Malpuech, Appl. Phys. Lett. **112**, 031106 (2018).

[39] S. Klembt, T. H. Harder, O. A. Egorov, K. Winkler, R. Ge, M. A. Bandres, M. Emmerling, L. Worschech, T. C. H. Liew, M. Segev, C. Schneider, and S. Höfling, Nature **562**, 552 (2018).

[40] A. Eckardt, Rev. Mod. Phys. **89**, 011004 (2017).

[41] S. D. Huber, Nature **12**, 621 (2016).

[42] C. H. Lee, S. Imhof, C. Berger, F. Bayer, J. Brehm, L. W. Molenkamp, T. Kiessling, and R. Thomale, Communications Physics **1**, 39 (2018).

[43] M. A. Bandres, S. Wittek, G. Harari, M. Parto, J. Ren, M. Segev, D. N. Christodoulides, and M. Khajavikhan, Science **359**, eaar4005 (2018).

[44] G. Harari, M. A. Bandres, Y. Lumer, M. C. Rechtsman, Y. D. Chong, M. Khajavikhan, D. N. Christodoulides, and M. Segev, Science **359**, eaar4003 (2018).

[45] H. Haken, *Light (Volume 2)* (North-Holland Physics Publishing, Amsterdam, 1985).

[46] I. de Vega and D. Alonso, Rev. Mod. Phys. **89**, 015001 (2017).

[47] V. V. Albert and L. Jiang, Phys. Rev. A **89**, 022118 (2014).

[48] M. Scully and M. Zubairy, *Quantum Optics* (Cambridge University Press, 1997).

[49] M. C. Cross and P. C. Hohenberg, Rev. Mod. Phys. **65**, 851 (1993).

[50] A. L. Schawlow and C. H. Townes, Phys. Rev. **112**, 1940 (1958).

[51] T. E. Lee and H. R. Sadeghpour, Phys. Rev. Lett. **111**, 234101 (2013).

[52] S. Walter, A. Nunnenkamp, and C. Bruder, Phys. Rev. Lett. **112**, 094102 (2014).

[53] T. Weiss, A. Kronwald, and F. Marquardt, New J. Phys. **18**, 013043 (2016).

[54] N. Lörch, S. E. Nigg, A. Nunnenkamp, R. P. Tiwari, and C. Bruder, Phys. Rev. Lett. **118**, 243602 (2017).

[55] S. Dutta and N. R. Cooper, Phys. Rev. Lett. **123**, 250401 (2019).

[56] W. Schleich, *Quantum Optics in Phase Space* (Wiley-VCH, Berlin, 2001).

[57] C. Navarrete-Benlloch, T. Weiss, S. Walter, and G. J. de Valcárcel, Phys. Rev. Lett. **119**, 133601 (2017).

[58] A. Noguchi, R. Yamazaki, Y. Tabuchi, and Y. Nakamura, Nat. Commun. **11**, 1183 (2020).

[59] D. Zoepfl, M. L. Juan, C. M. F. Schneider, and G. Kirchmair, Phys. Rev. Lett. **125**, 023601 (2020).

[60] F. Marquardt, J. P. Chen, A. A. Clerk, and S. M. Girvin, Phys. Rev. Lett. **99**, 093902 (2007).

[61] F. Marquardt, J. G. E. Harris, and S. M. Girvin, Phys. Rev. Lett. **96**, 103901 (2006).

[62] M. Ludwig, B. Kubala, and F. Marquardt, New J. Phys. **10**, 095013 (2008).

[63] J. Qian, A. A. Clerk, K. Hammerer, and F. Marquardt, Phys. Rev. Lett. **109**, 253601 (2012).

[64] N. Lörch, J. Qian, A. Clerk, F. Marquardt, and K. Hammerer, Phys. Rev. X **4**, 011015 (2014).

[65] R. W. Andrews, R. W. Peterson, T. P. Purdy, K. Cicak, R. W. Simmonds, C. A. Regal, and K. W. Lehnert, Nat. Phys. **10**, 321 (2014).

[66] H. Xu, D. Mason, L. Jiang, and J. G. E. Harris, Nature **537**, 80 (2016).

[67] S. Hong, R. Riedinger, I. Marinković, A. Wallucks, S. G. Hofer, R. A. Norte, M. Aspelmeyer, and S. Gröblacher, Science **358**, 203 (2017).

[68] R. Riedinger, A. Wallucks, I. Marinković, C. Löschnauer, M. Aspelmeyer, S. Hong, and S. Gröblacher, Nature **556**, 473 (2018).

[69] A. Metelmann and A. A. Clerk, Phys. Rev. X **5**, 021025 (2015).

[70] J. Kim, M. C. Kuzyk, K. Han, H. Wang, and G. Bahl, Nat. Phys. **11**, 275 (2015).

[71] Z. Wang, L. Shi, Y. Liu, X. Xu, and X. Zhang, Sci. Rep. **5**, 8657 (2015).

[72] F. Ruesink, M.-A. Miri, A. Alù, and E. Verhagen, Nat. Commun. **7**, 13662 (2016).

[73] K. Fang, J. Luo, A. Metelmann, M. H. Matheny, F. Marquardt, A. A. Clerk, and O. Painter, Nat. Phys. **13**, 465 (2017).

[74] N. R. Bernier, L. D. Tóth, A. Koottandavida, M. A. Ioannou, D. Malz, A. Nunnenkamp, A. K. Feofanov, and T. J. Kippenberg, Nat. Commun. **8**, 604 (2017).

[75] S. Barzanjeh, M. Wulf, M. Peruzzo, M. Kalaee, P. B. Dieterle, O. Painter, and J. M. Fink, Nat. Commun. **8**, 953 (2017).

[76] D. E. Chang, A. H. Safavi-Naeini, M. Hafezi, and O. Painter, New J. Phys. **13**, 023003 (2011).

[77] G. Heinrich, M. Ludwig, J. Qian, B. Kubala, and F. Marquardt, Phys. Rev. Lett. **107**, 043603 (2011).

[78] A. Xuereb, C. Genes, and A. Dantan, Phys. Rev. Lett. **109**, 223601 (2012).

[79] M. Ludwig and F. Marquardt, Phys. Rev. Lett. **111**, 073603 (2013).

[80] M. Aidelsburger, M. Atala, S. Nascimbène, S. Trotzky, Y.-A. Chen, and I. Bloch, Phys. Rev. Lett. **107**, 255301 (2011).

[81] M. Aidelsburger, M. Atala, M. Lohse, J. T. Barreiro, B. Paredes, and I. Bloch, Phys. Rev. Lett. **111**, 185301 (2013).

[82] C. Brendel, V. Peano, O. J. Painter, and F. Marquardt, Proc. Natl. Acad. Sci. U.S.A. **114**, E3390 (2017).

[83] C. Brendel, V. Peano, O. Painter, and F. Marquardt, Phys. Rev. B **97**, 020102(R) (2018).

[84] A. Seif, W. DeGottardi, K. Esfarjani, and M. Hafezi, Nat. Commun. **9**, 1207 (2018).

[85] S. Walter and F. Marquardt, New J. Phys. **18**, 113029 (2016).

[86] C. N. Yang and R. L. Mills, Phys. Rev. **96**, 191 (1954).

[87] P. W. Anderson, Phys. Rev. **130**, 439 (1963).

[88] P. W. Higgs, Phys. Rev. Lett. **13**, 508 (1964).

[89] H. Kleinert, *Gauge Fields in Condensed Matter* (World Scientific, Singapore, 1989).

[90] C. Castelnovo, R. Moessner, and S. L. Sondhi, Annu. Rev. Condens. Matter Phys. **3**, 35 (2012).

[91] P. E. Lammert, D. S. Rokhsar, and J. Toner, Phys. Rev. Lett. **70**, 1650 (1993).

[92] P. E. Lammert, D. S. Rokhsar, and J. Toner, Phys. Rev. E **52**, 1778 (1995).

[93] D. Banerjee, M. Dalmonte, M. Müller, E. Rico, P. Stebler, U.-J. Wiese, and P. Zoller, Phys. Rev. Lett. **109**, 175302 (2012).

[94] E. Zohar, J. I. Cirac, and B. Reznik, Rep. Prog. Phys. **79**, 014401 (2016).

[95] D. Marcos, P. Rabl, E. Rico, and P. Zoller, Phys. Rev. Lett. **111**, 110504 (2013).

[96] D. Marcos, P. Widmer, E. Rico, M. Hafezi, P. Rabl, U. J. Wiese, and P. Zoller, Annals of Physics **351**, 634 (2014).

[97] K. E. Ballantine, B. L. Lev, and J. Keeling, Phys. Rev. Lett. **118**, 045302 (2017).

[98] P. Hauke, D. Marcos, M. Dalmonte, and P. Zoller, Phys. Rev. X **3**, 041018 (2013).

[99] E. A. Martinez, C. A. Muschik, P. Schindler, D. Nigg, A. Erhard, M. Heyl, P. Hauke, M. Dalmonte, T. Monz, P. Zoller, and R. Blatt, Nature **534**, 516 (2016).

[100] L. Yuan and S. Fan, Phys. Rev. Lett. **114**, 243901 (2015).

[101] L. Yuan and S. Fan, Optica **3**, 1014 (2016).

[102] P. Rabl, Phys. Rev. Lett. **107**, 063601 (2011).

[103] A. Nunnenkamp, K. Børkje, and S. M. Girvin, Phys. Rev. Lett. **107**, 063602 (2011).

[104] K. J. Vahala, Phys. Rev. A **78**, 023832 (2008).

[105] D. A. Rodrigues and A. D. Armour, Phys. Rev. Lett. **104**, 053601 (2010).

[106] A. D. Armour and D. A. Rodrigues, C. R. Phys. **13**, 440 (2012).

[107] P. D. Drummond and D. F. Walls, J. Phys. A: Math. Gen. **13**, 725 (1980).

[108] J. D. Thompson, B. M. Zwickl, A. M. Jayich, F. Marquardt, S. M. Girvin, and J. G. E. Harris, Nature **452**, 72 (2008).

[109] J. C. Sankey, C. Yang, B. M. Zwickl, A. M. Jayich, and J. G. E. Harris, Nat. Phys. **6**, 707 (2010).

[110] A. H. Safavi-Naeini and O. Painter, New J. Phys. **13**, 013017 (2011).

[111] T. K. Paraïso, M. Kalaee, L. Zang, H. Pfeifer, F. Marquardt, and O. Painter, Phys. Rev. X **5**, 041024 (2015).

[112] H. Wu, G. Heinrich, and F. Marquardt, New J. Phys. **15**, 123022 (2013).

[113] M. R. Hush, W. Li, S. Genway, I. Lesanovsky, and A. D. Armour, Phys. Rev. A **91**, 061401(R) (2015).

[114] V. M. Martinez Alvarez, J. E. Barrios Vargas, M. Berdakin, and L. E. F. Foa Torres, Eur. Phys. J. Spec. Top. **227**, 1295 (2018).

[115] H. Zhao, X. Qiao, T. Wu, B. Midya, S. Longhi, and L. Feng, Science **365**, 1163 (2019).

[116] A. Cerjan, S. Huang, M. Wang, K. P. Chen, Y. Chong, and M. C. Rechtsman, Nat. Photonics **13**, 623 (2019).

[117] T. Ozawa, H. M. Price, N. Goldman, O. Zilberberg, and I. Carusotto, Phys. Rev. A **93**, 043827 (2016).

[118] E. Lustig, S. Weimann, Y. Plotnik, Y. Lumer, M. A. Bandres, A. Szameit, and M. Segev, Nature **567**, 356 (2019).

[119] A. Dutt, Q. Lin, L. Yuan, M. Minkov, M. Xiao, and S. Fan, Science **367**, 59 (2020).

[120] D. Smirnova, D. Leykam, Y. Chong, and Y. Kivshar, Appl. Phys. Rev. **7**, 021306 (2020).

[121] P. St-Jean, V. Goblot, E. Galopin, A. Lemaître, T. Ozawa, L. L. Gratiet, I. Sagnes, J. Bloch, and A. Amo, Nat. Photonics **11**, 651 (2017).

[122] M. Parto, S. Wittek, H. Hodaei, G. Harari, M. A. Bandres, J. Ren, M. C. Rechtsman, M. Segev, D. N. Christodoulides, and M. Khajavikhan, Phys. Rev. Lett. **120**, 113901 (2018).

[123] H. Zhao, P. Miao, M. H. Teimourpour, S. Malzard, R. El-Ganainy, H. Schomerus, and L. Feng, Nat. Commun. **9**, 981 (2018).

[124] B. Bahari, A. Ndao, F. Vallini, A. E. Amili, Y. Fainman, and B. Kanté, Science **358**, 636 (2017).

[125] Y. Zeng, U. Chattopadhyay, B. Zhu, B. Qiang, J. Li, Y. Jin, L. Li, A. G. Davies, E. H. Linfield, B. Zhang, Y. Chong, and Q. J. Wang, Nature **578**, 246 (2020).

[126] S. Longhi, Y. Kominis, and V. Kovanis, EPL **122**, 14004 (2018).

[127] M. Seclì, M. Capone, and I. Carusotto, Phys. Rev. Research **1**, 033148 (2019).

[128] A. Pick, A. Cerjan, D. Liu, A. W. Rodriguez, A. D. Stone, Y. D. Chong, and S. G. Johnson, Phys. Rev. A **91**, 063806 (2015).

[129] P. Delplace, J. B. Marston, and A. Venaille, Science **358**, 1075 (2017).

[130] X.-L. Qi, Y.-S. Wu, and S.-C. Zhang, Phys. Rev. B **74**, 045125 (2006).

[131] K. v. Klitzing, G. Dorda, and M. Pepper, Phys. Rev. Lett. **45**, 494 (1980).

[132] D. J. Thouless, M. Kohmoto, M. P. Nightingale, and M. den Nijs, Phys. Rev. Lett. **49**, 405 (1982).

[133] B. I. Halperin, Phys. Rev. B **25**, 2185 (1982).

[134] F. D. M. Haldane, Phys. Rev. Lett. **61**, 2015 (1988).

[135] C. L. Kane and E. J. Mele, Phys. Rev. Lett. **95**, 226801 (2005).

[136] C. L. Kane and E. J. Mele, Phys. Rev. Lett. **95**, 146802 (2005).

[137] S. Raghu and F. D. M. Haldane, Phys. Rev. A **78**, 033834 (2008).

[138] M. C. Rechtsman, J. M. Zeuner, Y. Plotnik, Y. Lumer, D. Podolsky, F. Dreisow, S. Nolte, M. Segev, and A. Szameit, Nature **496**, 196 (2013).

[139] G. Jotzu, M. Messer, R. Desbuquois, M. Lebrat, T. Uehlinger, D. Greif, and T. Esslinger, Nature **515**, 237 (2014).

[140] P. G. Savvidis, C. Ciuti, J. J. Baumberg, D. M. Whittaker, M. S. Skolnick, and J. S. Roberts, Phys. Rev. B **64**, 075311 (2001).

[141] N. R. Bernier, E. G. Dalla Torre, and E. Demler, Phys. Rev. Lett. **113**, 065303 (2014).

[142] N. R. Bernier, L. D. Tóth, A. K. Feofanov, and T. J. Kippenberg, Phys. Rev. A **98**, 023841 (2018).

[143] H. Hodaei, M.-A. Miri, M. Heinrich, D. N. Christodoulides, and M. Khajavikhan, Science **346**, 975 (2014).

[144] R. Lauter, C. Brendel, S. J. M. Habraken, and F. Marquardt, Phys. Rev. E **92**, 012902 (2015).

[145] T. Weiss, S. Walter, and F. Marquardt, Phys. Rev. A **95**, 041802(R) (2017).

[146] Z. Yang, E. Lustig, G. Harari, Y. Plotnik, Y. Lumer, M. A. Bandres, and M. Segev, Phys. Rev. X **10**, 011059 (2020).

[147] J. F. Poyatos, J. I. Cirac, and P. Zoller, Phys. Rev. Lett. **77**, 4728 (1996).

[148] M. Keck, D. Rossini, and R. Fazio, Phys. Rev. A **98**, 053812 (2018).

[149] S. Mittal, E. A. Goldschmidt, and M. Hafezi, Nature **561**, 502 (2018).

[150] V. V. Orre, S. Mittal, E. A. Goldschmidt, and M. Hafezi, arXiv: 2006.03084 (2020).

[151] V. Peano, M. Houde, F. Marquardt, and A. A. Clerk, Phys. Rev. X **6**, 041026 (2016).

[152] T. Shi, H. J. Kimble, and J. I. Cirac, PNAS **114**, E8967 (2017).

[153] M. Nixon, M. Fridman, E. Ronen, A. A. Friesem, N. Davidson, and I. Kanter, Phys. Rev. Lett. **108**, 214101 (2012).